The Philosophical Magazine

FIRST PUBLISHED IN 1798

A Journal of Theoretical Experimental and Applied Physics

UNIVERSITY OF HAWAII LIBRARY
SEP 25 '59

Vol. 4 June 1959 No. 42
Eighth Series

£1 5s. 0d., plus postage
Annual Subscription £13 10s. 0d., payable in advance

ALERE FLAMMAM

Printed and Published by
TAYLOR & FRANCIS LTD
RED LION COURT, FLEET STREET, LONDON, E.C.4

THE PHILOSOPHICAL MAGAZINE

Editor

Professor N. F. Mott, M.A., D.Sc., F.R.S.

Editorial Board

Sir Lawrence Bragg, O.B.E., M.C., M.A., D.Sc., F.R.S.
Sir George Thomson, M.A., D.Sc., F.R.S.
Professor A. M. Tyndall, C.B.E., D.Sc., F.R.S.

Authors wishing to submit papers for publication in the Journal should send manuscripts directly to the Publishers.

Manuscripts should be typed in *double* spacing on one side of quarto (8 × 10 in.) paper, and authors are urged to aim at absolute clarity of meaning and an attractive presentation of their texts.

References should be listed at the end in alphabetical order of authors and should be cited in the text in terms of author's name and date. Diagrams should normally be in Indian ink on white card, with lettering in soft pencil, the captions being typed on a separate sheet.

A leaflet giving detailed instructions to authors on the preparation of papers is available on request from the Publishers.

Authors are entitled to receive 25 offprints of a paper in the Journal free of charge, and additional offprints can be obtained from the Publishers.

The *Philosophical Magazine* and its companion journal, *Advances in Physics*, will accept papers for publication in experimental and theoretical physics. The *Philosophical Magazine* publishes contributions describing new results, letters to the editor and book reviews. *Advances in Physics* publishes articles surveying the present state of knowledge in any branch of the science in which recent progress has been made. The editors welcome contributions from overseas as well as from the United Kingdom, and papers may be published in English, French and German.

The Growth of Grain-boundary Voids Under Stress†

By D. HULL and D. E. RIMMER

Atomic Energy Research Establishment, Harwell

[Received January 1, 1959]

ABSTRACT

The effect of combined hydrostatic pressure, P, and of uniaxial tension, σ, on the rupture time of polycrystalline copper wire in the temperature range 400° to 500°C has been determined. All the specimens broke by intergranular fracture, due to the growth of voids along grain boundaries. Preliminary experiments indicated that the voids grow by the addition of vacancies under the action of the applied stress. A theory has been developed assuming that failure results from the growth of void nuclei on the grain boundary, which requires that the activation energy for failure is that of grain boundary diffusion and that the rupture time, t_r, depends only on $(\sigma-P)$. The experiments show that the activation energy is close to the expected value, and provided that σ is constant t_r agrees with theory. Changes in σ, when $(\sigma-P)$ is constant, affect t_r appreciably, and the results suggest that many of the void nuclei are stress induced.

§ 1. INTRODUCTION

IN recent years attention has been drawn to the mechanism of failure of metals under certain creep conditions. Small voids have been observed at grain boundaries, particularly those transverse to the applied stress when specimens are tested at high temperatures; rupture results from the growth and coalescence of these voids (Greenwood *et al.* 1954). This type of failure has been observed in Magnox cans used for containing uranium fuel elements, and the present work was undertaken to try to understand the mechanism of void nucleation and growth.

There appear to be several methods whereby voids might be nucleated on grain boundaries. Grain boundary sliding can open up a hole at the junction of three boundaries or a ledge on a single boundary. Impurity particles which lack cohesion with the lattice may act as pre-existing voids. A dislocation pile-up breaking through to the boundary might also be a suitable nucleus. Of these four possibilities, all except the first must have vacancies supplied to them if they are to grow. Balluffi and Seigle (1957) have shown that sufficient vacancies can be produced at transverse grain boundaries because of the tension acting across the boundary, and suggest that this method of void growth is more likely to occur than that based on condensation of vacancies produced during strain (Machlin 1956). If the latter mechanism is operative voids would be produced by both tensile and compressive strains. However, no vacancies can be generated at a grain boundary by applying a compressive stress across it. It was decided, therefore, to carry out a series of short time creep tests in which a uniaxial tensile stress and a hydrostatic pressure were applied simultaneously.

---

† Communicated by the Authors.

In the first part of this paper we outline a mechanism of rupture based on the growth of void nuclei on a grain boundary by the addition of vacancies from the boundary. The effect of hydrostatic pressure and uniaxial tensile stress on the time for failure of such a system is calculated. The results of experiments designed to test this model are given and these are discussed.

§ 2. THEORY OF RUPTURE BY VOID GROWTH

The initial experimental results suggested that the mechanism proposed by Balluffi and Seigle (1957) was probably the operative one for vacancy formation. This process must certainly be occurring, regardless of any other mode of void growth which may also operate, and it permits an analysis in terms of parameters which may be estimated with reasonable precision.

In this section we shall derive an approximate expression for the rupture time, in order to show the significant features of this model. A fairly rigorous solution for a system having a simple geometry is given in the Appendix.

2.1. *Estimate of Rupture Time*

The specimen is taken to be in the form of a wire and subjected to a uniaxial stress, σ, along its length and a hydrostatic pressure P. Void nuclei of an unspecified nature are assumed to lie on the grain boundaries. ρ_0 will denote the radius of a typical nucleus and a their mean separation.

At the temperature at which the tests are being made (400° to 500°C) grain-boundary diffusion is more efficient than lattice diffusion in transporting the surface atoms of the void to the grain boundary. This may be shown briefly by the following calculation:

The ratio of the number of atoms transferred from the void to the boundary by lattice diffusion to that by grain-boundary diffusion is given approximately by

$$\frac{D_l \cdot \rho}{D_g \, . \, \delta z}$$

where D_l and D_g are respectively lattice and grain-boundary diffusion coefficients, ρ is the void radius and δz the grain-boundary width.

$D_g \, . \, \delta z \sim 3 \times 10^{-15}$ cm^3 sec^{-1} for silver at 500°C (Hoffman and Turnbull 1951), and a similar value is to be expected for copper. At the same temperature D_l (for copper) $\sim 2 \times 10^{-14}$ cm^2 sec^{-1}. Even if $\rho = 10^{-2}$ cm, which must be an extreme upper limit to its possible size, the contribution from lattice diffusion is only 6% of the total, so that we are justified in neglecting it. If there is considerable enhancement of lattice diffusion under stress, this argument may no longer be valid; the results, however, seem to indicate that lattice diffusion does not occur.

In view of this it is presumed that the atoms are released from within a ring round each void, which lies in, and has the same thickness, δz, as the grain boundary.

The rate of growth of a void is determined by the gradient of chemical potential, ∇f, in the plane of the grain boundary, since the diffusion flux, j, is given by (Herring 1950)

$$j = \frac{D_g}{kT\Omega} \nabla f$$

where k = Boltzmann's constant, T = absolute temperature, Ω = atomic volume, and ∇f is to be evaluated at the void surface.

In the grain boundary, the potential is given by (Herring 1950)

$$f = -\sigma_n \Omega$$

where σ_n is the normal tension acting across the boundary. At a point well away from any void it may be assumed that this is roughly equal to the resultant of the externally applied stresses and has a maximum value $(\sigma - P)$ on a grain boundary normal to the direction of σ.

On the surface of a void $f = -2\gamma\Omega/\rho$, where γ is the surface tension of the metal.

Hence, as a rough approximation we may take,

$$\nabla f \sim -\frac{\Omega}{a}\left(\sigma - P - \frac{2\gamma}{\rho}\right)$$

giving

$$j \sim \frac{D_g}{kTa}\left(\sigma - P - \frac{2\gamma}{\rho}\right).$$

This shows that only those nuclei for which

$$\rho_0 > \frac{2\gamma}{\sigma - P}$$

will grow. For voids smaller than this critical size the applied stress is not sufficient to overcome the surface tension and sintering occurs. Assuming that there are some nuclei which can grow, the larger ones will determine the rupture time and it then is reasonable to neglect $2\gamma/\rho$ with respect to $(\sigma - P)$.

The area of the void surface from which diffusion takes place is $2\pi\rho\delta z$, so that the rate of increase in void volume is given by

$$\frac{dV}{dt} \sim \frac{(D_g \delta z)(\sigma - P) \cdot 2\pi\rho\Omega}{kTa}.$$

If the bubble retains spherical shape by surface diffusion, we have

$$\frac{d\rho}{dt} \sim \frac{(D_g \delta z)(\sigma - P)\Omega}{2kTa\rho}.$$

To obtain the rupture time, t_r, this expression must be integrated between $\rho=\rho_0$ and $\rho\sim\frac{1}{2}a$.

Assuming that $a\gg\rho_0$ this gives

$$t_r\sim\frac{kTa^3}{4(D_g\delta z)(\sigma-P)\Omega}.$$

It is shown in the Appendix that for an array of equally sized nuclei lying on a square lattice the rupture time is given almost exactly by

$$t_r=\frac{kTa}{2\pi\Omega(D_g\delta z)(\sigma-P)}\left\{\frac{a^2}{8}+\frac{\gamma a}{(\sigma-P)}+\frac{4\gamma^2}{(\sigma-P)^2}\ln\left[\frac{\frac{1}{2}a(\sigma-P)-2\gamma}{\rho_0(\sigma-P)-2\gamma}\right]\right\}. \quad . \; . \; . \quad (11)$$

The approximate result differs by a factor of 4π from the first term in the bracket in eqn. (11). The effect of nucleus size, which was neglected above, appears in the third term and is usually negligible except for values of ρ_0 only slightly greater than $2\gamma/(\sigma-P)$.

It would appear that the square array is about the best simple periodic approximation that can be made to a random arrangement of nuclei, but in order to estimate the effect of the assumed spatial distribution on the result it was decided to carry out an analysis similar to that given in the Appendix, but for a single void feeding atoms into a concentric ring of grain-boundary having the same initial area, i.e. $(a^2-\pi\rho_0{}^2)$. A close-packed array of such systems is an alternative approximation that may be made to a real grain boundary. Using a particular set of parameters the time for failure on this model was about 70% of the breaking time using the square lattice. The longer time taken by the square lattice is due to the fact that the region of grain boundary associated with each void is of a more irregular shape than that of the other model (in which circular symmetry is used), and is therefore the more realistic.

It therefore seems reasonable to use eqn. (11) for the interpretation of experimental results, with the following proviso. A randomly dispersed array of mean separation a should bring about fracture in a shorter time than the uniform set considered in obtaining eqn. (11), as some will join up quickly and increase the local stress concentration. A value of a determined from an experimental result will therefore be somewhat less than the mean distance between nuclei.

2.2. *Theoretical Predictions*

The significant features of eqn. (11) are: (i) The activation energy of the process is that for grain-boundary diffusion. (ii) The quantities σ and P only occur in the form $(\sigma-P)$ so that for identical specimens at the same temperature the breaking-time is a function only of $(\sigma-P)$. If $(\sigma-P)\gg2\gamma/\rho_0$ the three terms on the right-hand side of eqn. (11) are in the approximate ratio

$$\frac{1}{8}\;:\;\frac{\gamma}{a(\sigma-P)}\;:\;4\left(\frac{\gamma}{a(\sigma-P)}\right)^2.$$

Taking $\gamma=10^3$ dyne cm^{-1}, $a\sim2\times10^{-4}$ cm, the first term dominates if $(\sigma-P) \gtrsim 5\times 10^7$ dyne cm^{-2} = 750 p.s.i. In the experiments to be described this is true, although significant contributions come from the other two terms. Thus the shape of the t_r versus $(\sigma-P)$ curve is approximately hyperbolic down to $(\sigma-P)=2\gamma/\rho_0$, at which point the third term becomes infinite. Physically this is the point at which the applied stress is balanced by the surface tension of the void nucleus, so that the voids never grow. Figure 1 shows the expected variation of t_r with $(\sigma-P)$.

Fig. 1

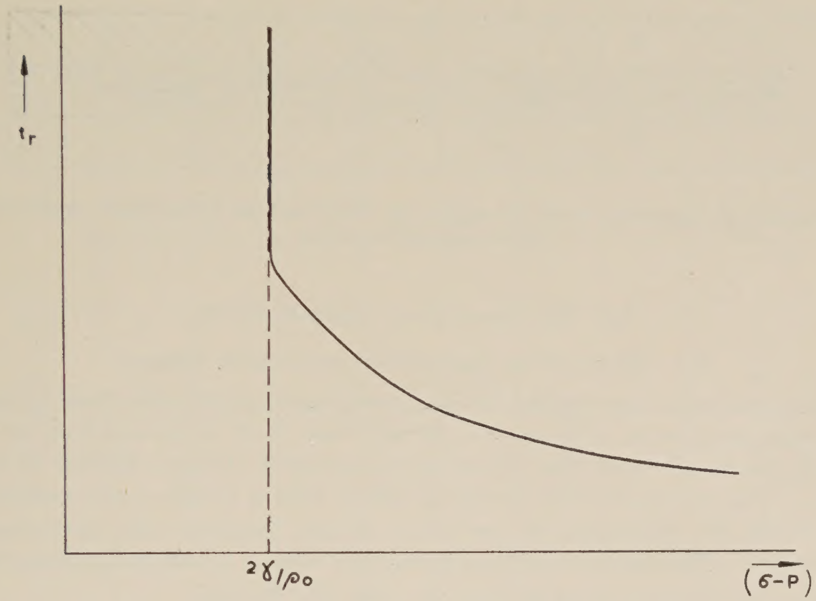

Theoretical Variation of t_r with $(\sigma-P)$.

§ 3. Experimental Details

The tests were made on a relatively impure copper (99·8%) which contained small copper oxide inclusions in short stringers along the direction of drawing. The specimens were in the form of wire 0·020 in. diameter, which was etched in dilute nitric acid to reduce the diameter to between 0·013 and 0·010 in. along a 1 in. gauge length. Copper beads were welded onto the ends of the wire specimens to hold them in the apparatus. The specimens were annealed at 600°c for one hour before testing. Combined hydrostatic and uniaxial tensile stresses were applied using the apparatus illustrated in fig. 2. The tensile stresses were obtained using a spring D attached to one end of the specimen C and held in a silica tube B, approximately 12 in. long. This assembly was inserted inside a pressure bomb A (Fennell *et al.* 1958) with an internal diameter 5/16 in., capable of holding pressures of 6000 p.s.i. for a few hours. All the tests were made in argon. The time to fracture was measured by means of an electric clock circuit through the specimen. The pressure bomb was inserted in a furnace tube and temperatures between 400° and 500°c maintained to ±3°c. The creep strain was not measured during the test, but measurements on fractured specimens showed that the creep strain was less than 3 to 5%.

The specimens were examined metallographically after fracture by sectioning along their length followed by polishing on fine alumina.

Fig. 2

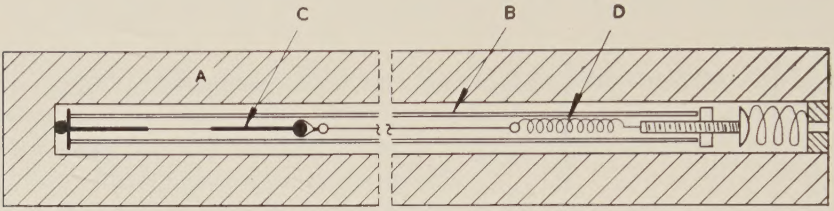

Diagram of apparatus used for applying simultaneous hydrostatic pressure and uniaxial tension.

§ 4. Experimental Observations

4.1. *Effect of Non-hydrostatic Compressive Stresses*

An experiment was carried out to determine whether voids were formed in specimens tested with $\sigma = P$. In this case there is no resolved stress along the tensile axis, but there are compressive stresses normal to this axis. The specimens were tested at 480°c with a tensile stress sufficient to break the specimens in less than 20 min (without the hydrostatic pressure). The specimens did not fracture after 8 hours and subsequent micro-examination revealed that no voids had formed.

4.2. *Metallography*

It was confirmed that all the specimens tested had ruptured by the formation of voids on grain boundaries. Figure 3 (Pl. 77) shows the general appearance of a specimen, the majority of voids having formed on boundaries normal to the applied stress. A few stringers of oxide particles are also visible. Figure 4 (Pl. 77) is a high magnification photograph which shows clearly the voids along grain boundaries. Voids do not form on twin boundaries, even when the boundaries are transverse to the applied stress. The photographs show that the voids in fractured specimens are close together and often coalesce. The size and number of voids varied with the applied stress. This is illustrated in the photographs (figs. 5 and 6 (Pl. 78)) of two specimens tested at the same temperature, the first stressed at 4730 p.s.i. and the second at 3000 p.s.i. At the high stress a large number of small voids have formed compared with a smaller number of larger voids at the low stress.

4.3. *Activation Energy of the Process Leading to Rupture*

A series of specimens was tested at a constant uniaxial tension and the time to fracture measured for a range of testing temperatures between 370° and 490°c. The results, which are plotted in fig. 7, give an activation energy of 25 000 ± 3000 cals/mole. This figure compares well with the activation energy for grain-boundary diffusion determined for silver (20 200 cals/mole) (Hoffman and Turnbull 1951).

Fig. 7

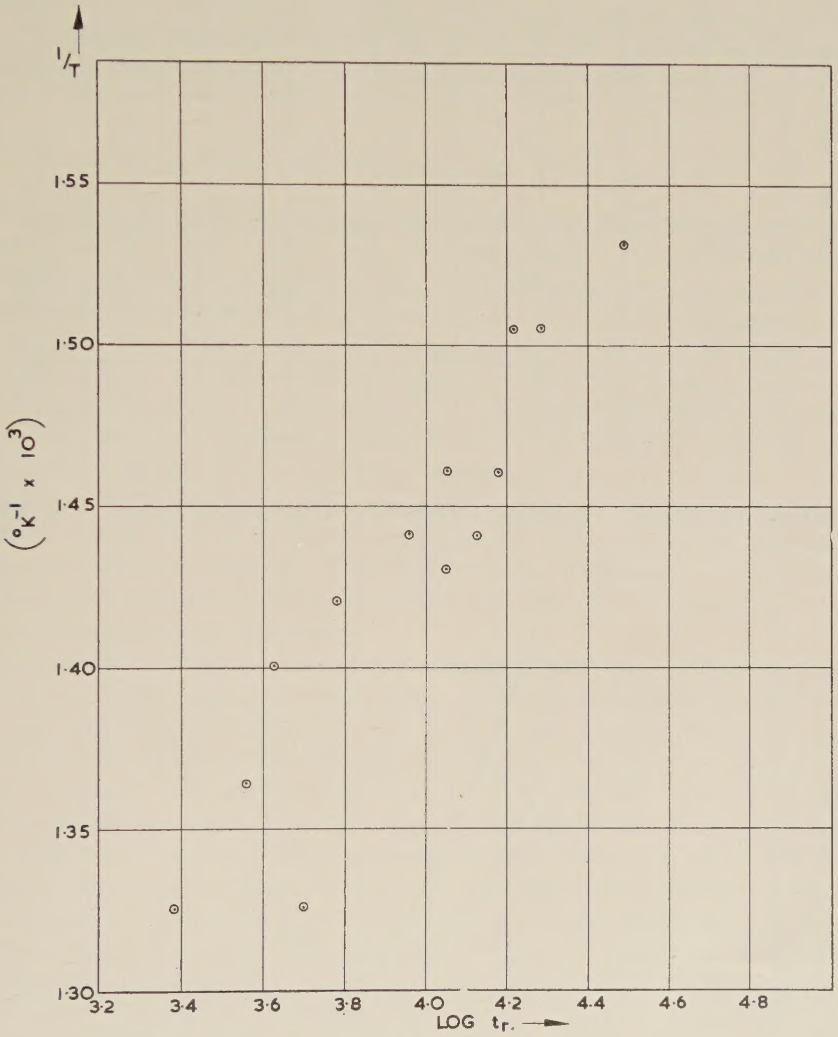

Variation of log t_r with $1/T$ for $\sigma = 4730$ p.s.i., $P = 0$.

Fig. 8

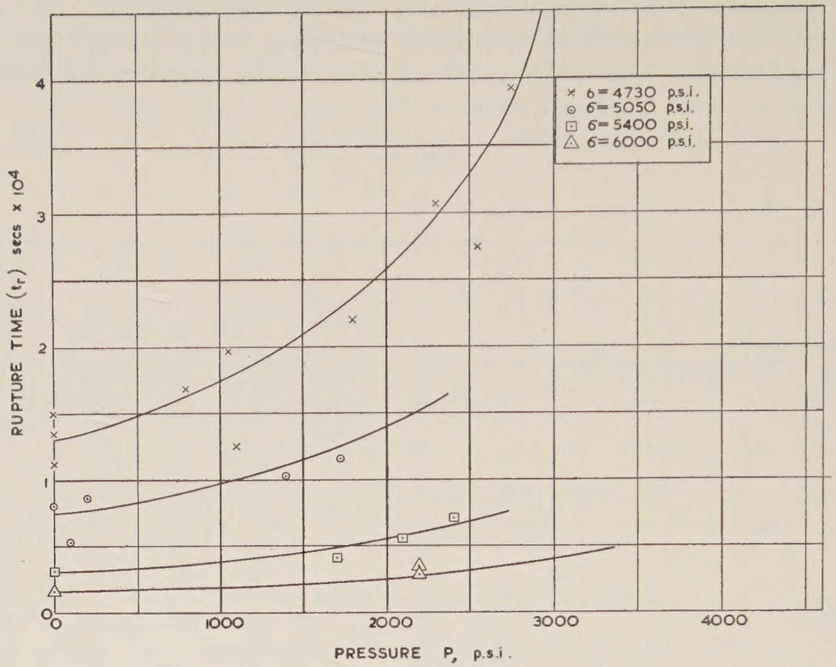

Variation of t_r with P. Experimental points with theoretical curves. $T = 410°$C.

Fig. 9

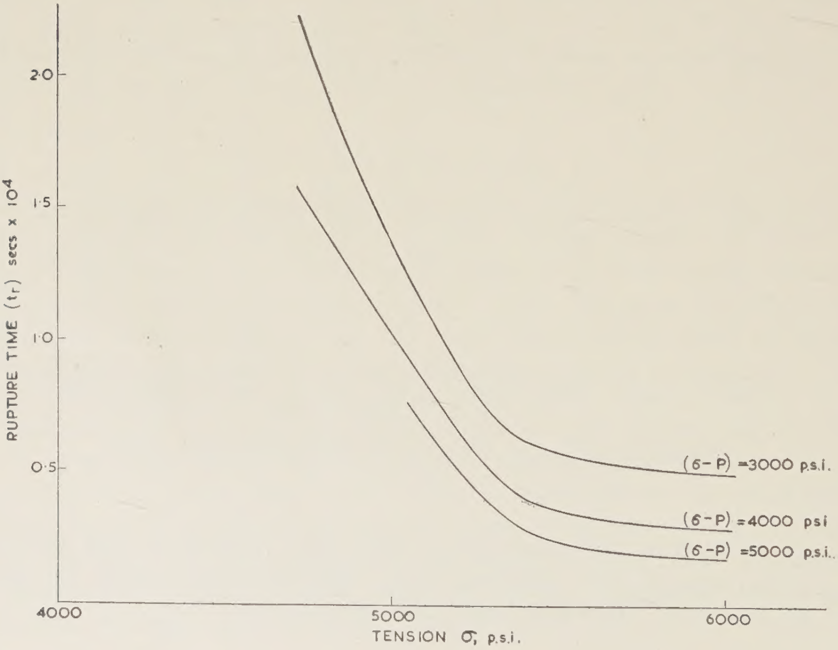

Variation of t_r with σ for constant values of $(\sigma - P)$.
(Taken from smoothed experimental results at 410°C.)

4.4. *Effect of Stress* (σ) *and Pressure* (P) *at Constant Temperature*

The variation of the time to rupture (t_r) with hydrostatic pressure for a number of values of σ was obtained at 410°C and the results are plotted in fig. 8. The variation of rupture time with stress for a number of values of $(\sigma-P)$ has been obtained from these results and is plotted in fig. 9. Equation (11) predicts that the rupture time should be dependent only on $(\sigma-P)$, i.e. a variation of σ should not affect the rupture time providing $(\sigma-P)$ remains constant. As shown in fig. 9, the rupture time alters appreciably with change in σ and this is discussed below in § 5.

§ 5. DISCUSSION

In § 4.1 an experiment designed to test the theory of void growth by vacancy condensation under strain was described. It was shown that although a certain stress applied in tension would easily break the specimen, when applied in compression it could not do so. Further, in the latter case no visible voids were produced. This suggests that the vacancies for void growth are produced by the tension across the grain boundaries rather than deformation inside the grain. It seemed reasonable therefore to try and correlate the experimental results with a theory based on the grain-boundary diffusion model from which eqn. (11) was derived.

The activation energy of the processes leading to rupture in the temperature range used corresponds with that for grain-boundary diffusion rather than lattice diffusion. This supports one of the basic assumptions of the theory that the voids grow by the diffusion of atoms from the void surface along the grain boundary.

Examination of the results in fig. 8 compared with eqn. (11) shows that the theory cannot explain all the experimental results, since if $(\sigma-P)$ were the only stress factor affecting t_r then for a constant value of $(\sigma-P)$, e.g. 3000 p.s.i., the breaking time should be constant, whereas at $\sigma=4730$ p.s.i. $t_r=2{\cdot}2\times10^4$ sec, and at $\sigma=5050$ p.s.i., $t_r=1{\cdot}25\times10^4$ sec. However, we shall consider first how eqn. (11) agrees with the effect of $(\sigma-P)$ on t_r providing σ is constant, and then examine the variation of t_r with σ. Figure 8 shows some observed values of t_r as a function of P for a number of values of σ. Equation (11), with which it is to be compared, contains two unknowns, a and ρ_0. The appropriate value to use for ρ_0 is difficult to determine. It is however possible to find a lower limit for it because it is known that $t_r\to\infty$ as $(\sigma-P)\to2\gamma/\rho_0$ (see § 2.2). Figure 8 shows that t_r is still finite when $(\sigma-P)=2000$ p.s.i. It is unlikely that this, the smallest experimental value, is by coincidence very close to the critical one. If we take 1500 p.s.i. $=10^8$ dyne cm^{-2} as the critical value

$$\rho_0=\frac{2\times10^3}{10^8}=2\times10^{-5}\text{ cm}$$

which is reasonable. Using this figure, any one of the experimental results giving t_r for specified values of σ and P will enable a value for a to be calculated by eqn. (11). This may then be used to predict values of t_r for comparison with the remaining experimental values. If results for which $P=0$ are used to determine a, the term containing ρ_0 is small and the assumptions made in its estimation have little effect on the calculated value of a.

It was found that for each value of σ, a different value of a is needed to fit the experimental point at $P=0$. However, if for any given σ, the appropriate value of a is used to derive the $t_r(P)$ relation, this agrees well with the experimental points. The full lines in fig. 8 are the theoretical curves, using the following values of a:

Table Giving the Distance Between Voids, a, for Values of Applied Tension, σ

σ (p.s.i.)	a (μ)
4730	2·1
5050	1·8
5400	1·3
6000	1·1

As explained in § 2.1 the values obtained for a are likely to be rather less than the mean distance between nuclei. This suggests a void separation of about 3 μ, a figure which is in general agreement with the metallographic observations (see figs. 3 and 4).

The effect of variation of σ on t_r for constant values of $(\sigma-P)$ is shown in fig. 9. At higher values of σ the rupture time is less. This is in agreement with the results given in the table, where it is shown that the distance between voids a, decreases with increasing σ and therefore if the growing force $(\sigma-P)$ is constant the rupture time will decrease with increasing σ. The observation (§ 4.2) that there are more voids present after a tensile stress of 4730 p.s.i. has been applied than after 3000 p.s.i. supports this conclusion.

Thus it would appear that the mechanism of void growth is as postulated in the theory, but that in order to explain all the experimental facts it is necessary to allow a density of void nuclei which increases with applied tension. This virtually implies that the stress itself is generating nuclei. These could result from grain boundary sliding as suggested by Gifkins (1956) and Chen and Machlin (1956). It is also possible that some of the impurity particles are more firmly bound to the lattice than others, and only become free when the specimen is strained.

It does not seem possible to make any useful deductions about the number of nuclei produced by stress. Estimates made from the a values given in the table would require the assumption that all nuclei are produced at the beginning of the experiment. This also prevents a useful comparison with the observed variation of void separation with stress.

In conclusion, the experiments show that the grain-boundary voids which are frequently observed to be the cause of creep failure, grow by the diffusion of surface atoms to the surrounding grain boundary under the action of the applied stress. It appears that many of the void nuclei are induced by the stress, but their exact nature is uncertain.

ACKNOWLEDGMENTS

It is a pleasure to thank Professor A. H. Cottrell, Dr. W. M. Lomer and Mr. R. S. Barnes for many useful discussions, and Messrs. D. C. Wynne and B. Hudson for help with some of the experimental work.

REFERENCES

BALLUFFI, R. W., and SEIGLE, L. L., 1957, *Acta Met.*, **5,** 449.
CHEN, C. W., and MACHLIN, E. S., 1956, *Acta Met.*, **4,** 655.
FENNELL, J., HANCOCK, N. H., and BARNES, R. S., 1958, *Metal Treatm.*, **25,** 332.
GIFKINS, R. D., 1956, *Acta Met.*, **4,** 98.
GREENWOOD, J. N., MILLER, D. R., and SUITER, J. W., 1954, *Acta Met.*, **2,** 250.
HERRING, C., 1950, *J. appl. Phys.*, **21,** 437.
HOFFMAN, R. E., and TURNBULL, D., 1951, *J. appl. Phys.*, **22,** 634.
MACHLIN, E. S., 1956, *Trans. Amer. Inst. min. (metall.) Engrs*, **206,** 106.

APPENDIX

The Rupture Time for a Square Array of Equally Sized Nuclei

Figure 10 shows a square array of spherical voids with repeat distance a and having grown to a radius ρ, lying on a grain-boundary normal to the direction of σ. The centre of a void is taken as the origin of rectangular and polar axes.

In order to calculate ∇f at the void surface it is necessary to define the problem more exactly than in § 2, and we shall make the following additional assumptions:

(i) The ring of void surface lying in the grain boundary, which acts as a source of diffusing atoms has a radial width w, about equal to that of one atomic layer (see fig. 10). The atoms are released uniformly from within this volume.

(ii) The atoms are deposited uniformly over the grain boundary, so as to minimize lattice strains.

(iii) The void retains its spherical shape throughout its growth. It must be pointed out that whilst there is mechanism available (i.e. surface diffusion) for doing this, a sphere is not the equilibrium shape for a void under the conditions that have been postulated. Owing to the presence of the other voids the natural shape of its grain-boundary cross section is a deformed circle with bulges towards the corners of the unit square.

These become more predominant as the void grows. In order to retain a circular cross section it is necessary to impose small restraining forces on the void. In view of the other approximations necessary in this problem it has been thought permissible to assume that the bubbles remain spherical, yet ignore the forces holding them to this shape. Although the effect of this on the final result is unimportant, it will be seen later that it produces some slight inconsistencies in the mathematics which have been accepted in view of the great simplification in the working that has resulted.

Fig. 10

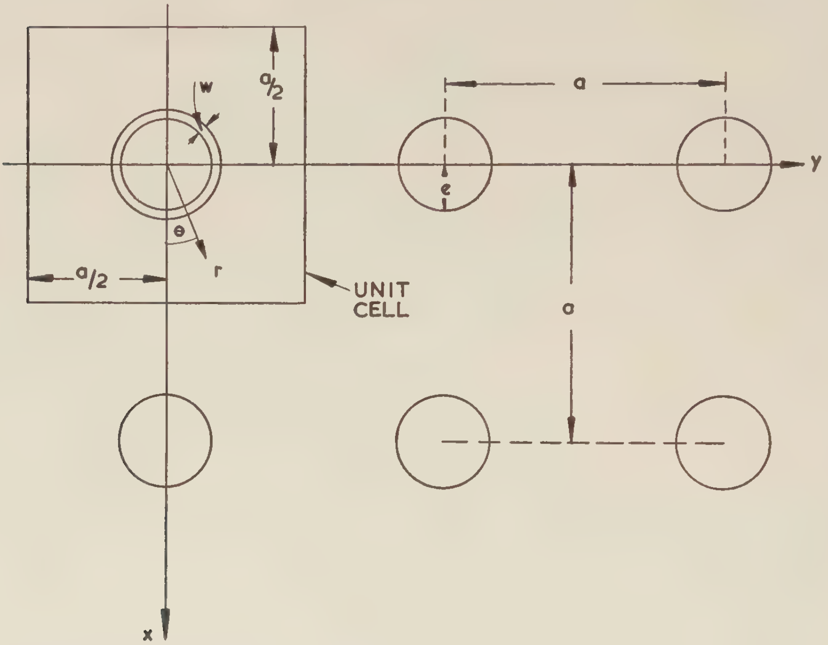

Cross section through voids lying in the plane of the grain boundary.

Let us consider a unit cell centred on the origin and defined by

$$|x| \leqslant \tfrac{1}{2}a,$$
$$|y| \leqslant \tfrac{1}{2}a.$$

$\nabla^2 f$ is a measure of the strength of a given point as a source of or sink for atoms. In view of assumption (i) and (ii) above it is determined (apart from a scaling factor) at all points inside the unit cell since we have,

$$\left.\begin{aligned} \nabla^2 f &= 0 \quad \text{when} \quad 0 < r < \rho, \\ \nabla^2 f &= A \quad \text{when} \quad \rho < r < \rho + w, \\ \nabla^2 f &= B \quad \text{when} \quad r > \rho + w, \end{aligned}\right\} \qquad (1)$$

where A and B are related by the equation,

$$B(a^2 - \pi\rho^2) + Aw \cdot 2\pi\rho = 0 \qquad (2)$$

as the total number of atoms is constant.

But $\nabla^2 f$ has periodicity a in x, y, and may be written in the form

$$\nabla^2 f = \sum_{m=-\infty}^{+\infty} \sum_{n=-\infty}^{+\infty} C_{mn} \cos\frac{2\pi}{a}(mx+ny) \qquad . \quad . \quad . \quad (3)$$

where

$$C_{mn} = \frac{1}{a^2}\int_{-\frac{1}{2}a}^{+\frac{1}{2}a}\int_{-\frac{1}{2}a}^{+\frac{1}{2}a} \nabla^2 f \cos\frac{2\pi}{a}(mx+ny)\,dx\,dy$$

$$= \frac{B}{a^2}\int_{-\frac{1}{2}a}^{+\frac{1}{2}a}\int_{-\frac{1}{2}a}^{+\frac{1}{2}a} \cos\frac{2\pi}{a}(mx+ny)\,dx\,dy - \frac{B}{a^2}\int_0^{\rho+w}\int_0^{2\pi} \cos\frac{2\pi r}{a}(m\cos\theta+n\sin\theta)\,d\theta\,r dr$$

$$+\frac{A}{a^2}\int_0^{\rho+w}\int_0^{2\pi}\cos\frac{2\pi r}{a}(m\cos\theta+n\sin\theta)\,d\theta\,r dr,$$

from eqns. (1).

Assuming $w \ll \rho$,

$$C_{mn} = (B \text{ or } 0) - \frac{\rho B}{a(m^2+n^2)^{1/2}} J_1\left(\frac{2\pi\rho(m^2+n^2)^{1/2}}{a}\right) + \frac{2\pi A\rho w}{a^2} J_0\left(\frac{2\pi\rho(m^2+n^2)^{1/2}}{a}\right) \qquad . \quad . \quad . \quad . \quad (4)$$

where the first term is B if $m=n=0$ and zero otherwise.

Hence

$$C_{00} = B - \frac{\rho B}{a}\frac{\pi\rho}{a} + \frac{2\pi A\rho w}{a^2} = B\left(1-\frac{\pi\rho^2}{a^2}\right) + \frac{2\pi\rho w}{a^2}A = 0$$

from eqn. (2). Otherwise,

$$\frac{C_{mn}}{B} = -\frac{\rho}{a(m^2+n^2)^{1/2}} J_1\left(\frac{2\pi\rho(m^2+n^2)^{1/2}}{a}\right) - \left(1-\frac{\pi\rho^2}{a^2}\right) J_0\left(\frac{2\pi\rho(m^2+n^2)^{1/2}}{a}\right). \qquad . \quad . \quad . \quad (5)$$

The most general integral of eqn. (3) which has the required symmetry is

$$f = -\frac{a^2}{4\pi^2}\sum_m\sum_n \frac{C_{mn}}{(m^2+n^2)}\cos\frac{2\pi}{a}(mx+ny) + K \qquad . \quad . \quad (6)$$

where K is a constant, obtained from the condition,

$$f = -\sigma_n\Omega. \qquad . \quad . \quad . \quad . \quad . \quad . \quad . \quad . \quad . \quad (7)$$

σ_n will vary over the unit cell owing to the stress concentration set up round the void. However, the total force over the unit cell due to the applied stress and pressure must be $(\sigma-P)a^2$.

Hence integrating eqn. (7) over a unit cell and allowing for surface tension,

$$\Omega[2\pi\rho\gamma - (\sigma-P)a^2] = \int_{-\frac{1}{2}a}^{+\frac{1}{2}a}\int_{-\frac{1}{2}a}^{+\frac{1}{2}a} f\,dx\,dy - \int_0^{\rho}\int_0^{2\pi} fr\,d\theta\,dr. \qquad . \quad . \quad (8)$$

On physical grounds we may expect f to have the value $-2\gamma\Omega/\rho$ at all points inside the void. If it were calculated from eqn. (6) this result would not be obtained because the restoring forces round the void have been neglected. $-(2\gamma\Omega/\rho)$ will in fact be the mean value inside the region and for the purposes of carrying out the second integration in eqn. (8) we shall take it as constant. The origin is one of the positions which has the mean value, a fact which will be used later. Hence

$$\Omega[2\pi\rho\gamma-(\sigma-P)a^2]=Ka^2+\frac{2\gamma\Omega}{\rho}\,.\,\pi\rho^2$$

giving

$$K=-\Omega(\sigma-P).$$

Hence
$$f=-\frac{a^2}{4\pi^2}\sum_m\sum_n\frac{C_{mn}}{(m^2+n^2)}\cos\frac{2\pi}{a}(mx+ny)-\Omega(\sigma-P). \quad . \quad . \quad (9)$$

Assuming a radial flow of atoms at the void surface which is reasonable if $\rho \ll a$ the diffusion flux is given by,

$$j=-\frac{D_g}{kT\Omega}\left(\frac{\partial f}{\partial r}\right)_{r=\rho+w}.$$

If we let $w \to 0$ and evaluate $(\partial f/\partial r)$ at $r=\rho$ it must be remembered that $(\partial f/\partial r)$ is now discontinuous at this point (see fig. 11) and the value required is the maximum (numerically) which is equal to twice that obtained by computing the Fourier sum at $r=\rho$.

Fig. 11

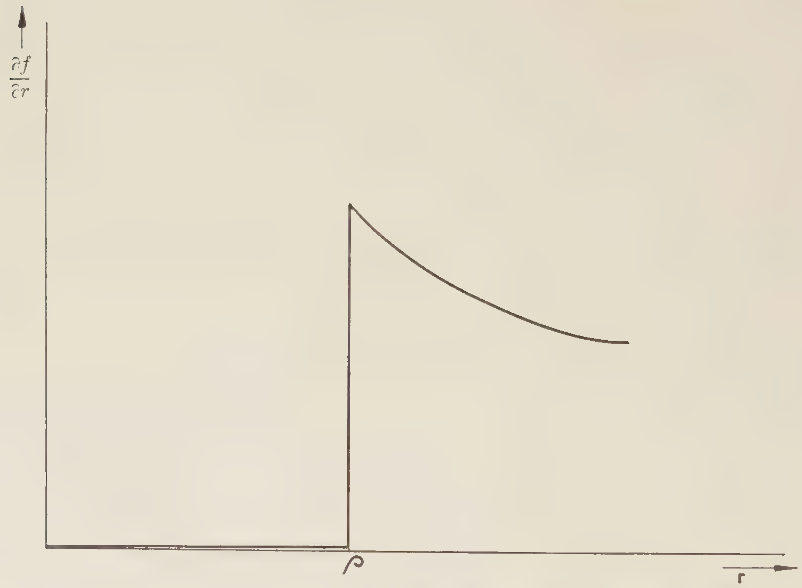

Approximate radial variation of gradient of chemical potential.

Changing to polar coordinates,

$$f=-\frac{a^2}{4\pi^2}\sum_m\sum_n\frac{C_{mn}}{(m^2+n^2)}\cos\left\{\frac{2\pi r}{a}(m\cos\theta+n\sin\theta)\right\}-(\sigma-P)\Omega,$$

$$\left(\frac{\partial f}{\partial r}\right)_{r=\rho}=\frac{a}{2\pi}\sum_m\sum_n\frac{C_{mn}(m\cos\theta+n\sin\theta)}{m^2+n^2}\sin\left\{\frac{2\pi\rho}{a}(m\cos\theta+n\sin\theta)\right\}.$$

The number of atoms, per second, coming out of an elementary area $\rho d\theta\delta z$ of void is,

$$-\frac{2D_g\rho d\theta\delta z}{kT\Omega}\left(\frac{\partial f}{\partial r}\right)_\rho .$$

Therefore, the rate at which atoms leave the void is given by,

$$\begin{aligned}\frac{dN}{dt}&=-\frac{2\rho(D_g\delta z)}{kT\Omega}\int_0^{2\pi}\left(\frac{\partial f}{\partial r}\right)_{r=\rho}d\theta\\&=-\frac{2(D_g\delta z)\rho a}{kT\Omega}\sum_m\sum_n\frac{C_{mn}}{(m^2+n^2)^{1/2}}J_1\left(\frac{2\pi\rho(m^2+n^2)^{1/2}}{a}\right).\end{aligned}\tag{10}$$

The coefficients C_{mn} are not known, but C_{mn}/B is given in eqn. (5). However, as stated earlier the value of f is known at the centre of the void.

Substituting

$$f=-\frac{2\gamma\Omega}{\rho}\quad\text{when}\quad x=y=0$$

into eqn. (9) gives

$$\frac{dN}{dt}=\frac{2(D_g\delta z)\rho}{kT}\frac{4\pi^2}{a}\left(\sigma-P-\frac{2\gamma}{\rho}\right)\cdot S$$

where

$$S=\sum_m\sum_n\frac{C_{mn}/B}{(m^2+n^2)^{1/2}}J_1\left(\frac{2\pi\rho}{a}(m^2+n^2)^{1/2}\right)\Big/\sum_m\sum_n\frac{C_{mn}}{B(m^2+n^2)}.$$

The rate of change of void radius is,

$$\frac{d\rho}{dt}=\frac{\Omega}{4\pi\rho^2}\cdot\frac{dN}{dt}=\frac{2\pi\Omega(D_g\delta z)(\sigma-P-2\gamma/\rho)S}{kTa\rho}.$$

The time to fracture is obtained by integrating this expression between $\rho=\rho_0$ and $\rho=\frac{1}{2}a$. S is a function of ρ/a only, and has been calculated for a set of values in the expected range of integration. These suggest that the approximation $S=1$ may be used as it only deviates significantly from this value for a short time just before the voids coalesce.

This gives,

$$\frac{2\pi\Omega(D_g\delta z)}{kTa}\int_0^{t_r}dt=\int_{\rho_0}^{\frac{1}{2}a}\frac{\rho d\rho}{\sigma-P-2\gamma/\rho}$$

where t_r = time to failure.

On integrating and assuming $\rho_0\ll a$, we obtain

$$t_r=\frac{kTa}{2\pi\Omega(D_g\delta z)(\sigma-P)}\left\{\frac{a^2}{8}+\frac{\gamma a}{(\sigma-P)}+\frac{4\gamma^2}{(\sigma-P)^2}\ln\left[\frac{\frac{1}{2}a(\sigma-P)-2\gamma}{\rho_0(\sigma-P)-2\gamma}\right]\right\}.\tag{11}$$

The Lattice Thermal Conductivity of Dilute Alloys of Silver and Gold†

By G. K. White‡, S. B. Woods and M. T. Elford§

[Received January 6, 1959]

Abstract

The thermal conductivity of certain alloys was measured on samples which had been carefully annealed to reduce the concentration of dislocations. After subtraction of an electronic component estimated from the residual electrical resistivity, the remainder was proportional to T^2 below 10°K, and agreed with Makinson's calculation of the lattice conductivity, assuming that lattice waves of all three polarizations interact equally with conduction electrons.

The lattice thermal conductivity, λ_g, of metals at low temperatures appears to be limited by electron scattering of the lattice waves or phonons and measurements of λ_g may therefore yield information about the electron–phonon interaction (Klemens 1954 a, 1956). The lattice conductivity of pure metals cannot be measured directly because of the dominance of λ_e, the electronic component of thermal conductivity, but it can be deduced under certain assumptions from measurements on dilute alloys in which the two conductivity components may be comparable. Studies, below about 100°K, of the electrical and thermal conductivities of silver alloys (Kemp *et al.* 1954, 1956), of copper alloys (White and Woods 1954, Kemp, Klemens and Tainsh 1957, Kemp, Klemens, Tainsh and White, 1957) and of a gold alloy (Birch *et al.* 1958) have yielded values for the lattice thermal conductivity of silver, copper and gold. These values lead to the conclusion that the interaction of the conduction electrons with transverse lattice waves is almost as strong, if not as strong, as with longitudinal waves.

Unfortunately the interactions of lattice waves with dislocations and with conduction electrons produce components of thermal resistance which vary in the same way ($\propto T^{-2}$) with temperature. Thus, if there is an appreciable number of dislocations in the specimens, it is only possible to set an upper limit to the thermal resistance produced by the electrons. Although annealing at high temperature may substantially reduce the dislocation density, it is possible that many dislocations become immobile in alloys having large concentrations of solute atoms. However, in sufficiently dilute alloys suitable annealing should remove all but a negligible number of dislocations. Some years ago measurements were made on a dilute solution of iron in copper (White and Woods 1954) and this work has now been extended to dilute alloys of iron in gold and tin in silver.

---

† Communicated by the Authors.

‡ Now at Division of Physics, C.S.I.R.O., Sydney, Australia.

§ National Research Laboratories Postdoctorate Fellow.

The apparatus and techniques described by White and Woods (1955) were used to measure the electrical and thermal conductivities of the specimens between 2 and 150°K. The alloys were vacuum cast from the constituent metals and homogenized in this laboratory and were then swaged† to form rods which were finally sealed in evacuated quartz tubes and annealed. Leads were connected to the specimens with a bismuth–cadmium solder which does not become superconducting above 1°K.

Table 1. Some Physical Data for the Specimens

Specimen	Solute (at.%)	Length (cm)	Diameter (mm)	Anneal	ρ_{295} ($\mu\Omega$ cm)	ρ_0 ($\mu\Omega$ cm)	W_0T W^{-1} cm deg^2
Au 1	0·13% Fe	6·48	2·31	15 hrs 700°C	3·44	$1{\cdot}18_4$	48·3
Ag 1	0·14% Sn	6·10	2·45	15 hrs 700°C	2·32	$0{\cdot}72_4$	29·7
Ag 2	0·3% Sn	4·57	4·49	150 hrs 760°C	2·69	1·05	42·7

Some physical data for the specimens are given in table 1. To check the compositions, part of each alloy was chemically analysed after being annealed. Also the electrical resistance values measured at 295°K and in the liquid helium range were compared with the measurements by Linde (1939) on alloys to estimate the solute concentration (Gerritsen 1956).

The total thermal conductivity of the alloys is given by the sum of the electronic and lattice components,

$$\lambda=\lambda_e+\lambda_g \qquad \text{. . . . .} \qquad (1)$$

where the electronic thermal resistivity is

$$1/\lambda_e=W_e=W_0+W_i. \qquad \text{. . . . . . .} \qquad (2)$$

The ideal electronic thermal resistivity, W_i, which arises from electron scattering by lattice vibrations, is assumed to be the same as that of the pure parent metal. The residual electronic thermal resistivity, W_0, due to impurity scattering, should be related at temperature T to the residual electrical resistance, ρ_0, by the relation

$$\rho_0/W_0T=L_0 \qquad \text{. . . . .} \qquad (3)$$

where the Lorenz number, $L_0=2{\cdot}45\times10^{-8}$ watt ohm/deg^2. At temperatures below about 20°K, $W_i\ll W_0\equiv 1/\lambda_0$, and thus $\lambda=\lambda_0+\lambda_g$. Since we expect $\lambda_g=\text{constant}\times T^2$ (see Makinson 1938, Klemens 1954 a) at low temperatures where the lattice waves are scattered mainly by electrons, λ/T plotted versus T should yield a straight line with intercept λ_0/T at $T=0$. The values of W_0T given in table 1 are obtained in this way and agree within about 1% with the values obtained from eqn. (3). Values for W_i were taken from measurements on pure gold (White 1953 a, Rosenberg 1955) and on pure silver (White 1953 b, Rosenberg 1955). Using eqn. (2) we were then able to deduce λ_e and hence, with eqn. (1), λ_g. The results are shown in fig. 1 for gold and fig. 2 for silver.

---

† We are indebted to Mr. J. A. Perry of the Mines Branch, Department of Mines and Technical Surveys, Government of Canada for arranging to have the alloys swaged in his department.

It can be seen that below about 10°K the lattice conductivity does indeed vary as T^2 and the constant $\lambda_g T^{-2}$ derived from the results in this region may be compared with theoretical values. Klemens (1954 a) has derived two values theoretically—one on Makinson's (1938) assumption that the electrons interact equally with lattice waves of all three polarizations, the other adopting the Bloch model in which interactions occur with the longitudinal waves only.

Fig. 1

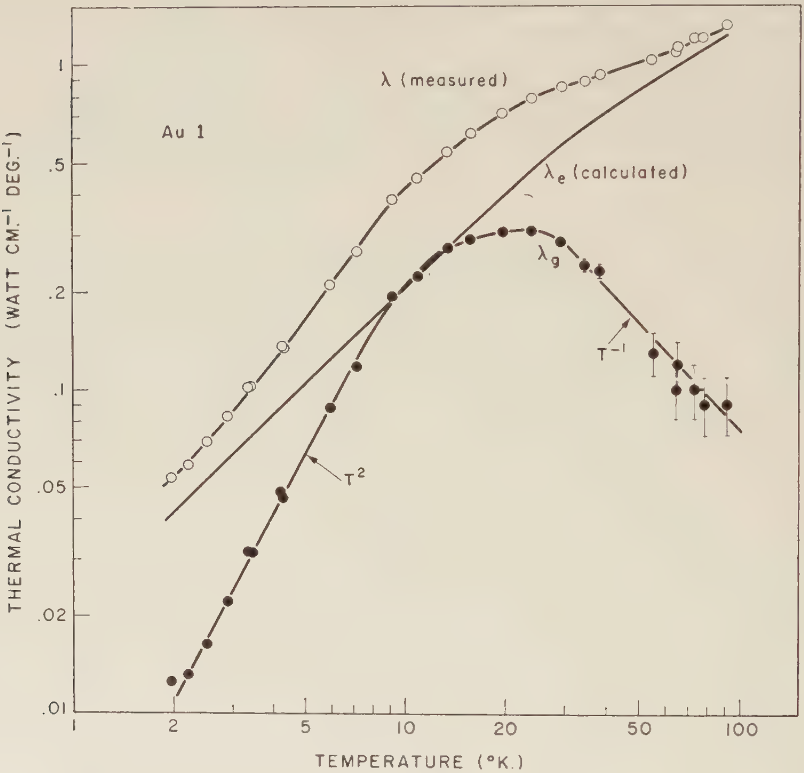

Thermal conductivity of gold–iron alloy.

Makinson's coupling scheme results in a lattice conductivity about twenty times higher than that given by Bloch coupling and, although an electron interaction with transversely polarized waves intermediate between these two extremes would lead to intermediate conductivity values, it is apparent from table 2 that the experiments support Makinson's hypothesis very closely. This result generally confirms earlier work on less dilute alloys, the present values of $\lambda_g T^{-2}$ being only a few per cent greater than the maximum values obtained earlier of about $1{\cdot}9 \times 10^{-3}$ for Ag (+2% Cd) by Kemp *et al.* (1956) and a recent value of $2{\cdot}6 \times 10^{-3}$ for Au (+0·7% Pt, annealed 750°C and 1050°C) by Birch, Kemp, Klemens and Tainsh (to be published). This supports the thesis that provided the solute content is less than of the order of 1% and the alloy is annealed under normal conditions, then insufficient dislocations are locked into the alloy to noticeably affect the measured lattice conductivity. Hence a value of $\lambda_g T^{-2}$ (or $W_g T^2$) representative of phonon–electron interaction is obtained in these dilute alloys.

Fig. 2

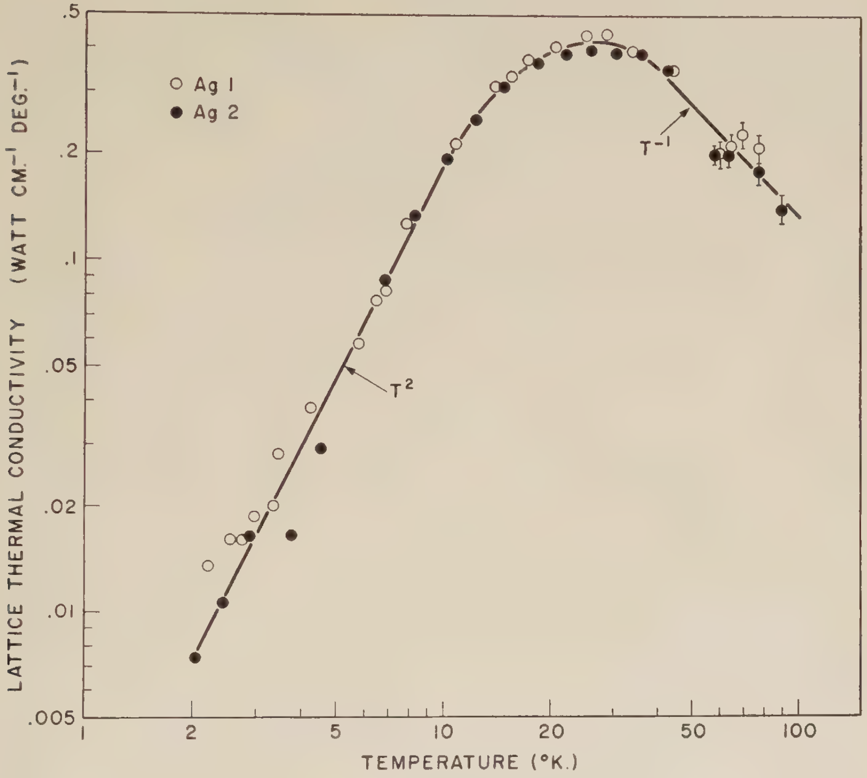

Lattice thermal conductivity of silver–tin alloy.

Near liquid air temperatures scattering of the lattice waves either by mutual interactions due to anharmonicity or by point imperfections should lead to $\lambda_g \propto T^{-1}$. The observed lattice conductivity exhibits this temperature dependence but is smaller than theoretical estimates by a factor of four or five (see White and Woods (1958) for a discussion of anharmonicity theories; Klemens (1956) for point scattering theory). Although uncertainties in the theoretical estimates make it difficult to draw conclusions

Table 2. Experimental and Theoretical Lattice Conductivity at Low Temperatures ($\lesssim 10°\text{K}$)

Metal	$\lambda_g T^{-2}$ (watt cm^{-1} deg^{-3})		
	Experimental	Makinson	Bloch
Gold	$2{\cdot}8 \times 10^{-3}$	$2{\cdot}9 \times 10^{-3}$	$1{\cdot}5 \times 10^{-4}$
Silver	$2{\cdot}0 \times 10^{-3}$	$2{\cdot}3 \times 10^{-3}$	$1{\cdot}2 \times 10^{-4}$
Copper	$1{\cdot}8 \times 10^{-3}$†	$1{\cdot}4 \times 10^{-3}$	$7{\cdot}2 \times 10^{-5}$

† See White and Woods 1954.

from this comparison it may be worth noting that in the inert gas solids, which also have a cubic lattice structure, somewhat better agreement is obtained (White and Woods, 1948) with the anharmonic interaction theories.

Acknowledgments

We are grateful to Mr. W. Fisher for preparing the samples, to Mr. W. Stockdale for the chemical analyses and to Messrs. F. Richardson and J. Broome for keeping us supplied with liquid helium. We also wish to thank Dr. Z. S. Basinski and Dr. W. B. Pearson for metallurgical advice and Dr. D. K. C. MacDonald for helpful criticism of the manuscript.

References

Birch, J. A., Kemp, W. R. G., and Klemens, P. G., 1958, *Proc. phys. Soc. Lond.*, **71**, 843.

Birch, J. A., Kemp, W. R. G., Klemens, P. G., and Tainsh, R. J., 1959 (to be published).

Gerritsen, A. N., 1956, *Handbuch der Physik*, **19**, 137 (Berlin : Springer-Verlag).

Kemp, W. R. G., Klemens, P. G., Sreedhar, A. K., and White, G. K., 1954, *Proc. phys. Soc. Lond.* A, **67**, 728 ; 1956, *Proc. roy. Soc.* A, **233**, 480.

Kemp, W. G. R., Klemens, P. G., and Tainsh, R. J., 1957, *Aust. J. Phys.*, **10**, 454.

Kemp, W. R. G., Klemens, P. G., Tainsh, R. J., and White, G. K., 1957, *Acta Met.*, **5**, 303.

Klemens, P. G., 1954 a, *Aust. J. Phys.*, **7**, 57 ; 1956, *Handbuch der Physik*, **14**, 4 (Berlin : Springer-Verlag).

Linde, J. O., 1939, *Thesis*, Lund University.

Makinson, R. E. B., 1938, *Proc. Camb. phil. Soc.*, **34**, 474.

Rosenberg, H. M., 1955, *Phil. Trans. roy. Soc.*, **247**, 441.

White, G. K., 1953 a, *Proc. phys. Soc. Lond.* A, **66**, 559 ; 1953 b, *Ibid.*, **66**, 844.

White, G. K., and Woods, S. B., 1954, *Phil. Mag.*, **45**, 1343 ; 1955, *Canad. J. Phys.*, **33**, 58 ; 1958, *Phil. Mag.*, **3**, 785.

The Yield Point of a Super-lattice†

By N. Brown
University of Pennsylvania and Cavendish Laboratory (Guggenheim Fellow 1958–1959)

[Received January 8, 1959]

Abstract

A completely theoretical calculation was made of the dependence of the yield point on the degree of long-range order in an AB b.c.c. super-lattice. The resulting equation is

$$\tau = NkTS_0^2/4b$$

where T is temperature, and S_0 is degree of long-range order. For β-brass a maximum in τ at 515°K of $0{\cdot}54 \times 10^9$ dynes/cm² is predicted; the experimentally observed values are 493°K and $0{\cdot}36 \times 10^9$ dynes/cm².

A sharp increase in τ was observed near T_c; it is associated with short-range order strengthening as predicted by Sumino.

The width of an anti-phase domain boundary was also calculated. For $T > 0{\cdot}5T_c$ the width is given by the equation

$$\text{width} = \tfrac{1}{2}\pi[T_c/(T_c - T)]^{1/2} + \tfrac{1}{2}.$$

§ 1. Introduction

The idea of the super-dislocation in a super-lattice was first presented by Koehler and Seitz in 1947.

The effect of long-range order on the yield point was first discussed quantitatively by Cottrell (1954), who considered the size effect of an anti-phase domain. The Cottrell equation is

$$\tau = \gamma l^{-1}(1 - \alpha a l^{-1}) \quad . \quad . \quad . \quad . \quad . \quad . \quad . \quad . \quad . \quad (1)$$

where τ is yield stress, γ is surface energy of a domain boundary, l is size of the domain, a is width of the boundary, and $\alpha \simeq 6$ is a shape factor. The equation is based on the idea that the external work τl equals the change in energy on the slip plane from $\gamma \alpha a l^{-1}$ to γ. Equation (1) predicts a maximum in the yield point at a domain size of about 20 A°. Implicit in eqn. (1) is the assumption that yielding is associated with a shear displacement of $l/2$ along the slip plane. In general, it would be expected for large l that the strain would be so large after a shear of $l/2$ that the resulting stress would be more closely associated with a flow stress rather than a yield point. Consequently, eqn. (1) should be restricted to small values of l.

A recent theory by Sumino (1958) considered two effects: (1) the disordering of short-range order as proposed by Fisher (1954) and (2) the interaction of the stress field of the dislocation with the change in nearest neighbour distance caused by ordering. The disordering of short-range order is the larger of the two effects and its corresponding yield rises very rapidly as the temperature approaches T_c from above. The other effect is such that screw dislocations are much easier to move than edges, and its corresponding yield stress is a maximum at T_c.

---

† Communicated by the Author.

Fig. 1

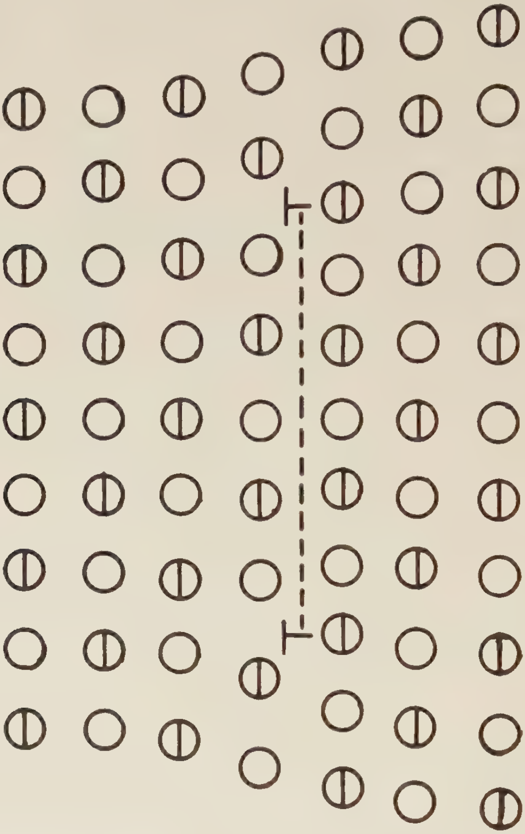

Paired dislocations joined by an anti-phase boundary.

Ardley and Cottrell (1953) proposed that in the super-lattice the stable dislocation consists of a pair of equal dislocations joined by an anti-phase boundary (fig. 1). The equilibrium configuration of such a super-dislocation was calculated by Brown and Herman (1956) for an AB b.c.c. super-lattice. Neglecting the entropy, the equilibrium spacing for two edge dislocations is

$$r = 4Gb^4/3\sqrt{2}\pi(1-\nu)kT_cS_0^2. \qquad . \quad . \quad . \quad . \quad . \quad (2)$$

When S_0, the degree of long-range order, is equal to unity, r becomes 32 Burgers vectors for β-brass, and the energy of the anti-phase domain boundary 82 ergs/cm^2. The stress to move a super-dislocation has been discussed many times but a concrete theory has not been proposed. The general attitude indicated that the stress to move a super-dislocation should not be appreciably greater than for an ordinary one because the trailing dislocation should re-order the disorder produced by the leading one. In this paper the nature of the anti-phase domain boundary in the super-dislocation is investigated further; and it turns out that the stress required to move it may be very large. The new mechanism of yielding predicts a maximum in the yield point as a function of the degree of long-range order. It is interesting that all quantitative theories (Cottrell 1954, Sumino 1958) involving the effect of long-range order on yield point predict a maximum. Experimental data are presented which support the new theory and which also indicate that the effect predicted by Sumino is observed near T_c.

§ 2. Theory

It is a geometrical necessity that an anti-phase domain boundary starts or terminates at a dislocation. In the AB b.c.c. type of super-lattice every anti-phase boundary which starts at any $\frac{1}{2}[111]$ dislocation can be terminated by any other $\frac{1}{2}[111]$ dislocation. The same generalization does not hold for a f.c.c. super-lattice because it has four kinds of lattice site whereas the b.c.c. lattice has only two. The present theory will be confined to the AB b.c.c. lattice and this will be directly comparable with the Sumino theory. In general, dislocations not on the same plane can be joined by a curve anti-phase boundary; this case will not be considered because the stress to move these dislocations is much greater than for the case where the dislocations are in the same slip plane. In fig. 2 (*a*) the super-dislocation consists of two edges on different slip planes, and when it slips, the anti-phase boundaries AA′ and BB′ are generated. In accordance with Fisher's equation, the required stress is

Fig. 2

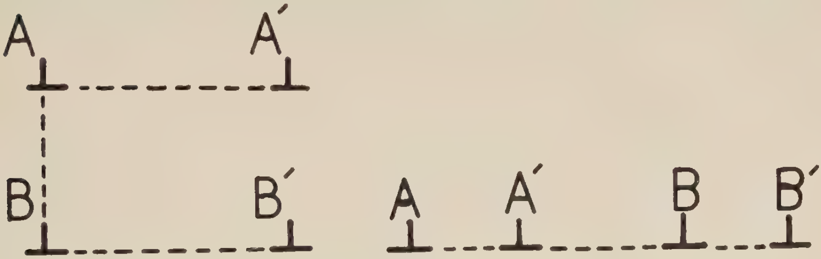

(*a*) (*b*)

(*a*) Movement of paired dislocation not on same slip plane. AB is initial position; A′B′ is position after slip.

(*b*) Movement of paired on same slip plane. AB is initial and A′B′ is position after slip.

$$\tau = E_{\mathrm{AA}'}/b \qquad (3)$$

where $E_{AA'}$ is the surface energy of AA′ or BB′. In fig. 2 (*b*) the super-dislocation lies on the same slip plane and the stress required for slip is

$$\tau=(E_{BB'}-E_{AA'})/2b \quad \ldots\ldots\ldots \quad (4)$$

where $E_{BB'}$ and $E_{AA'}$ are the surface energies produced by the slip of the leading and trailing dislocation respectively. Consequently if, as it has been assumed in the past, $E_{BB'}=E_{AA'}$, then no additional stress is required to move a super-dislocation. The main purpose of this paper is to prove that the stress to move a super-dislocation is in general not equal to zero. The proof requires that the anti-phase boundary generated by slip in the absence of diffusion is significantly different from an anti-phase boundary formed under thermal equilibrium (fig. 3). The boundary formed by slip is a step-function, but the one formed under thermal equilibrium is smoothly varying above 0°K as demanded by considerations of the entropy. Consequently, there is a difference in order on the slip plane of the two types of anti-phase boundaries. Since the degree of order determines the surface energies in eqn. (4), the stress to move a super-dislocation is in general not equal to zero except when the equilibrium order is unity or zero. Therefore, a maximum in the stress is expected at some intermediate degree of order. In order to determine the yield point we need to know the width of the anti-phase domain boundary formed under thermal equilibrium.

Fig. 3

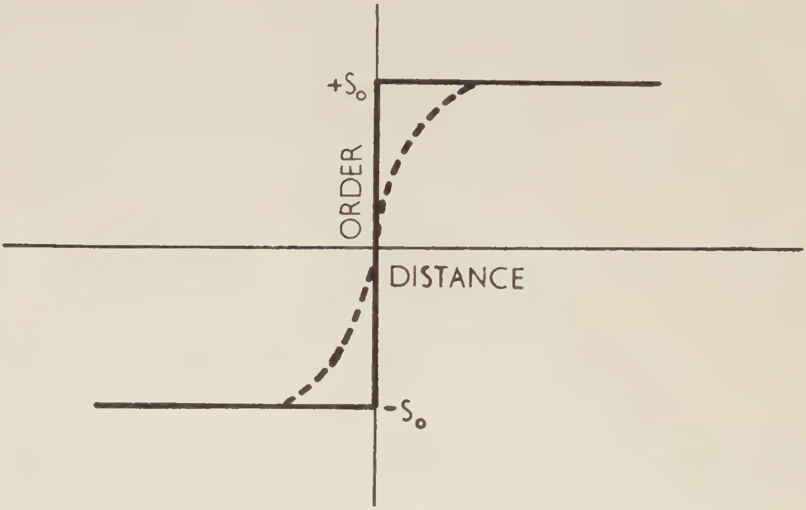

Width of anti-phase boundary showing order versus distance from slip interface. Full line is anti-phase boundary generated by slip of a single dislocation. Dotted line is an anti-phase boundary formed under thermal equilibrium.

§ 3. CALCULATION OF WIDTH OF ANTI-PHASE BOUNDARY

A one-dimensional calculation will be made in which it is assumed that the order is constant along planes parallel to the slip plane. Obviously, the assumption breaks down at the core of the dislocation, and the assumption is more valid the more extended the super-dislocation. Equation (2) as applied to CuZn indicated that the minimum spacing at order $S_0 = 1$ was $32b$; therefore the one-dimensional calculation is expected to give results which have physical significance. Using the Bragg–Williams parameter for long-range order, the fraction of A atoms on α sites of the nth plane from the slip interface is given by

$$\tfrac{1}{2}/(1 - S_n).$$

Considering only nearest neighbour interactions the energy per unit area of anti-phase boundary is given by

$$E = 2N\left\{\left(2\sum_{n=1}^{n=n_\infty} 1 + \tfrac{1}{2}\right)(2V_{\mathrm{AB}} + V_{\mathrm{AA}} + V_{\mathrm{BB}}) + \left(\sum_{n=1}^{n=n_\infty} S_n{}^2 + S_n S_{n+1} - \tfrac{1}{2}S_1{}^2\right)(2V_{\mathrm{AB}} - V_{\mathrm{AA}} - V_{\mathrm{BB}})\right\} \quad . \quad (5)$$

where $2N$ is the density of atoms on the (110) plane, V_{AA}, V_{BB}, and V_{AB} are the energy of the bonds between A–A, B–B, and A–B atoms; and $S_{n_\infty} = S_0$, the degree of long-range order in the perfect crystal under thermal equilibrium. In deriving eqn. (5) the widths of anti-phase domain boundary on both sides of the slip interface are included ($S_n = -S_{-n}$). The entropy per unit area of anti-phase boundary is

$$S = 2k \sum_{n=1}^{n=n_\infty} \log\{N!/\tfrac{1}{2}(1 - S_n)N!\,\tfrac{1}{2}(1 + S_n)N!\}. \quad . \quad . \quad . \quad (6)$$

The free energy is given by

$$F = E - TS. \quad . \quad . \quad . \quad . \quad . \quad . \quad . \quad . \quad . \quad (7)$$

Substituting eqns. (5) and (6) in (7) and setting $\partial F/\partial S_n = 0$, the following values of S_n at thermal equilibrium result:

$$S_1 + S_2 = 2T/T_c \log(1 + S_1)/(1 - S_1)$$

for $n > 1$ $$S_{n-1} + 2S_n + S_{n+1} = 2T/T_c \log(1 + S_n)/(1 - S_n) \quad . \quad . \quad . \quad (8)$$

where $$kT_c = -2(2V_{\mathrm{AB}} - V_{\mathrm{AA}} - V_{\mathrm{BB}}).$$

Equations (8) reduce to the well-known equation (Kittel 1953)

$$S_0 = T/2T_c \log(1 + S_0)/(1 - S_0) \quad . \quad . \quad . \quad . \quad . \quad . \quad (9)$$

where S_0 is the equilibrium degree of long-range order in the perfect crystal. The exact solution of eqns. (8) over the entire temperature range, 0°K–T_c, can only be obtained by numerical methods. However, since the higher temperatures are of the greatest interest, a high temperature approximation will be used which leads to a simple solution and which was found to agree closely with more exact calculations down to about $0{\cdot}5T_c$.

At high temperatures where $S_0 \ll 1$ eqns. (8) transform to the differential equation

$$4S + a^2 d^2S/dX^2 = 4TS/T_c \quad . \quad . \quad . \quad . \quad . \quad . \quad . \quad (10)$$

where S_n transforms to $S(X)$, a is the distance between (110) planes, and X is the coordinate perpendicular to the slip interface. From fig. 3 the boundary conditions are $S=0$ at $X=0$ and $ds/dX=0$ at $S=S_0$. A sinusoidal solution is indicated.

$$S = S_0 \sin pX\,;\; p^2 = 4(T_c - T)/a^2T_c. \quad . \quad . \quad . \quad . \quad . \quad (11)$$

The width of the anti-phase domain boundary is determined by the condition

$$p(n_\infty - 1/2)a = 1/2\pi$$

and $2n_\infty$, the number of atomic planes in the boundary, is

$$2n_\infty = 1/2\pi[T_c/(T_c - T)]^{1/2} + 1/2 \quad . \quad . \quad . \quad . \quad . \quad . \quad (12)$$

n_∞ behaves properly because $n \simeq 2$ when $T=0$ and $n_\infty \to \infty$ when $T \to T_c$. At $0{\cdot}975\,T_c$ where $S_0 = 0{\cdot}5$ $2n_\infty \simeq 10$. Thus, the width of the anti-phase domain boundary is generally very narrow except very close to T_c. As far as the author knows the above calculation represents the first one for the width of an anti-phase boundary. A more accurate solution of eqns. (8) was made by approximating the region of $S \ll 1$ with a sine function and the region of $(S_0 - S) \ll 1$ with an exponential. The two solutions were matched at a slope of $\tan \pi/4$. The increased accuracy over the purely sinusoidal approximation was found to be small and not worth the loss of simplicity in the light of the major approximation involving only nearest neighbour interactions.

§ 4. STRESS TO MOVE THE SUPER-DISLOCATION

The stress to move the super-dislocation is calculated from eqn. (4), where (Brown and Herman 1956)

$$E_{\mathrm{BB'}} = 1/2NkT_cS_0^2 \quad . \quad . \quad . \quad . \quad . \quad . \quad . \quad (13\,a)$$

and

$$E_{\mathrm{AA'}} = 1/2NkT_cS_1^2 \quad . \quad . \quad . \quad . \quad . \quad . \quad . \quad . \quad (13\,b)$$

where S_1 is the degree of order at $X=a/2$ (the slip plane). From eqn. (11)

$$\left.\begin{aligned} S_1 &= S_0 \sin\,[(T_c - T)/T_c]^{1/2}, \\ S_1^2 &\simeq S_0^2(T_c - T)/T_c \quad \text{for} \quad T > 0{\cdot}5T_c. \end{aligned}\right\} \quad . \quad . \quad . \quad . \quad (14)$$

Substituting eqns. (13) and (14) in (4)

$$\tau = NkTS_0^2/4b \quad . \quad . \quad . \quad . \quad . \quad . \quad . \quad . \quad . \quad . \quad (15)$$

where τ is the stress to move a super-dislocation. τ is plotted against T in fig. 4, for the case of CuZn where S_0 was obtained from X-ray data by Chipman and Warren (1950), $N = 8{\cdot}2 \times 10^{14}$ atoms/cm^2 $k = 1{\cdot}4 \times 10^{-16}$ ergs/°K and $b = 2{\cdot}57 \times 10^{-8}$cm. A very sharp maximum appears at 515°K, where the yield point becomes $0{\cdot}54 \times 10^9$ dynes/cm^2. In comparing the above theory with the experimental data it must be remembered that it was assumed that slip occurred in the absence of diffusion and also the effect of thermal fluctuations in reducing the yield point was neglected. These effects are expected to reduce the yield point but are not expected to cause much of a change in the temperature at which the maximum yield point is observed.

Fig. 4

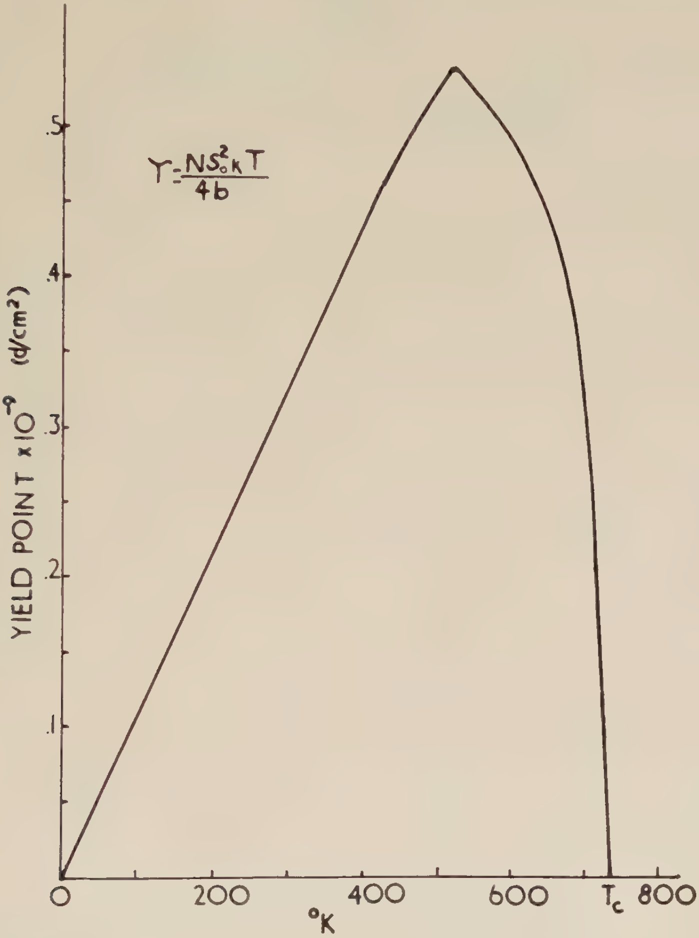

Theoretical curve of yield point versus temperature in region of long range order.

§ 5. Experimental Data

Two compositions of β-brass were used of 48·6 and 49·9 at. % Zn. The tensile specimens were 6·4 mm in diameter and were both polycrystalline and single crystals. The yield points were determined on the Instron machine. For temperatures above room temperature the specimens were in air surrounded by a furnace, and below room temperature the specimens were immersed in a coolant. No essential difference was obtained for single-crystal and polycrystalline specimens with respect to their temperature dependence of the yield point. Care was taken that only single phase material was used. The single phase 49·9 at. % Zn was obtained below 300°c by heating to 750°c, water quenching, and then heating to 300°c for five hours.

Fig. 5

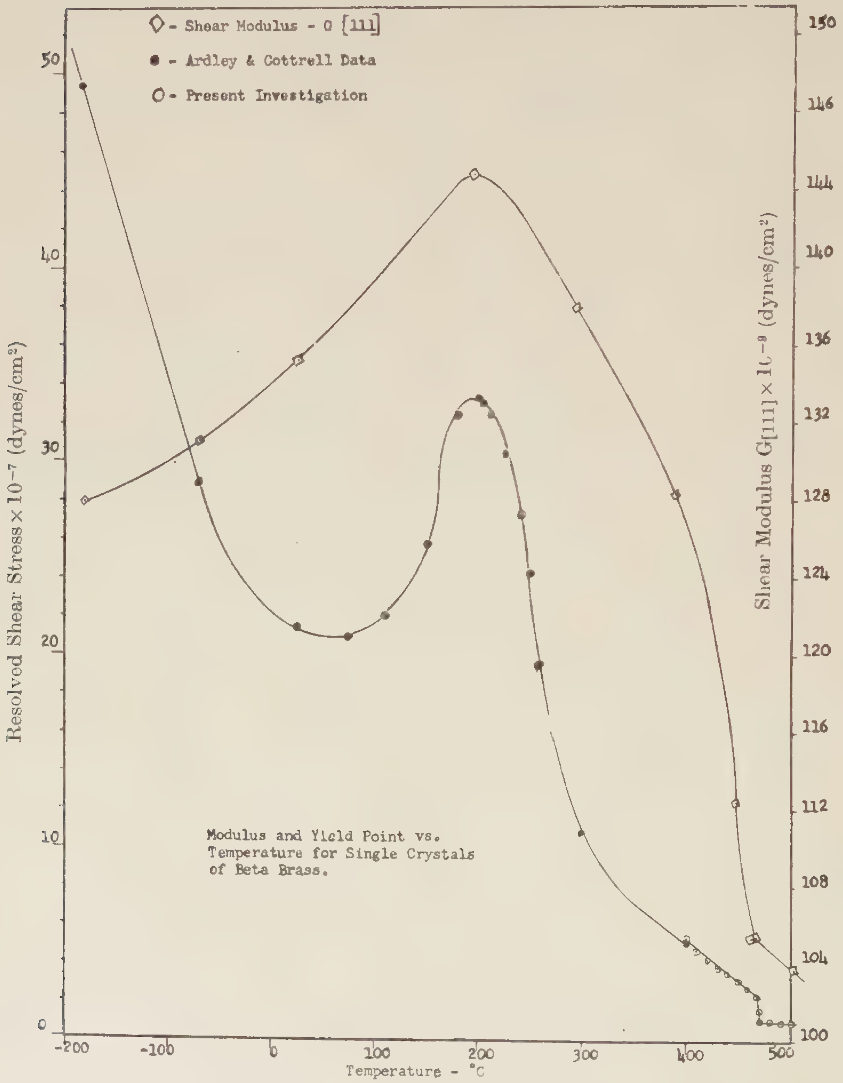

Experimental curves of yield point and shear modulus of β-brass (48·6% Zn) single crystals versus temperature.

The yield point as a function of temperature is shown in fig. 5 for the 48·6 at. % Zn. Data by Ardley and Cottrell (1953) for β-brass of about the same composition are included. The variation of yield point with temperature may be divided into four regions. Region I is above T_c and represents the behaviour of disordered β-brass : Region II (fig. 6) in the immediate vicinity of T_c is probably related to the Sumino theory because Sumino predicted exactly the same kind of jump in yield point at T_c : Region III between T_c and the minimum is associated with the present theory of the super-dislocation : Region IV below the minimum is connected with the phase transformation found by Massalski and Barrett (1957).

Fig. 6

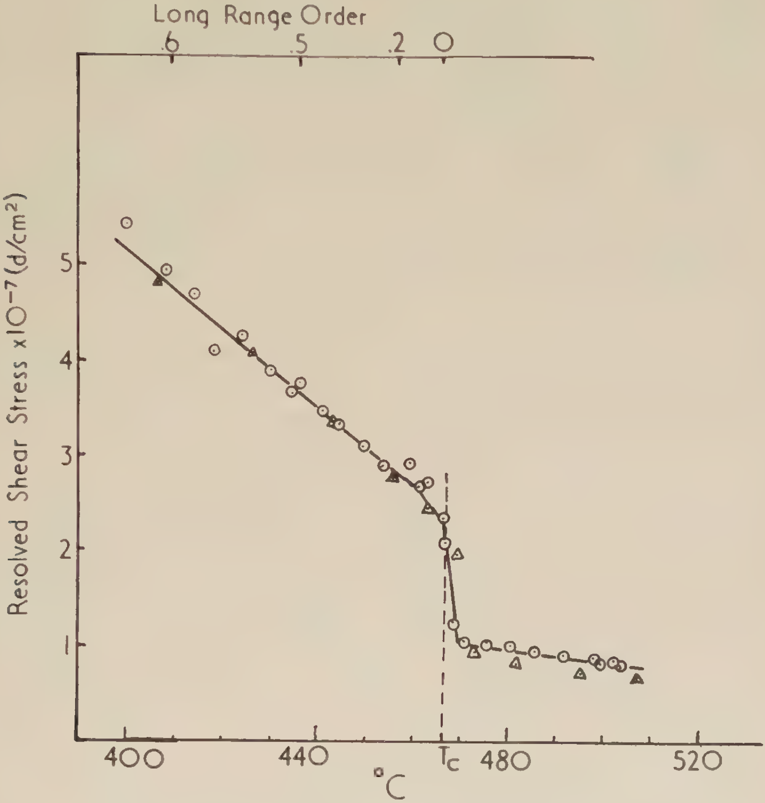

Shows short range order effect above T_c.

Regions I and II are shown more clearly in fig. 6. It is important to note that τ rises rapidly just before the temperature reaches T_c; this rise is attributed to short-range order effect as presented by Sumino. It is this short range order that also produces the tail in the specific heat curve (Dehlinger 1939).

Ardley and Cottrell suggested that Region III was caused by the maximum in shear modulus (Good 1941) which is also plotted in fig. 5. If the shear modulus were responsible, then it means that a 6% change in G can produce a 40% change in τ. This would not be possible if G acted by means of the internal stress where τ/G should be invariant as is clearly not the case. Another possibility is to assume that G effects the Peierls–Force in which case τ might vary exponentially with G as indicated by Cottrell (1953). However, the slow change in order with temperature in the vicinity of 200°c does not indicate that G would behave anomalously in this region. It is suggested that the observed change in G is an effect of the yield point and not its cause, i.e. the change in G is a relaxation effect caused by dislocation movement. In fact, Clarebrough (1957) showed that a well-defined minimum in the internal friction existed at about 200°c. It is this relaxation in G [III] that would also account for the anomalous anisotropy observed in the elastic behaviour of β-brass (Good 1941).

If one examines the phase diagram (Beck and Smith 1952) the composition of 48·6% Zn appears to cross the two-phase boundary at about 200°c where the two-phase boundary at 200°c is obtained by extrapolation. In order to test the vital point of whether the maximum at 200°c is associated with the $\beta \to \alpha$ transformation, the 49·9 at. % Zn was tested. The composition of 49·9 at. % Zn appears to cross the two-phase boundary at 75°c; if the maximum in τ is associated with the $\beta \to \alpha$ transformation, then $\tau_{\max}$ should be shifted to a lower temperature for the higher Zn concentration. Figure 7 shows τ versus T for 49·9 at. % Zn where the maximum τ is shifted to a higher temperature, 220°c, which is very close to the theoretical value of 242°c (fig. 4). In addition, the temperature of the minimum is shifted to a lower temperature, 50°c, as predicted by Massalski and Barrett, i.e. an increase in Zn content decreases the transformation temperature.

For 48·6 and 49·9 at. % Zn the maximum yield point is 0·33 and $0{\cdot}36\dagger \times 10^9$ dynes/cm^2 respectively as compared to the theoretical value of $0{\cdot}54 \times 10^9$ dynes/cm^2. Since β-brass orders very rapidly, it is thought that diffusion effects and thermal activation are jointly responsible for the yield point being less than theoretical.

Ardley (1955) has measured the yield point in $AuCu_3$ and found a maximum just below T_c. This maximum seems to fit the Sumino theory better than the present theory. However, the maximum predicted from the present theory should occur at a higher temperature for $AuCu_3$ than for CuZn because $AuCu_3$ is more ordered close to T_c. Additional data showing a maximum in yield point versus temperature was obtained by

---

† The experimental value was reduced by one-half because the specimen was polycrystalline.

Marcinkowski (1958) for Ni_3Mn. It is concluded that if yield point is measured as a function of the equilibrium degree of long-range order, a maximum will be observed. No data are known to exist that contradict the above conclusion for the cases where no change in crystal structure occurs during the long-range order transformation.

Fig. 7

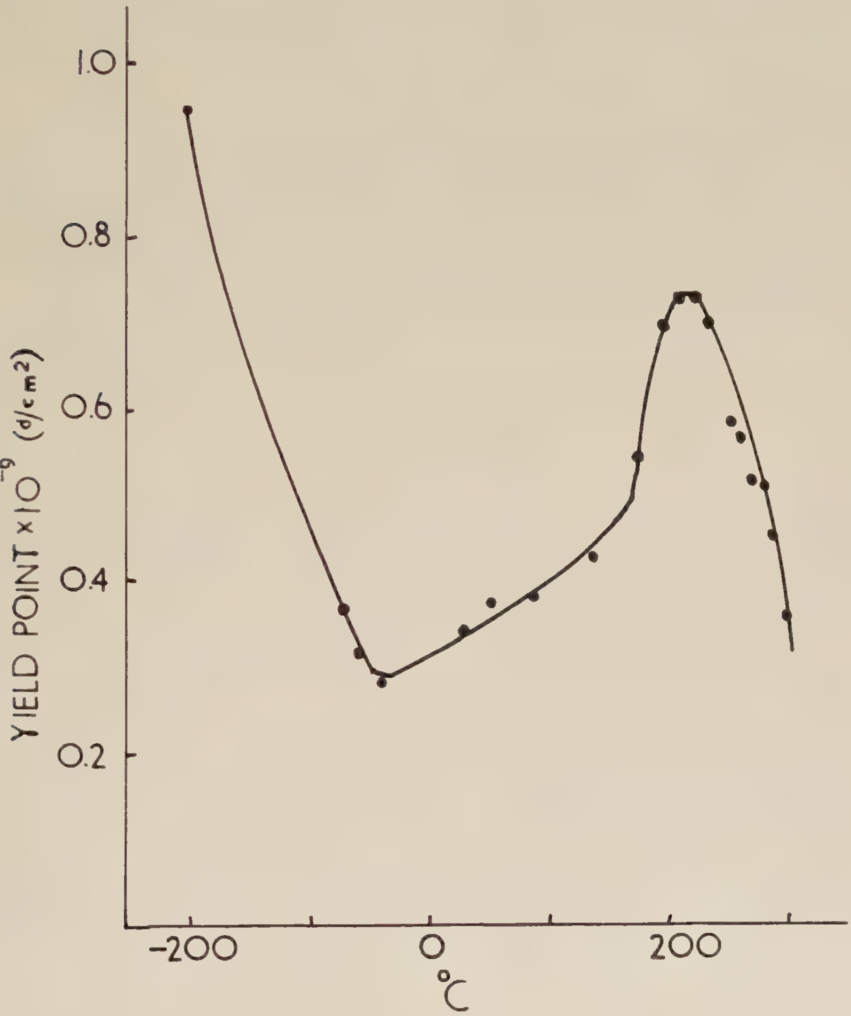

Yield point versus temperature of polycrystalline β-brass (49·9% Zn).

§ 6. Conclusions

The width of an anti-phase boundary was calculated. The stress to move a super-dislocation in the AB b.c.c. super-lattice was found to be

$$NkTS_0^2/4b$$

where S_0 is the degree of long-range order and T is the temperature. For β-brass a maximum at $T=515$°K is predicted and the maximum is observed at 493°K. The theoretical and experimental values of $\tau_{\max}$ are 0·54 and $0{\cdot}36\times10^9$ dynes/cm^2 respectively.

A very sharp increase in yield point was observed at T_c which agrees with the theory by Sumino.

There is a minimum in yield point which shifted from 50 to 75°C when the composition was charged from 49·9 to 48·6 at. % Zn in accordance with the b.c.c. to close-packed phase transformation observed by Massalski and Barrett.

ACKNOWLEDGMENTS

The data on the 48·6 Zn alloy were obtained by C. McMahon as part of his B.S. thesis at the University of Pennsylvania in 1955. R. Eckvall assisted in the experimental work. M. Herman not only prepared the alloys, but he also took part in many discussions of the problem. Dr. M. H. Cohen made many suggestions on the theory; his interest stimulated the achievement of the final solution.

Part of the work was supported by the office of Ordnance Research. The assistance of the Guggenheim Foundation is gratefully acknowledged.

REFERENCES

ARDLEY, G. W., 1955, *Acta Met.*, **3,** 525.
ARDLEY, G. W., and COTTRELL, A. H., 1953, *Proc. roy. Soc.*, **219,** 328.
BECK, L. H., and SMITH, C. S., 1952, *Trans. Amer. Inst. met. Engrs*, **194,** 1079.
BROWN, N., and HERMAN, M., 1956, *Trans. Amer. Inst. met. Engrs*, **206,** 1353.
CHIPMAN, D., and WARREN, B. E., 1950, *J. appl. Phys.*, **21,** 696.
CLAREBROUGH, L. M., 1957, *Acta Met.*, **5,** 413.
COTTRELL, A. H., 1953, *Dislocations and Plastic Flow in Crystals* (Oxford: University Press), p. 64; 1954, *Relation of Properties to Microstructure*, ASM Monograph.
DEHLINGER, U., 1939, *Chemische Physik der Metalle u. Legierungen.*
FISHER, J. C., 1954, *Acta Met.*, **2,** 9.
GOOD, W. A., 1941, *Phys. Rev.*, **60,** 605.
KOEHLER, J. S., and SEITZ, F., 1947, *J. appl. Mech.*, **14,** A–217.
KITTEL, C., 1956, *Introduction to Solid State Physics* (New York: Wiley and Son), p. 343.
MARCINKOWSKI, M. J., 1958, *Ph.D. Thesis*, University of Penna.
MASSALSKI, T. B., and BARRETT, C. S., 1957, *Trans. Amer. Inst. met. Engrs*, **209,** 455.
SUMINO, K., 1958, *Sci. Rep. R.I.T.U.*, A–10, No. 4.

The Propagation of Sound in a Binary Liquid Mixture†

By A. E. Brown and E. G. Richardson
King's College, Newcastle upon Tyne

[Received October 10, 1958 ; and in revised form January 17, 1959]

Abstract

Measurements are made in mixtures of aniline and cyclohexane at various concentrations and temperatures in the vicinity of the solution point of the velocity and attenuation of ultrasonic pulses. It appears that the large values of the attenuation observed in this region are due to the scattering of the radiation, which has been measured as to its angular distribution at various frequencies.

Evidence from the extinction and directionality of sound signals in the mixture shows that the scattering is due to biphasal clusters which exist in the neighbourhood of the solution point and which are not set up by the passage of the sound itself. There remains some absorption which is of a molecular (viscous) nature.

§ 1. Introduction

Measurements of the velocity and attenuation of sound in mixtures of liquids have been made fairly frequently since sources of ultrasonics became available and have shown in many cases a maximum or minimum in both factors at a certain concentration. This is so in liquid mixtures which form a complete solution. Our interest has been in those mixtures which in a certain range of concentration and temperature persist in two phases, whereas in another range they form a homogeneous solution. At certain concentrations the interface vanishes in a way similar to the disappearance of the liquid phase at the liquid–vapour critical point. By analogy, this phenomenon is known as 'critical solution' and the temperature as the 'critical solution temperature'.

Interesting sound transmission phenomena have been noted in the neighbourhood of the critical state of vapours. It has been the purpose of this work to extend the study of these effects. Thermodynamically, the critical solution point of a pair of liquids is similar to the liquid–vapour critical point and provides an admirable opportunity of studying the one-to-two phase transition. In many cases the critical conditions occur at atmospheric pressure and a temperature near that of the laboratory.

The present investigation has as its principal object a study (not heretofore attempted) of the *mechanism* of the ultrasonic attenuation in the critical region. One important question is, are the factors which produce the attenuation inherent in the mixture or are they set up by the passage of the radiation? Most of the previous investigators have made the latter assumption.

---

† Communicated by the Authors.

There has been a tendency in this field to make a few measurements on a number of different mixtures rather than to study one in detail, as we decided to do.

The absorption of sound in binary mixtures, is of course, closely related to the viscosity of the mixture. If there is no change of volume on mixing, the viscosity away from the critical state is linear with concentration, but if, as is often the case, there is a contraction, the viscosity shows a maximum at an intermediate concentration. This is so in alcohol–water solutions studied by Sette (1955). If, however, the concentration is kept constant while the temperature is varied and the liquids can pass from the double-phase to the single-phase type at a certain temperature, then the attenuation of sound rises to a value many times that which would be anticipated from the viscosity, as Chynoweth and Schneider (1951), also Alfrey and Schneider (1953), have shown in aniline–hexane and triethylamine–water mixtures. Cevolani and Petralia (1952) found similar behaviour in aniline–hexane and phenol–water mixtures. When solution takes place, the velocity of sound has a value intermediate between that proper to the individual liquids. The experiments are usually carried out at ultrasonic frequencies from 1 to 30 Mc/s.

In all these papers the data on attenuation and velocity were recorded but no experiments were carried out on the mechanism of the transition in relation to the ultrasonic propagation.

§ 2. The Present Experiments

In the choice of a system for the study of critical solution, the following considerations were borne in mind:

(*a*) The solution temperature must be neither too near nor too remote from room temperature.

(*b*) The liquids must be obtainable in a good state of purity.

(*c*) To minimize evaporation, the critical solution temperature must be well away from the boiling point of either liquid.

The system aniline–cyclohexane seemed to fulfil these conditions best. The critical solution temperature is near 30°c, minimizing problems of thermal insulation and stability. The substances could be obtained pure in reasonable quantity. Cyclohexane boils at 83°c and aniline at 184°c, well above the critical solution temperature.

Measurements of velocity and attenuation were made, using a pulse technique, at 1·5, 2·5 and 5 Mc/s. The composition of the mixture was varied and observations made for several degrees on either side of the critical solution point.

Following techniques which have been used for a number of years in this laboratory, a double transducer system of quartz—one to emit and one to receive—was employed.

Pulses of 40 microseconds duration were derived from a gated oscillator. These were applied to the transmitting crystal which was carried on a movable piston. The electrical signal from the receiver, having an amplitude proportional to that of the incident sound, was, after amplification and detection, displayed on a cathode-ray oscillograph. As the crystal separation was reduced, the amplitude of the display was kept constant by the operation of a calibrated attenuator in the receiving circuit, its reading corresponding to the attenuation of the decreased path.

A graph of the movement against attenuator reading gives the attenuation coefficient α' in decibels per centimetre directly from the slope; α' is related to the amplitude attenuation coefficient α by the relation

$$\alpha' = 20\alpha \log_{10} e \quad \text{or} \quad \alpha' = 8{\cdot}686\alpha.$$

Measurements of the velocity of propagation of the pulse, required in the calculations of scattering, *vide infra*, were made by mixing the signal at the receiving transducer with a comparable fraction of the (electrical) pulse applied to the sender. The magnitude of the resultant measures the relative phase of the components, which varies rhythmically with the separation of the transducers and so can be used to calculate the velocity. These experiments were made entirely in the Fresnel region of the radiation, i.e. for a separation of transducers less than R^2/λ where R is the radius of the quartz face ($\frac{1}{2}$ in.) and λ the wavelength in the liquid.

The vessel containing the liquids is a vertical glass tube 2 in. diameter and 6 in. long. The lower quartz is pressed from outside against a thin aluminium disc, forming the base of the vessel; the upper is mobile and has the usual adjustments for setting it parallel to the other. The whole is then placed in a container $4\frac{1}{2}$ in. diameter and 8 in. long with heater coils and thermostat control. The latter is designed to hold the temperature—read by thermocouple in the liquid—constant to 0·01°C over a period of 5 min.

§ 3. PREPARATION OF LIQUIDS AND TESTS

Benzene was used as test liquid. Adjustments of the mechanical part of the apparatus were made until a value for the attenuation in this liquid was obtained in agreement with the most precise of published results.

Liquids of 'Analar' grade were used for the mixtures. As samples obtained on different dates from the suppliers gave consistent results, it was concluded that the purity of the liquids was sufficient to give reliable results.

Each mixture was made up by volume, shaken in a bottle, then introduced into the apparatus, stirred to remove the bubbles, and the thermostat set in operation. A graph of micrometer screw reading against attenuator setting was plotted and the attenuation in decibels per centimetre calculated. Any graphs showing appreciable departure from linearity were discarded.

The thermostat was set to allow a slight fall of temperature during the day. As the critical solution temperature was approached, the fall was slowed down by the emission of the latent heat of solution—a convenient effect since more measurements could be made in this important region. Measurements were made only at falling temperature. If the stratified liquids were left undisturbed, mixing did not take place until the temperature had risen a degree or more above the temperature at which separation took place, doubtless an influence of the size of the experimental vessel. Vigorous stirring was found to promote mixing, but often carried air bubbles under the edge of the upper crystal holder. It was therefore assumed that the temperature of separation obtained in a run at falling temperature was the true critical solution temperature and effects of hysteresis were not investigated.

The experimental points obtained by a run of the above type usually fell on a smooth curve, indicating some degree of reliability. Intermediate points could be filled in on subsequent runs with quite good accuracy. It was estimated that the overall accuracy at higher attenuations (~ 2 dB/cm) was 2%, at lower attenuations ($> 0{\cdot}3$ dB/cm) 5%, the main uncertainty being the setting-up of the signal on the graticule of the oscilloscope.

The concentrations studied ranged from 20 to 60% mols of aniline and the temperatures from 29° to 34°C by half degrees.

Fig. 1

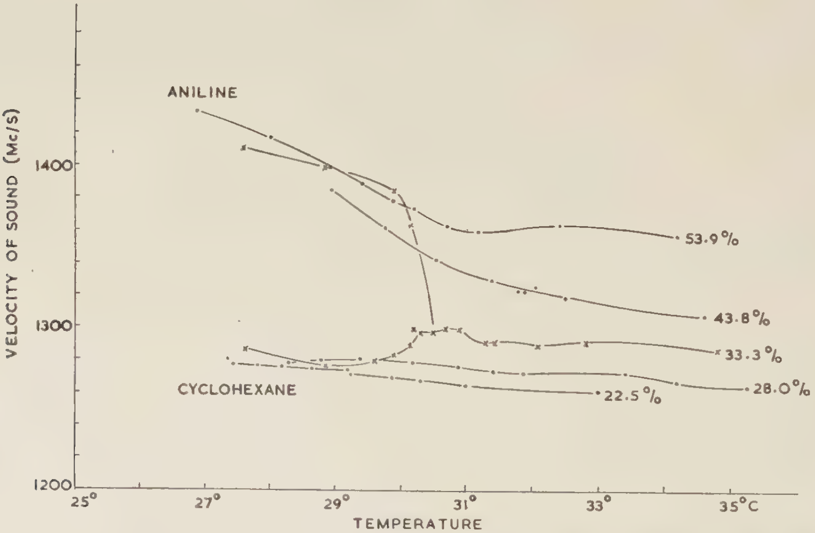

Velocity of sound in mixtures of various molar percentages of aniline in cyclohexane at 5 Mc/s.

§ 4. Velocity Results

Measurements of velocity as a function of temperature for a range of concentration were made at 1·5, 2·5 and 5 Mc/s. Figure 1 shows the results at the highest frequency, with the critical temperature indicated as 30·7 °c for a concentration of 33·3%. Below this temperature the mixture breaks into two layers, so that different results are obtained for the ultrasonic wavelength according as the interferometer path lies entirely above or below the interface.

Although the curves for the three frequencies did not exactly fall together, especially near the solution point, a fact which we ascribe to different mixing conditions for successive solutions, we have no definite indication of dispersion of velocity in this range of frequency.

Fig. 2

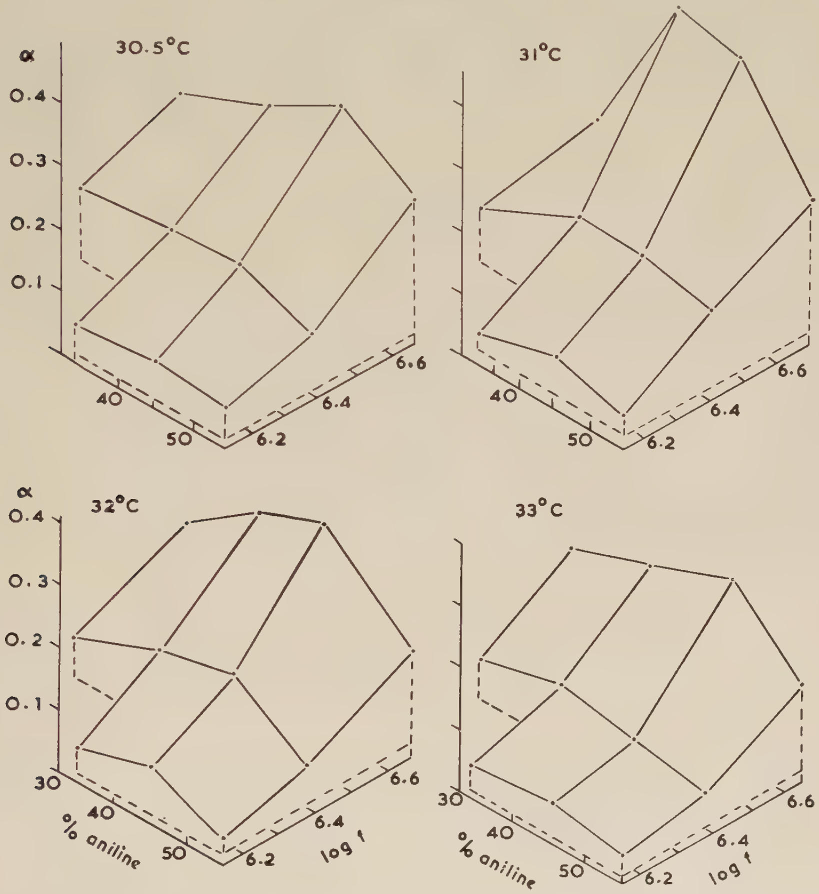

Total attenuation in mixtures at various frequencies.

§ 5. ATTENUATION RESULTS

While the ‘ triple point ’ in the velocity always occurred at the solution temperature, the maximum of attenuation often occurred a little higher (up to $1\frac{1}{2}$ °c higher). After analysis of many observations at four temperatures in this region, they were re-plotted as shown in fig. 2. They exhibit the rise of attenuation with frequency, when the mixture has a concentration near 40%. (The pure liquids have values for the coefficient α ranging from 0·001 to 0·04 as the frequency rises in this range.)

The previous workers in this field all ascribe this large absorption to relaxation processes, mostly structural in nature, as though much of the energy in the sound beam were dissipated in forming and breaking up 'clusters'; indeed, some speak of 'cluster relaxation'. Be this as it may, we have adopted the viewpoint that the clusters may be already present in the critical state—as they certainly are in carbon dioxide near its critical point, cf. Andrews' well-known experiments—and may scatter the radiation out of the forthright beam, just as they scatter light in this region in the phenomenon of 'critical opalescence'.

Scattering will occur wherever fluctuations in acoustical refractive index occur, having their origin in density variations or circulatory motions in the fluid. The former type is to be found in suspensions of solids or liquid globules in a matrix liquid (Allinson and Richardson (1958)); the latter in an atmosphere filled with eddies (Richardson (1950)). The scattering of sound from a rigid sphere, small compared to the wavelength λ, was first calculated by Rayleigh and led him to the well-known law, which applies equally in optics. When the obstacle is large, the scattered energy is concentrated in a direction down the beam (behind the scatterer). At intermediate sizes ($2\pi a \approx \lambda$) the diffraction phenomena familiar in optics under the name of Mie make their appearance and withal the total energy scattered goes through sinuous variations (as λ decreases) until it establishes itself at a value twice that intercepted by the scattering obstacle. Although the form of this curve is the same for all acoustic properties of the scattering material, the amplitude of these variations in the total scattered energy depends on the refractive index, to sound, of the material and on its density relative to the ambient medium.

§ 6. SCATTERING MEASUREMENTS

In order to examine these aspects of the problem it seemed to us desirable to modify the apparatus so that the proportion of sound energy diffused out of the main beam could be measured.

An ultrasonic beam is transmitted across a vessel containing the mixture. A receiving transducer or probe is mounted so as to allow it to be moved in a circle through whose plane the axis of the beam passes. Pulsing of the sound transmitter allows spurious echoes from the walls and the free surface to be distinguished by their associated time delay. The amplitude of the signal at any angle is read directly from its height on the oscilloscope display.

A cross-section of the mechanical apparatus is given in fig. 3. The experimental vessel is of sheet steel, 6 in. deep and about 3 in. square in section. It is arranged to fit neatly into the thermostat cylinder whilst being suspended from a wooden base-board carrying the usual thermal insulation. A hole in the side of the vessel is covered with an aluminium diaphragm. Against the back of this the transmitting crystal is pressed by means of a leaf spring acting as the r.f. connection.

The receiving probe is also a quartz crystal carried in a brass holder having an aperture of 1 cm. This size is chosen as a matter of compromise. In this work it is necessary that the angle at which the energy is scattered be known with precision. For a given wavelength, the receiver becomes more directional the larger its diameter, making a large-aperture receiver desirable. On the other hand, if the beam of scattered sound is of less width than the receiver, the latter will give an erroneous value of the scattered amplitude. The chosen diameter (1 cm) gives an angular half-width of 1·4° of the central maximum of its diffraction pattern at 5 Mc/s. This diameter is less than half that of the transmitted beam and—it is assumed—of the scattered beams. The size of the chamber in these experiments is limited by the necessity to keep a close control on the temperature and by the high attenuation in the vicinity of the critical solution.

Fig. 3

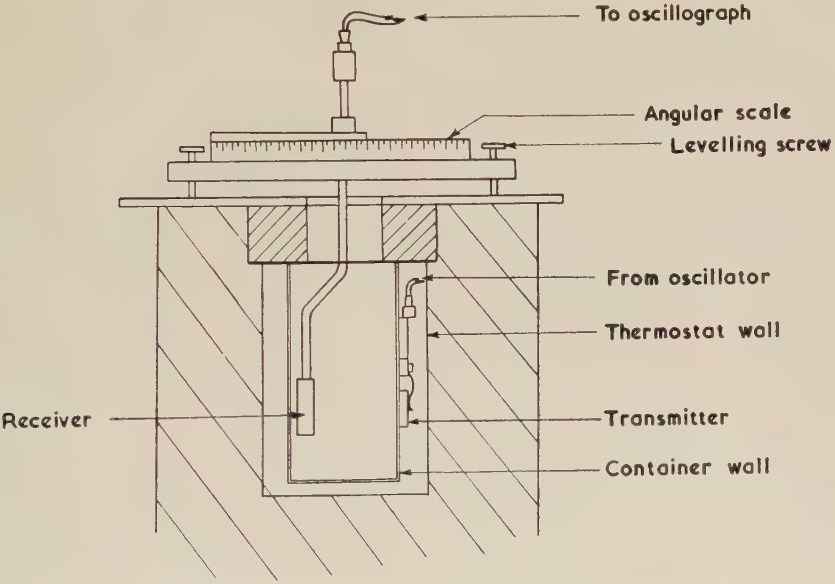

Device for detecting scattered radiation.

Consider a single scattering obstacle in a plane sound beam. Let the intensity of scattered sound at angle θ to the beam (as measured by a probe) be $I_{(\theta)}$. Assuming the intensity of scattered sound is symmetrical about the beam axis, the scattered energy dE at angle θ is given by $dE = I_{(\theta)} d\Omega$ where $d\Omega$ is the element of solid angle between θ and $\theta + d\theta$. The total energy

$$E_1 = 2\pi I_0 \int_0^{\pi} f(\theta) \sin\theta \, d\theta,$$

I_0 being the central maximum and $f(\theta)$ the distribution with angle.

Now let the experiment be repeated in a pure liquid having the same velocity of sound so that the pattern due to diffraction alone will be unchanged. The total energy

$$E_2 = 2\pi I_1 \int_0^\pi f'(\theta) \sin\theta \, d\theta,$$

I_1 being the intensity in the central maximum.

Both the central and azimuthal beams are subject to molecular dissipation which may not be the same for the mixture and the comparison liquid but does not affect the polar curve in the first order. (The effect of attenuation on the theory of diffraction has been studied by Alblas (1957).) If therefore the central maximum is adjusted to the same value in each case, the energy scattered between the crystal and a plane of scansion at a distance x can be expressed by a coefficient

$$\alpha_s = \frac{1}{2x} \log_e \frac{P_x}{Q_x}$$

where P_x and Q_x are the values of the integrals

$$\int f(\theta) \sin\theta \, d\theta \text{ and } \int f'(\theta) \sin\theta \, d\theta$$

at the distance x. There is of course an implicit assumption that the pure liquid does not scatter. This might be tested by plotting the sound field round the transducer in a gas like argon for which the absorption is given by the classical formula of Kirchhoff and adjusting the pattern for the difference in sound velocity. There is also the ever-present difficulty that the scattering is multiple whereas the theory assumes single scattering. (Multiple scattering has been studied by Fejer (1953) but his theoretical results for $a \leqslant \lambda$ are not applicable to this case.)

If the transmitter behaved as a piston source it might be thought that interference between the contributions at the receiver from all the scatterers within the volume which the probe 'views' would occur, but in practice the width of the probe seems to obliterate such interference, except at the highest frequency. The scattered distribution could therefore be mapped out directly without undue labour. In the 5 Mc/s case the pattern consisted of many peaks whose precise delineation would have been laborious and unnecessary. The following procedure was therefore adopted. The amplitude at the top of each peak was noted. A plot of these readings against angle was similar in form to one in which the peaks and valleys were smoothed out—i.e. in which interference was allowed for—except that compared to other curves the vertical scale was doubled. The value of E evaluated from a graph of $I_{(\theta)} \sin\theta$ by mechanical integration was therefore divided by 4. This procedure however obliterated the central peak but a value obtained from the experiments on non-scattering liquids could be inserted to compensate for this, if required.

§ 7. Scattering Results

The angular distributions of sound were obtained and the scattering attenuation estimated at frequencies of 5, 2·5 and 1·5 Mc/s in mixtures containing 22·5, 33·3, 43·8 and 53·9 molar per cent of aniline. The measurements at 5 Mc/s occasioned little difficulty apart from the complicated nature of the distribution pattern, presumably due to interference. At 2·5 Mc/s the distribution took on more the aspect of a broadened central beam, the angular spread not being more than 4° or 5°. At 1·5 Mc/s this spread was greatest, although it was still possible to distinguish between scattering and non-scattering liquids with certainty.

Fig. 4

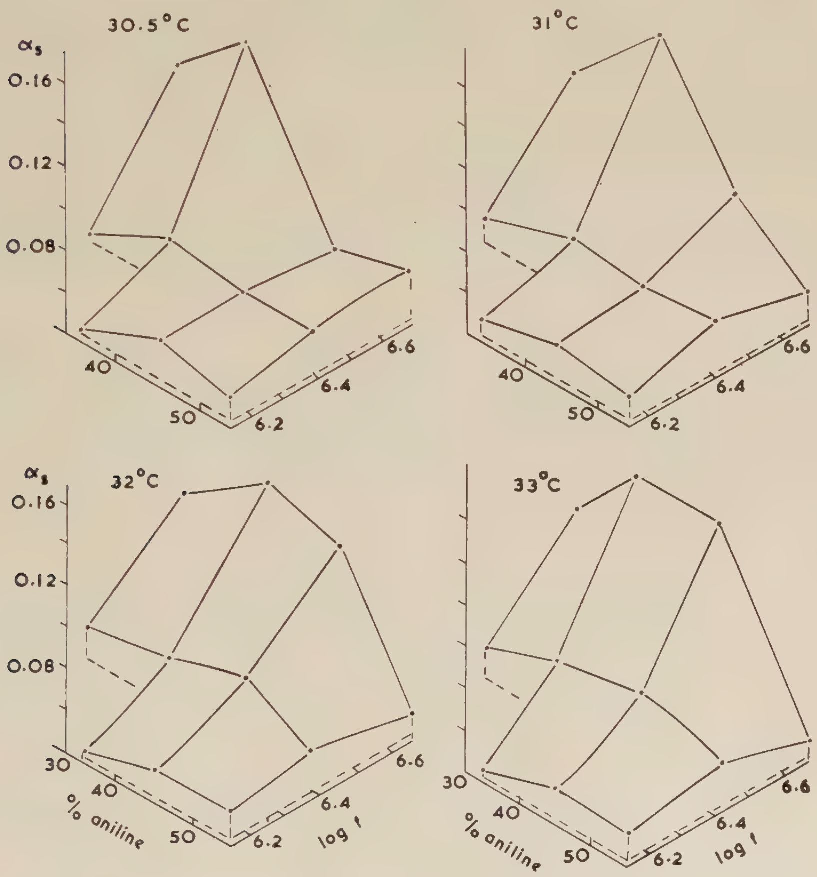

Scattered attenuation at various frequencies.

The overall scattering measurements are presented in a three-dimensional plot (fig. 4) of the same type as that in fig. 2.

At 22·5% aniline concentration the scattering attenuation almost keeps pace with the total sound loss throughout the critical region. At

Table 1

Temperature °C	$f=1{\cdot}5$ Mc/s			$f=2{\cdot}5$ Mc/s			$f=5{\cdot}0$ Mc/s		
	α	α_s	c	α	α_s	c	α	α_s	c
22·5% aniline									
34				0·057	0·011	1262	0·145	0·11	1260
33				0·070	0·030	1262	0·15	0·11	1260
32				0·080	0·035	1262	0·15	0·11	1262
31				0·097	0·023	1262	0·155	0·11	1264
30·5				0·115	0·023	1262	0·17	0·12	1266
30				0·140	0·011	1262	0·185	0·14	1268
29·25				0·105	0·06	1262	0·26	0·145	1270
33·3% aniline									
34	0·042	0·006	1281	0·09	0·055	1282	0·23	0·20	1288
33	0·045	0·007	1284	0·105	0·055	1282	0·23	0·20	1291
32	0·057	0·011	1288	0·130	0·055	1289	0·25	0·17	1288
31	0·060	0·02	1294	0·160	0·055	1289	0·40	0·17	1294
30·5	0·057	0·007	1296	0·132	0·055	1296	0·25	0·20	1297
43·8% aniline									
34	0·050	0·035	1312	0·080	0·063	1318	0·24	0·17	1310
33	0·057	0·035	1317	0·086	0·063	1319	0·27	0·20	1316
32	0·092	0·035	1323	0·130	0·070	1322	0·30	0·15	1322
31	0·083	0·04	1323	0·160	0·046	1319	0·38	0·05	1333
30·5	0·077	0·052	1323	0·140	0·046	1318	0·32	0·03	1342
53·9% aniline									
34	0·040	0·035	1355	0·070	0·052	1360	0·14	0·023	1356
33	0·040	0·035	1355	0·075	0·046	1360	0·16	0·023	1361
32	0·040	0·035	1356	0·087	0·043	1361	0·18	0·023	1360
31	0·055	0·030	1359	0·14	0·058	1371	0·23	0·035	1359
30·5	0·054	0·030	1360	0·115	0·050	1375	0·23	0·029	1365
30	0·080	0·023	1360	0·092	0·058	1379	0·26	0·035	1376

33·3% however there is a falling-off in scattering at a slightly higher temperature than the attenuation peak, the scattering attenuation not recovering its former value until around the solution point. With the 43·8% mixture, the behaviour is most striking. The scattering attenuation, having kept pace with the total loss, falls sharply some 2°c above the solution temperature reaching a very low minimum at a temperature almost identical with that of maximum total attenuation. There are signs of an increase in scattering at temperatures below the solution temperature, but it is difficult to decide in which of the two liquid layers the measurements have been taken and such results may be misleading. The 53·9% mixture displays little scattering, but a peak is noted near the temperature of maximum attenuation together with an increase through the solution temperature. One of the matters of note about the curves is the way in which the scattering and total attenuation keep pace at the

Fig. 5

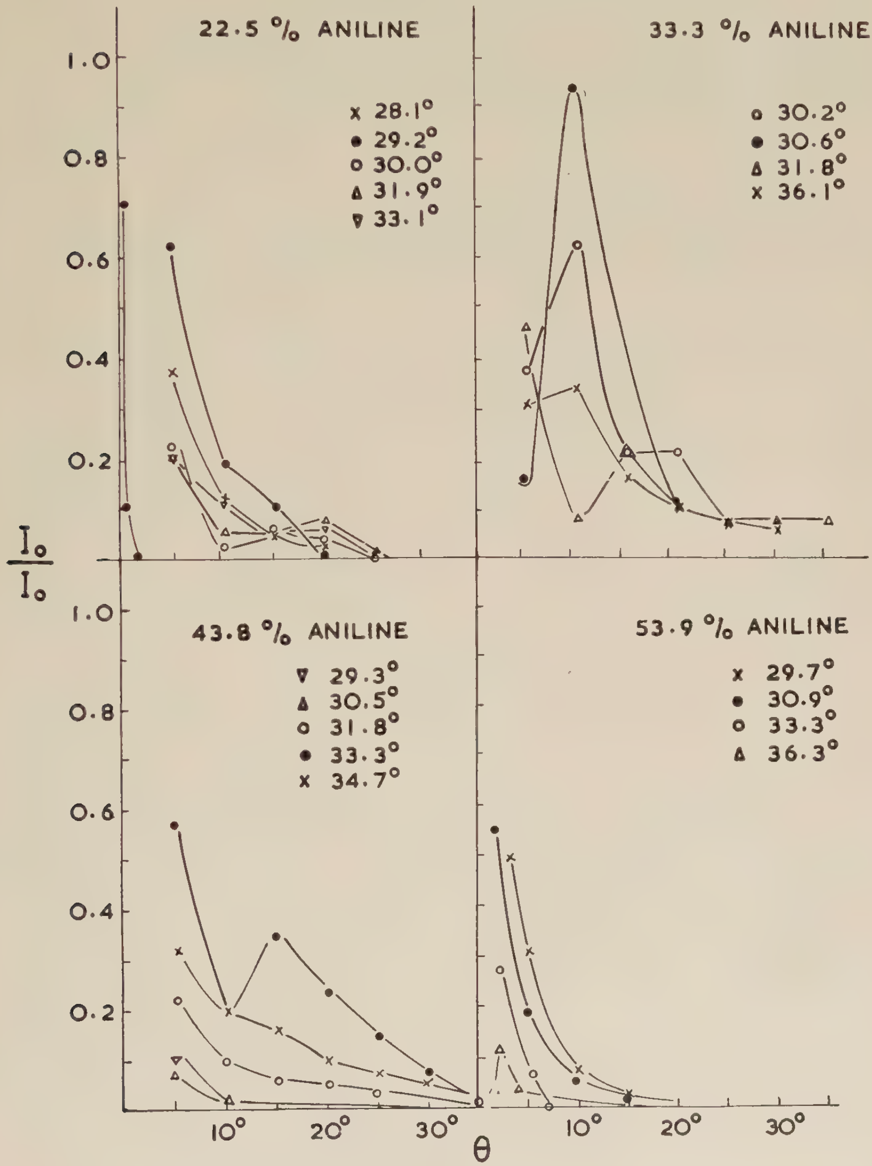

Angular distribution of scattered sound at 5 Mc/s.

high temperature end of the range. When the scattering coefficient is subtracted from the total coefficient in this region the remainder is of the order of that found in the separate liquids, viz. aniline $\alpha/f^2=50$, cyclohexane $\alpha/f^2=200$, $\times 10^{-17}$.

The individual results are shown, as total attenuation and total scattering in table 1. Although both reach a maximum near the solution temperature, the two peaks do not always fall together.

There are several methods of analysing the scattering curves of a monodisperse suspension of spheres to derive the particle size in terms of the wavelength, the relevant parameter being $\gamma=2\pi a/\lambda$:

(1) From the variation of scattered intensity with angle using tables such as those compiled by Lowan (1946).

(2) From the variation of extinction in the direct beam, supposed to be deprived of energy by scattering, with wavelength or frequency.

Curves of the relative intensity of sound at various angles from the beam axis for certain temperatures and compositions are given in fig. 5. The relative intensities plotted are the average values for the required angle on both sides of the central maximum. In a medium without scattering the diffraction pattern of the probe falls to zero (first minimum) at an angle of 1·5° at 5 Mc/s. Viewing our curves in the light of this fact demonstrates beyond any reasonable doubt the existence of the scattering phenomenon.

Maxima and minima in the polar curves are noted, particularly when the mixture contains one third of aniline (molar), indicating some degree of uniformity of size of the clusters. From the position of these maxima and minima and from the polar curves in general, it should be possible to deduce the mean cluster size, if the refractive index m is known. The velocities of sound in the pure liquids are 1250 and 1660 m/s respectively giving $m=1{\cdot}33$—as for rain drops in air to light waves. The calculation of the angular distribution can be made from the Rayleigh–Gans theory if the refractive index is sufficiently near to unity for the scattered field to be solely due to the phase difference between the wave which has passed through the 'sound-soft' sphere and that through the external medium when they reach the rear of the obstacle. Otherwise the calculation of the field is difficult but Hart and Montroll (1951) have been able to extend the Rayleigh–Gans calculations to refractive indices in the range $m^2-1<\gamma-1$ which would cover all the cases encountered in these mixtures. In what follows it appears that this cluster size is comparable with or, in some cases, greater than the wavelength. When γ is considerably greater than unity the distribution with angle takes the form

$$I_\theta \propto 1+\cot^2\theta/2J_1^2(\gamma\sin\theta)$$

but in the awkward region where $\gamma=1$, the tables constructed by Lowan for the corresponding light case must be used.

Pursuing this course for some trial values of γ we find, for instance, that for $\gamma=3$, the first maximum should occur at about 15°, which corresponds to the distribution at 30·2°C in the mixture of one-third aniline, while the steeper fall in 53·9% aniline at a nearby temperature would indicate $\gamma=5$, with a much smaller value at 36°C.

Fig. 6

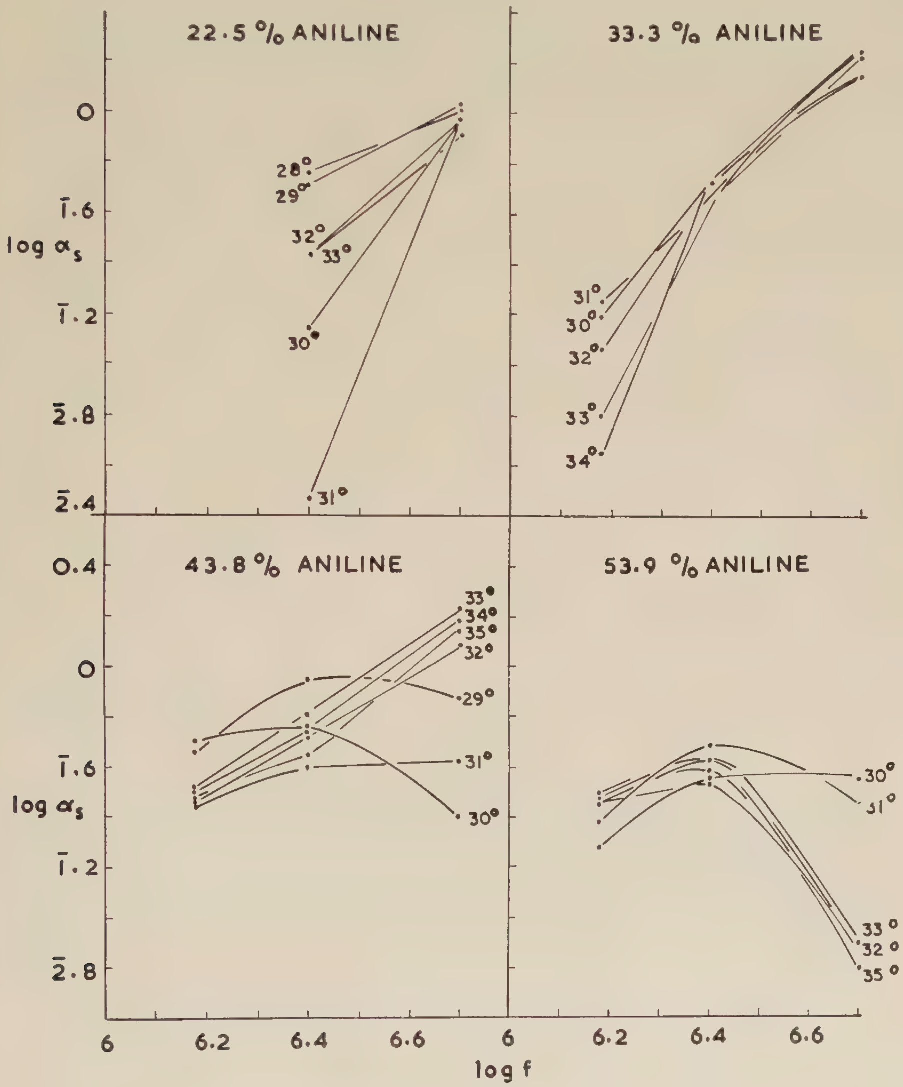

Frequency dependence of scattered sound.

A log–log plot of scattering attenuation against frequency for various temperatures and concentrations is given in fig. 6. For the curves away from the absorption region the slope is round about 2, indicating a scattering proportional inversely to the square of the wavelength.

In the case of the 53·9% concentration, the power changes in sign at a higher frequency, while in the 33·3% case it increases with decreasing frequency, approaching the value 4 appropriate to scattering by obstructions much smaller in size than the wavelength. Such behaviour of the extinction coefficient—fraction cut-off the direct beam—recalls the maxima and minima of transmission as λ is varied and whose position is again a function of γ. It is usual to express the transmission in terms of a scattering cross-section (per unit area) A as it varies with $\gamma(=2\pi af/c$, with c the velocity of sound, in this case). A graph of this parameter for a refractive index $m=1{\cdot}33$ has been calculated by Hart and Montroll (1951) and is shown in fig. 7 for comparison with fig. 6.

Fig. 7

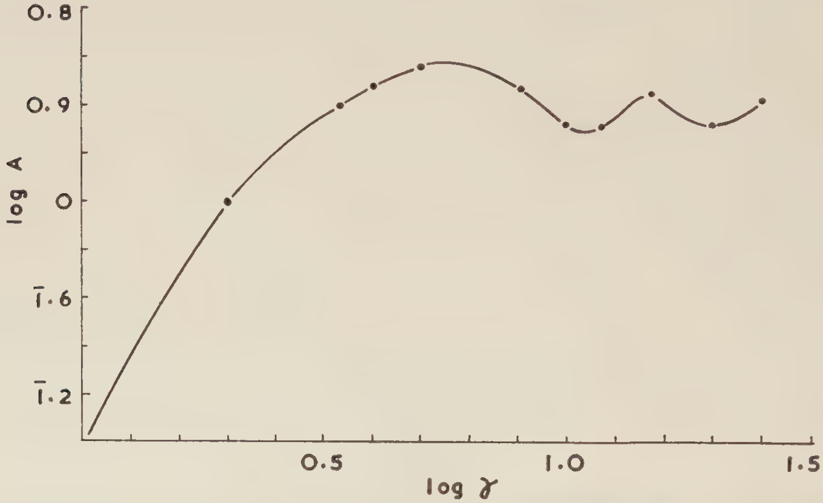

Variation of extinction due to scattering with parameter $2\pi a/\lambda$ for refractive index, 1·33.

We have made the comparison by choosing for each temperature a value of γ to which each of the four sets of curves in fig. 6 of α_s against f can be best matched in slope and turnover. Knowing the frequency and velocity of sound we then calculate from this value of γ the 'cluster radius' a.

Here are some typical results at 2·5 Mc/s and 31°c.

Table 2

Mol % aniline	γ estimated	λ (mm)	a (microns)
22·5	1·5	0·50	120
33·3	2	0·51	150
43·8	3	0·53	250
53·9	5	0·54	400

It may well be that the value we have assumed for m is too high. There is no reason to suppose that the globules should be formed of pure aniline in a matrix of pure cyclohexane. A smaller refractive index would shift the first peak of the curve in fig. 7 in the direction of higher values of γ in the ratio $\lambda/(m-1)$, but in the absence of knowledge of the coefficient of mutual diffusion of the two liquids, we cannot quote a precise value for m.

§ 8. SCATTERING PROCESSES

We should hesitate to aver that, within the limits of accuracy of the scattering measurements, the whole of the reduction in intensity in the direct beam is to be ascribed to scattering. After subtracting that which can be ascribed to shear viscosity, there remains an amount, of the same magnitude as that in the pure liquids, which must be put down to relaxation or bulk viscosity.

We now revert to the question we raised earlier; do these clusters exist already in the liquids when they approach the critical solution temperature or are they caused by the passage of the ultrasonics? Ernst (1947) in his investigations on the velocity of sound—measured by optical diffraction—in another binary mixture mentions the appearance of a 'brick wall structure'. He shows a photograph of this appearance but he does not give a scale, though it appears that the cells have a diameter of the order of the ultrasonic wavelength and they seem to us to correspond to the cells of Bénard which can be set up in an unstable liquid column as small scale copies of the 'mackerel sky', a cloud formation visible under similar conditions in the atmosphere. He remarks that the formation once set up could persist for hours. We have not observed this honeycomb structure in our mixtures but then we are putting in the energy only weakly and occasionally, Ernst used *continuous* waves of sufficient intensity to diffract light at the wave front.

Though it is not possible to see clusters at the solution point with the unaided eye because the relative optical refractive index of the liquids is only 1·11, we have successfully applied the schlieren technique to this problem. The schlieren apparatus was set up for the observation of phenomena due to convection in a large tank of water. For the present purpose a small glass-walled cell about 3·4 cm square and 7 cm deep containing the mixture was set up vertically in a large tank of water (acting as a thermostat) and in the way of the light beam of a schlieren apparatus. Under the schlieren view and in the absence of any sound propagation the clusters were clearly visible moving about, though they had rather the appearance of striations than globules, at all temperatures from 30° to 33°C, and recalled the photographs made by Graham (1934) of a layer of liquid heated from below and sheared. When a photograph was taken of our striations it was possible to estimate their size e.g. at 32·5° there were 25 per cm length, at 33°C, 30 per cm (cf. fig. 8), Pl. 79.

These inhomogeneities are the evident cause of the scattering which we have encountered in the ultrasonic experiments. It is intended to continue this work on sound scattering by density inhomogeneities to the class of fluids investigated by Graham, i.e. to set up temperature gradients in a single fluid and observe the effect on an ultrasonic beam transmitted through it.

References

Alblas, J. B, 1957, *Appl. sci. Res., Hague*, A, **6,** 237.
Alfrey, C. F., and Schneider, W. G., 1953, *Trans. Faraday Soc.*, **15,** 218.
Allinson, P. A., and Richardson, E. G., 1958, *Proc. phys. Soc., Lond.*, **72,** 733.
Cevolani, M., and Petralia, S., 1952, *R.C. Accad. Naz. Lincei*, **2,** 674.
Chynoweth, A. G., and Schneider, W. G., 1951, *J. chem. Phys.*, **19,** 1566.
Ernst, P. J., 1947, *J. acoust. Soc. Amer.*, **19,** 342.
Fejer, J. A., 1953, *Proc. roy. Soc.* A, **220,** 455.
Graham, A., 1934, *Phil. Trans. roy. Soc.* A, **232,** 285.
Hart, R. W., and Montroll, E. W., 1951, *J. appl. Phys.*, **22,** 376.
Lowan, A. N., 1946, *Scattering and Radiation from Circular Cylinders and Spheres* (U.S. Navy Department).
Richardson, E. G., 1950, *Proc. roy. Soc.* A, **203,** 149.
Sette, D., 1955, *Ricerca Sci.*, **25,** 576.

An Electron Microscope Study of Stainless Steel Deformed in Fatigue and Simple Tension†

By P. B. Hirsch, P. G. Partridge and R. L. Segall
Crystallographic Laboratory, Cavendish Laboratory, Cambridge

[Received January 15, 1959]

Abstract

A technique is described whereby the surface of metal specimens can be examined by transmission electron microscopy. The original specimens are thinned by electropolishing from one side ; thus the surface contours, e.g. slip steps, are preserved on one of the surfaces. It is shown that dislocations are revealed associated with the surface slip lines ; the step heights and surface contours such as those of fatigue striations are observed at a high magnification due to a taper section effect.

§ 1. Introduction

In recent studies of the dislocation arrangements in deformed metals by the transmission electron microscopy technique (Whelan *et al.* 1957, Hirsch *et al.* 1958) bulk specimens were deformed and subsequently thinned by electrolytic polishing from both sides of the sheet. In this way the dislocation arrangement in the *interior* of the metal was revealed. It is of particular interest however to study the dislocation arrangement and other defects near the surface of the specimen. Accordingly a technique has been developed whereby the specimens are prepared by thinning from one side only, so that one original surface is retained. In this way surface markings, such as slip lines, can be seen at the same time as the dislocations and other defects just below the surface of the metal. The experiments have been performed on stainless steel with the following objects in view:

(1) To relate the slip lines to the dislocations just below the surface of the metal.

(2) To examine whether the dislocation arrangement near the surface is similar to that in the interior.

(3) To study the dislocations and other defects and to search for possible cracks at the surface of specimens deformed in fatigue, where the surface is known to be particularly important.

§ 2. Experimental Technique

Specimens of annealed stainless steel with the same composition as that used in previous investigations (Whelan *et al.* 1957, Whelan 1959) and some specimens of a similar austenitic stainless steel (18/8 type) were electropolished in a bath of 40% sulphuric acid and 60% phosphoric acid and then either deformed 10% in tension or fatigued for 10^7 cycles in reverse plane bending with zero mean stress. The thicknesses of the tensile and fatigue specimens were 0·005 in. and 0·012 in. respectively. The fatigue machine was a commercial Avery plane bending machine, this mode of deformation being chosen because it is comparatively easy to maintain zero mean stress in a thin specimen. The fatigue stress was chosen so that 10^7 cycles corresponded approximately to 10% of the life of the specimens.

---

† Communicated by the Authors.

After deformation the specimens were coated on one side with 'Lacomit', a commercial acid resistant varnish, and thin films were then prepared by electropolishing from the unprotected side towards the coated surface. When the test pieces were thought to be sufficiently thin, specimens were cut off in the usual way (Tomlinson 1958) and the varnish dissolved with 'Lacomit Remover'. The thin films were then examined in a Siemens and Halske Elmiskop I operating at 80 or 100 kv.

§ 3. Experimental Results

3.1. *Observations of Slip Lines*

The surface slip lines can be observed on the electron micrographs in two distinct ways:

(1) They appear as lines along the directions of the intersections of the slip planes with the previously protected surface, in much the same way as slip lines on surface replicas (e.g. Wilsdorf and Fourie 1956, Mader 1957).

(2) The slip lines are associated at the edge of the thin foil with steps which correspond to the slip line steps magnified by a taper section effect.

3.1.1. *Contrast effects*

Figure 1 (Pl. 80) is a micrograph of a stainless steel specimen deformed in tension showing a set of prominent slip lines crossed by a set of fainter lines corresponding to slip on another system. The transmitted intensity is the same on either side of a slip line, but the line itself shows very pronounced contrast. Sometimes the contrast of the lines is darker than the background, and sometimes lighter as for example in fig. 2 (Pl. 81), which is a micrograph from a similar specimen. Some of the lines on fig. 1 show both dark and faint white contrast. All these contrast effects are very similar to those observed on slip traces produced by movement of dislocations in thin foils (Hirsch *et al.* 1956, Whelan *et al.* 1957). By analogy with the interpretation of the slip traces, the contrast of the slip lines in the present case is considered to be due to strains in the oxide film on the specimen surface. However, whereas slip traces can be formed as the result of the movement of single dislocations, many of the slip lines in figs. 1 and 2 are due to the passage of a number of dislocations. Another important difference between slip lines and slip traces is the fact that slip lines only occur on one side of the specimen, while slip traces consist of pairs of lines corresponding to the top and bottom surfaces of the foil. This can be seen very clearly in fig. 3 (Pl. 82), where dislocations on the slip planes are associated with one line corresponding to the protected surface. Other clear examples can be seen at A in figs. 1, 2.

The question arises whether the slip lines are the result of dislocation movement during deformation, or whether they reflect a rearrangement of the dislocations in the thin foil (thinned specimen). Movement of dislocations after thinning would result in the formation of slip traces (i.e. pairs of lines). These are observed only very rarely. In some areas, for example at B in fig. 1, the dislocations (below B) appear to be associated with slip lines at both ends, as if the two slip lines constituted a slip trace. Close examination however reveals that the dislocations are associated *exactly* only with one line; thus the set of dislocations below B belong to the slip line on their left, while the set of dislocations to the right of B to the other slip line. Furthermore the asymmetry of the contrast of the slip lines in fig. 1 is always in the same sense (i.e. white line on the right of black line), whereas for the pair of lines constituting a slip trace the asymmetry would be in the opposite sense (for examples see Whelan *et al.* 1957). We conclude therefore that almost all of the lines correspond to slip lines produced either during deformation or during polishing. (The same is also true for specimens thinned from both sides where slip traces are hardly ever observed immediately after insertion in the microscope.) The strain at the oxide metal interface must therefore persist over periods of hours or days. This is quite consistent with observations on slip traces in stainless steel; examination of slip traces in the same specimen after an interval of several days has shown that the traces in fact persist over this period of time.

It is possible however that some rearrangement of dislocations takes place during polishing. It seems unlikely that much rearrangement could occur, partly because the observed networks are often very complex, and partly because experiments on the movement of dislocations have shown that the dislocations are strongly pinned at the surface; thus while during thinning some of the obstacles blocking the dislocations might be released, the surface pinning force becomes more important, and furthermore, the range of elastic interaction between dislocations decreases (because they become shorter); both these effects would tend to prevent rearrangement of the dislocations. Nevertheless, the possibility of some rearrangement cannot be ruled out; for example, in metals in which cross-slip is possible, when the foil is thin those dislocations in pile-ups which cross the foil from top to bottom could change into the screw configuration and cross-slip out of the slip plane, thus dispersing the pile-ups. This is clearly not the case in stainless steel. It is nevertheless planned to test for possible rearrangments of dislocations during thinning in this and other metals by close correlation between surface slip lines and dislocations inside the specimen, and by comparing surface replicas before and after thinning of specimens.

In some areas slip lines can also be recognised as a result of a different contrast mechanism. In fig. 4 (Pl. 83) the transmitted intensity changes abruptly on either side of a slip line, and this is due to a change either in thickness of the specimen produced by the slip step, or in orientation of the crystal due to a set of dislocations on the slip planes. It should be noted that the transmitted intensity is a rather complicated (oscillating) function of thickness and of orientation; nevertheless abrupt changes of contrast as in fig. 4 can be taken as an indication of changes of either of these parameters.

The same effect may be seen in a different way in fig. 3, where a thickness contour runs across the slip lines. At each slip step the contour shifts (for example at A, B) as would be expected from a change of thickness, or of orientation. It should be noted that the former interpretation is valid in regions free of strain; on the other hand a set of screw dislocations on a slip plane would tend to twist the parts of the crystal on either side of the slip plane relative to each other, and this change of orientation would lead to a shift of the extinction contours. In fig. 3 however there appear to be rather few dislocations in the neighbourhood of the contour suggesting that the shifts are due to thickness changes.

3.1.2. *Steps at the edge of the thin foil*

In fig. 3 slip lines can be seen to be associated with steps at the edge of the electron microscope specimen. This edge is the line of intersection of the polished surface and the protected original surface which make small angles with each other at the edge. The edge of the thin foil is clearly wedge shaped. Because of the nature of this geometry a change in thickness of the specimen at a slip step gives rise to a much larger step at the edge of the thin foil. This magnification is due to the well-known 'taper section' geometry applicable in this case. It should be noted therefore that the steps at the edge of the thin foil correspond to a (considerably magnified) increase in thickness of the specimen, i.e. they correspond to the component normal to the foil of the slip step. Figure 5 shows the geometry of this effect. The plane ABDF is considered to be normal to the direction of the electron beam. BDE is the slip plane, the projection of BE, i.e. BF is the slip line and BC is the step at the edge of the foil. It is often possible to determine directly from the micrographs the taper angle in the active slip planes; thus from fig. 5 it follows that $l=a\phi$ (for small ϕ) where l is the slip step height measured in the slip plane and normal to BE, a is the length BC of the step at the edge of the foil measured along the intersection of the slip plane with the polished surface (i.e. BD), and ϕ is the taper angle (assumed small) in the slip plane. Further, $l=a\psi \sec\theta$, where ψ is the projection of ϕ on to the lower surface of the foil and θ is the angle between the slip plane and the plane of the foil. It should be noted that the foil could also be mounted in such a way that the plane

ABE is normal to the direction of the electron beam. Since ϕ and ψ are small in practice the results of the above analysis apply.

The taper angle ψ can be measured in a number of ways. For example in fig. 3 the dislocations become progressively shorter towards the edge, giving the taper angle ψ. Or ψ may be determined from a suitable slip trace, for example one nucleated at the edge (see Whelan *et al.* 1957); again, the variation in taper can sometimes be determined by measuring the thickness at various distances from the edge, either from the width of slip traces or lengths of dislocations in known slip planes.

In fig. 3 the shifts of the extinction contour at A and B correspond to the steps at the edge; this confirms the view expressed above that in the absence of strain the shift of the contours is due to a change in thickness. Since the shift of the contours is approximately equal to the length of the steps at the edge, the taper is probably reasonably uniform between the contour and the edge.

Fig. 5

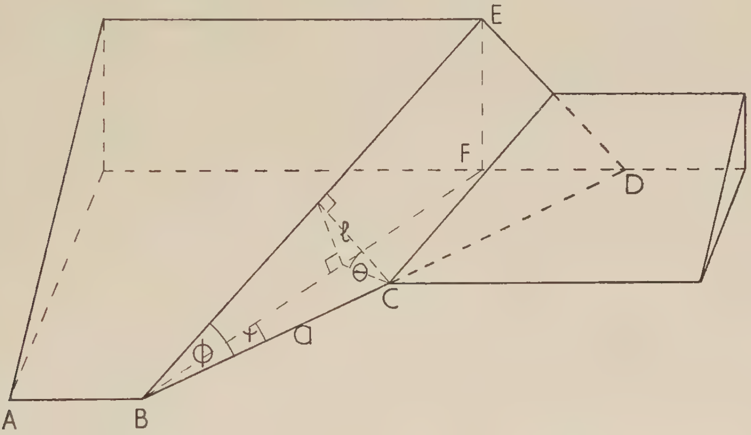

Geometry of taper section showing slip step magnification produced at the edge of the thin foil.

With an instrumental magnification of 100 000 times and a taper magnification of 10 times a millimetre edge step would correspond to 10 Å. Thus the technique is obviously a powerful one for studying the distribution of slip. Both the slip step height and the sense of the slip on different slip planes can readily be determined. The extreme edge of the foil would be expected to be rounded off during polishing. The only effect of this will be for the edge steps also to be rounded off. In fig. 5, ABC is the idealized shape. Rounding off will occur at B since polishing takes place along AB and BC and this effect can be seen in fig. 3. Nevertheless the length a can always be measured by extending the straight parts of the edge to intersect DC produced.

3.2. *Correlation of Number of Dislocations on Slip Plane and Slip Step Height*

In fig. 3 the number of dislocations on the slip planes can be counted and knowing the taper angle the offset expected from these and that measured by the taper section technique can be compared. In the case of plane B, where the dislocations can most readily be counted we have 12 dislocations and hence $l = 30$ Å for the Burgers vector nearest the foil normal. For this step $a \simeq 2{\cdot}5$ mm at a magnification of 70 000 times, $\theta = 72°$ and $\psi \simeq 2{\cdot}0°$; hence $l \simeq 40 \pm 20$ Å. These two estimates of l are consistent with each other, but considerably better accuracy is required to make the correlation precise.

Figure 6 (Pl. 81) suggests that it may be possible to make a similar comparison in another way. At A the slip steps on one system are offset by slip on a second system. Now between the two offsets indicated there are a number of dislocations on the crossing system. The difference in the offsets though small is measurable and can be compared with the displacement expected from the ten dislocations between them. The difference between the offsets is about 40 Å which is twice as great as the value corresponding to the observed dislocations. This difference is presumably due to slip occurring on one of the offset systems after the other and after the crossing system had begun to operate.

It is possible to check the accuracy of the taper section measurements by comparing them with the offsets on slip lines where slip has occurred on two systems. In fig. 4 offsets and edge steps can be compared but, because there is a choice of Burgers vectors, no definite conclusions can be drawn, although the two types of measurement are found to be consistent with each other.

The results described in this section are of a preliminary nature, and are intended to show only that it is possible with this technique to make quantitative estimates of the magnitude of features on the atomic scale.

3.3. *Dislocation Arrangement at the Surface after Deformation in Tension*

The arrangement of the dislocations at the surface is found to be very similar to that observed previously in the interior of the specimen (Whelan *et al.* 1957). Thus the dislocations are generally arranged in pile-ups or networks on the slip planes (figs. 1, 2). These networks are the result of interaction of the piled up dislocations with others on intersecting systems. Figure 2 shows many extended and contracted nodes of the type discussed in detail by Whelan (1959). It appears that some of the dislocations taking part in the network A are on a slip plane slightly displaced from that containing most of the dislocations. Although no systematic statistical average has been obtained from the micrographs, the networks or pile-ups often contain about 20–30 dislocations corresponding to slip displacements ~50–75 Å in agreement with the order of magnitude of the size estimated from the edge steps (see figs. 3, 4).

Examination of the sense of the edge steps shows at once that in general this is the same for most of the slip steps after unidirectional deformation (see figs. 3, 4). Taking the average displacement to be ~50 Å, and the spacing of the slip lines ~1000 Å, the average shear strain is found to be ~5%, i.e. of the correct order of magnitude (the deformation of the specimens corresponding to figs. 3, 4 was 10%).

While many of the dislocations are arranged in networks at the surface, as for example in fig. 2, it should be noted that if an etch pit technique had been used to reveal the dislocations, a sequence of pits resembling that of an irregularly spaced pile-up would have been observed. It is clear therefore that the interpretation of an array of etch pits in terms of a detailed arrangement of dislocations has to be carried out with caution.

3.4. *Some Observations on Fatigued Specimens*

The surface of a metal is particularly important in the study of fatigue. The first fatigue cracks are often if not always formed at the surface. In a number of face-centred cubic metals these cracks have been shown to occur during the first few percent of the life in the broad slip bands known as striations which develop during fatigue (for review see Thompson and Wadsworth 1958). It is of interest to study with the present technique the distribution of slip and the nature of the defects in the striations, the surface contour across them and, if possible, to observe the cracks at an early stage of their formation.

Figure 6 shows the appearance of the surface of a fatigued specimen. Area B shows slip lines and a dislocation arrangement not unlike that in a unidirectionally deformed specimen. At C however, there is a striation consisting of many closely spaced slip lines. There is also a very high density of dislocations in this region; the resolution is however too poor to make any estimate of this. Another feature often observed is the presence of patches of stacking faults in the slip bands, as at D, or in the striations.

Figure 7 (Pl. 84) shows the distribution of slip near the edge of the thin foil. In contrast to the micrographs obtained from unidirectionally deformed specimens the sense of the slip steps alternates frequently. Another distinguishing feature is the fact that some quite distinct slip lines have no steps associated with them, for example at A. While this could be due to slip with a Burgers vector in the plane of the foil, it is likely that the Burgers vector corresponding to the slip lines in the same area will be the same. We suggest therefore that these lines are the result of to and fro slip either on the same plane or on closely neighbouring planes. Some of the lines also show lighter contrast (for example at B) of a type not observed in unidirectionally deformed specimens. While the interpretation of these lines is not yet clear it is possible that they correspond to the early stages of cracks along the slip lines.

Figure 8 (Pl. 85) shows a very pronounced striation. Here the surface contour of the striation is revealed by the steps at the edge of the thin foil. The taper magnification is approximately 10 times, the magnification of the micrographs is 45 000 times, and hence the magnification of the steps is approximately 450 000 times. This is to be compared with a magnification of 20 × 1000 times achieved in recent taper section experiments of Wood and Segall (1957) and Wood (1958), who used an optical method. It is clear from this micrograph that slip can take place in opposite directions at spacings as close as ~50 Å. Both projections and fissures can be observed. Some of the former project above the mean surface level (i.e. in a direction normal to the plane of the foil) by about 300 Å. (It should be remembered when examining this micrograph that the magnification at the edge in the direction of the arrow is about ten times that at right angles to it. Hence the height of the projections is about equal to the width of their base.) The peaks undoubtedly represent genuine projections above the surface and may correspond to the early stages of the extrusions described by Forsyth and Stubbington (Forsyth and Stubbington 1955, Stubbington and Forsyth 1957). While the fissures correspond probably to intrusions, it is possible that they might be due to preferential polishing at a slip plane. The same argument applies to the white lines which can be observed and which sometimes end in fissures. In principle it might be possible to determine whether the white lines correspond to depressions in the protected surface or polishing groves on the other surface; in the former case they should appear as single lines; in the latter they should be paired with a slip line. There is little doubt that some of the white lines in fig. 7 represent actual fissures since they occur singly. In fig. 8 the slip lines are so closely spaced that it is difficult to be sure of the interpretation. Whatever the origin of the white lines or fissures might be, there is no doubt that they correspond to structural features not present in unidirectionally deformed specimens. Close examination of the white lines in fig. 8 also reveals that they consist of a series of closely spaced short white lines running transversely across them; the origin of this structure is not understood.

§ 4. Conclusions

The preliminary results obtained so far with the technique described in this paper for studying the surface of a metal, show that it combines the advantages of the transmission and replica methods of electron microscopy. It has been shown that in stainless steel it is possible to see the dislocations in the metal associated with the slip lines. The distribution of dislocations at the surface is similar to that in the interior of the metal. The height of the slip steps and surface contours, for example of fatigue striations, are revealed at a high magnification by the steps at the edge of the foil due to a taper section effect. It appears that the technique is likely to prove particularly useful for correlation between dislocation arrays and slip lines, and for the study of the distribution of slip, fissures, projections, and dislocation arrangements in fatigued specimens.

Acknowledgments

The authors wish to thank Professor N. F. Mott, F.R.S. and Dr. W. H. Taylor for encouragement and helpful discussion during the course of this work. We would also like to thank Dr. M. J. Whelan and Mr. A. Howie for numerous helpful criticisms and suggestions, Mr. C. K. Jackson for careful attention to the performance of the microscope and Mr. J. Bell for help with the photographic work. One of us (R.L.S.) is indebted to the Commonwealth Scientific and Industrial Research Organization, Australia and one (P.G.P.) to the Admiralty for financial support.

REFERENCES

FORSYTH, P. J. E., and STUBBINGTON, C. A., 1955, *J. Inst. Met.*, **83,** 395.
HIRSCH, P. B., HORNE, R. W., and WHELAN, M. J., 1956, *Phil. Mag.*, **1,** 677.
HIRSCH, P. B., PARTRIDGE, P. G., and TOMLINSON, H. M., 1958, *Fourth International Conference on Electron Microscopy* (in the press).
MADER, S., 1957, *Z. Phys.*, **149,** 73.
STUBBINGTON, C. A., and FORSYTH, P. J. E., 1957, *J. Inst. Met.*, **86,** 90.
THOMPSON, N., and WADSWORTH, N. J., 1958, *Advanc. Phys.*, **7,** 72.
TOMLINSON, H. M., 1958, *Phil. Mag.*, **3,** 867.
WHELAN, M. J., HIRSCH, P. B., HORNE, R. W., and BOLLMANN, W., 1957, *Proc. roy. Soc. Lond.* A, **240,** 524.
WHELAN, M. J., 1959, *Proc. roy. Soc. Lond.* A, **249,** 114.
WILSDORF, H., and FOURIE, J. T., 1956, *Acta Met.*, **4,** 271.
WOOD, W. A., and SEGALL, R. L., 1957, *Bull. Inst. Met.*, **3,** 160.
WOOD, W. A., 1958, *Phil. Mag.*, **3,** 692.

The Silver-based Heusler Alloys†

By E. O. Hall
Department of Physics, University of Sheffield‡

[Received December 12, 1958]

Abstract

The structures of some fifty alloys of silver, manganese, and aluminium have been studied with a view to explaining the magnetic properties of these alloys. Approximate equilibrium diagrams were made at 400°c and 650°c, and the alloys were also examined after quenching from the latter temperature. It follows from this examination that ferromagnetism in alloys in the vicinity of the atomic composition Ag_5MnAl is not associated with any equilibrium product, but arises from a finely dispersed nucleation structure, which grows during ageing into a Widmanstätten pattern and eventually transforms above the Curie point into β-manganese, rendering the alloy non-ferromagnetic. The ferromagnetic precipitate was extracted and identified by electron diffraction as having an ordered hexagonal structure with $a=2{\cdot}94$ Å, $c/a=1{\cdot}61$. This result is used to discuss the variation of magnetization with temperature in these alloys, and also the origin of their very high coercivities. A brief discussion of the valency of manganese in these structures is also included.

§ 1. Introduction

The silver–manganese–aluminium alloys are ferromagnetic and belong to a series known as the Heusler alloys, after their discoverer (F. Heusler 1903). The original compounds, discovered in 1898, were copper-based alloys, and it was later found (O. Heusler 1928) that the maximum intensity of magnetization arose in alloys, centred around the composition Cu_2MnAl, which had been quenched from a temperature well above the Curie point, and then subjected to a low temperature ageing treatment. The structure associated with the ferromagnetic phase was not solved until Bradley and Rogers (1934) concluded that it was an ordered structure based on a body-centred cubic cell, the atoms in the body centre being alternately manganese and aluminium, and the corner atoms copper.

The solution of this structure presented a fundamental difficulty, because the x-ray scattering factors of copper and manganese are virtually identical. Prior to this, Potter (1931) had endeavoured to overcome this by substituting monovalent silver for monovalent copper, but in doing so, he found that the maximum intensity of magnetization arose not at Ag_2MnAl, but at Ag_5MnAl. Figure 1 shows Potter's results, redrawn to give contours of equal saturation intensities per cubic centimetre. The cross marks the composition Ag_5MnAl.

---

† Communicated by the Author.

‡ Present address: School of Metallurgy, Newcastle University College, Newcastle, N.S.W., Australia.

Potter discovered three further facts. The maximum intensity of magnetization was achieved by chill-casting and ageing the alloy for several days at 250°c. Secondly, the magnetization was rapidly destroyed by heat treatment above the Curie point ($\sim$350°c), and finally the x-ray powder patterns taken from this alloy in its magnetic state showed only the pattern of a silver solid solution. Thus, no evidence could be obtained for a phase isomorphous with the structure of Bradley and Rogers.

Fig. 1

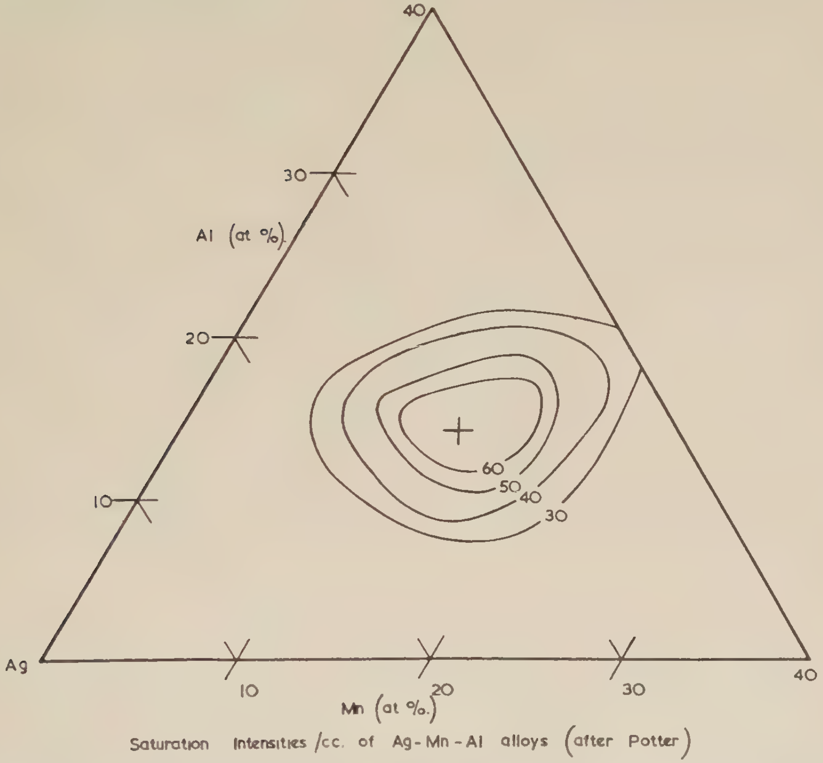

Magnetization contours in e.m.u./cm^3 of the ternary alloys (after Potter (1931)).

The alloy Ag_5MnAl, which has been given the name 'Silmanal' is characterized by a low intensity of magnetization, but has a very large coercive force. Values of 5000 oe are common, and more than 8000 oe can be reached under certain conditions. Apart from advances in the technical applications of these alloys, however, no further fundamental investigations were made on the structures of the alloys, with the exception of a brief report by Geisler (1951) which will be discussed in § 6. A detailed survey was therefore undertaken in this Department.

§ 2. MATERIALS AND APPARATUS

The alloys used in this investigation were prepared from fine silver grain (99·99% Ag), Johnson-Matthey H. S. manganese, and high-purity aluminium. The materials were melted together in an argon-arc furnace, and homogenized in evacuated silica tubes at a suitably high temperature close to the solidus of the alloy concerned. For the purposes of identification in the course of this paper, the alloys will be enumerated in terms of their atomic compositions, although this does not imply the presence of any intermetallic compounds, nor that the actual composition as shown by subsequent analysis is that indicated by the formula.

Microscopic examination was made on specimens polished either with fine alumina or liquid silver polish ('Silvo'), and etched in most cases in a 5% solution of potassium cyanide and ammonium persulphate, although, for alloys low in silver, an acid ferric chloride etch appeared more satisfactory. The preparation of these alloys for photomicroscopy was tedious, for in nearly all cases the structures consisted of a hard and brittle precipitate (β–manganese, for example) in a soft matrix of silver. Despite extreme care, a certain amount of pitting is present in most microsections. Over fifty alloys were so examined, most of which contained less than 50 at. % of aluminium, but for the purposes of this discussion, remarks will be confined to the silver-rich corner of the phase diagram.

X-ray investigations were used to complement the micrographic work, and in addition to the normal cameras, involved the use of a Unicam S150 High Temperature evacuable powder camera. Samples of filings were sealed *in vacuo* in thin-walled silica capillaries.

Finally, the identification of the non-equilibrium precipitates in the dilute alloys around the composition Ag_5MnAl could only be undertaken with extraction techniques familiar in electron microscopy, and using here a Metropolitan-Vickers EM3 machine, which has facilities for electron diffraction.

§ 3. THE PHASE DIAGRAMS

The major difference between the copper-based and silver-based Heusler alloys lies in the behaviour of the β (body-centred cubic) fields of the two binary systems, copper–aluminium and silver–aluminium, occurring around 25 at. % aluminium. In the former the β phase is in principle stable after quenching from elevated temperatures, although in practice it partially transforms to other complex products (Gawranek *et al.* 1936). The addition of manganese to this system apparently suppresses this martensitic transformation, and produces the highly ordered structure characteristic of the Heusler alloys. In the silver–aluminium system, however, the β phase is only stable at elevated temperatures and decomposes completely, again by a martensitic transformation, into a close-packed hexagonal structure (ζ). The equilibrium structure (μ) below 450°C is isomorphous with β-manganese. One of the first objects of this investigation was therefore to see if the β phase could be retained at low temperatures by the addition of manganese.

To reduce the large amount of labour normally involved in ternary diagram studies, the problem was reduced to a consideration of structures normally present under the following conditions:

(i) The section of the equilibrium ternary diagram at 400°c. This temperature was chosen as close to but above the Curie points of the alloys concerned.

(ii) The section of the equilibrium diagram at 650°c. This is within the β phase field of the binary system, but could only be examined using high-temperature x-ray studies.

(iii) The structures arising after quenching in water from 650°c. These non-equilibrium structures are related to the development of the ferromagnetic properties.

Fig. 2

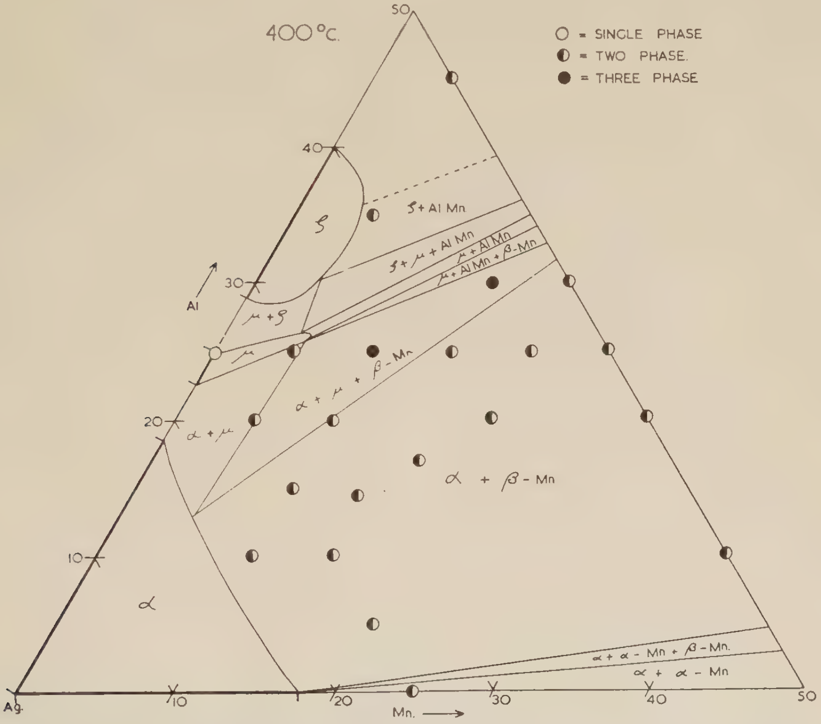

Approximate equilibrium diagram for the silver–manganese–aluminium system at 400°c.

A feature of the investigation was the rapidity at which equilibrium was reached, even at 400°c. Annealing for 24 hours at that temperature gave structures which differed little from those annealed for 7 days, although the latter period was adopted in all cases. At 650°c, equilibrium was attained in the course of a few hours, and the specimens could be successfully heat-treated within the high temperature x-ray camera itself.

The main intent in obtaining the ternary diagrams was to identify the phases appearing in the ferromagnetic alloys, and no high accuracy is claimed for the diagrams. However, they appear essentially simple, no intermetallic compounds have been discovered, and it is felt that the number of alloys examined enables the trend of the boundaries to be given with fair certainty, at least in the silver-rich region. Thus, only about half the alloys examined appear marked on the diagrams, the remainder (of lower silver content) merely served to confirm the run of the boundaries.

Fig. 3

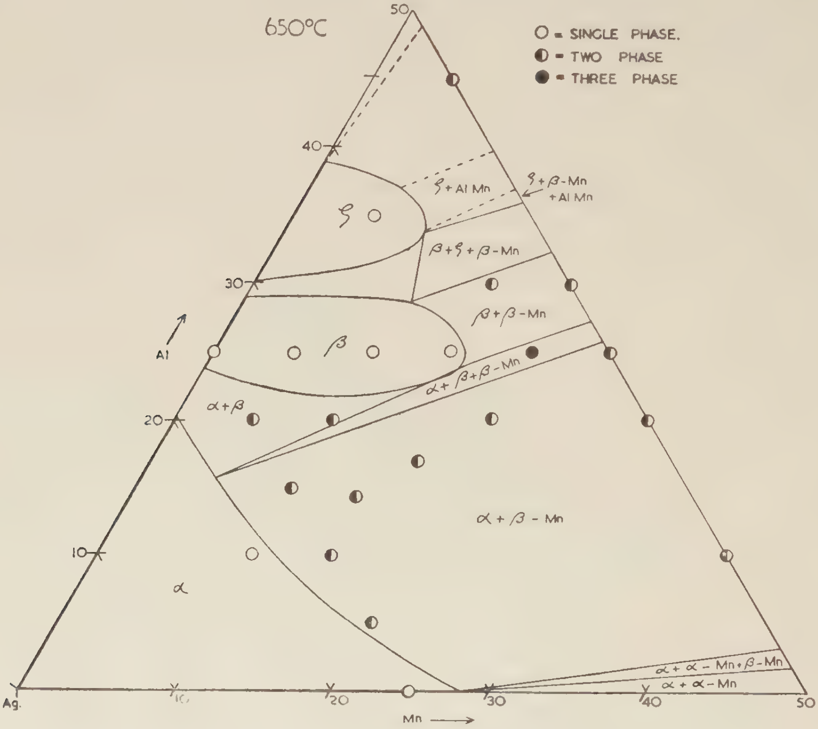

Approximate equilibrium diagram for the system at 650°c.

The diagrams are the combined results of x-ray and micrographic examination in conditions (i) and (iii) outlined above, while the section at 650°c is from high-temperature x-ray investigations alone, with correspondingly lowered accuracy.

Figure 2 therefore shows the 400°c section of the silver-rich corner of the equilibrium diagram for specimens quenched from that temperature. It will be seen that the alloys around the composition Ag_5MnAl lie within a broad two-phase field where the equilibrium structure is α–Ag + β–Mn. The absence of intermetallic compounds show a further difference between this system and the Cu–Mn–Al series (West and Thomas 1956). The μ

phase, although isomorphous with β–Mn, has only a very limited extent, and shows no tendency, as might be expected, to form a single phase band with its isomorphous structure in the manganese–aluminium system. The direction of this field may fairly reliably be determined by the constitution of the alloy $Ag_{14}Al_5Mn$, where the minor constituent (α) could be detected by x-ray examination because of its high scattering factor. The extent of the ζ field is not well established, but again is not of importance in this discussion.

Fig. 4

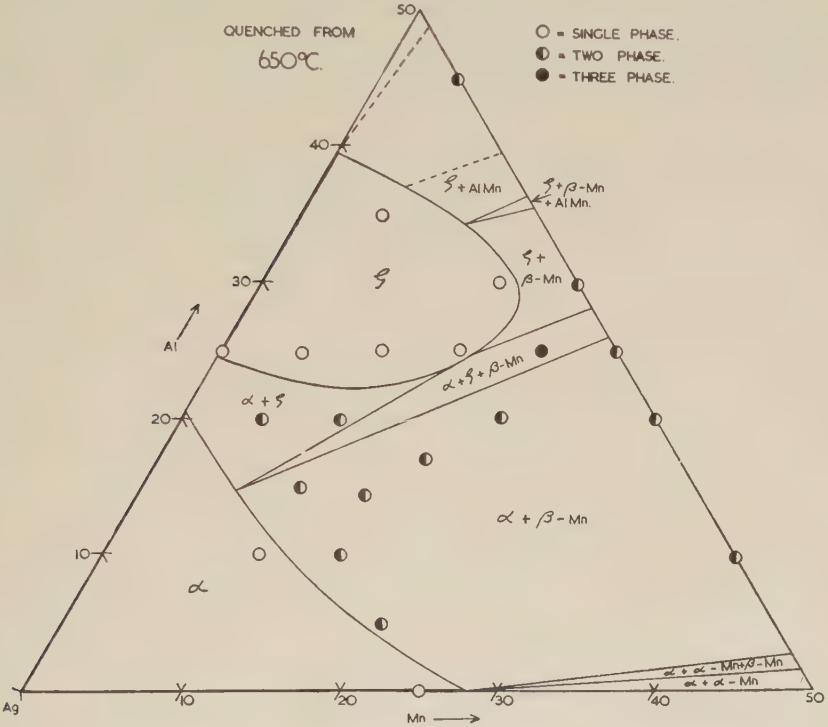

Approximate constitution diagram for the system, quenched from 650°c.

Figure 3 shows the section at 650°c. As in the copper–manganese–aluminium system, the β field has extended to cover a large area of the diagram, and overlaps, though incompletely, the area of the strongly ferromagnetic alloys. A limited number of investigations at even higher temperatures (up to 790°c) showed that the β phase could extend still further, close to but not embracing the Heusler composition Ag_2MnAl. It is therefore apparent that the strongly ferromagnetic alloys contain at most only a small proportion of β at 650°c—those around the 'Silmanal' composition contain none.

Finally, fig. 4 shows the constitution diagram of alloys quenched in water from 650°c. In no case was it found that the β phase was stabilized by the addition of manganese, in striking contrast to the Heusler alloys. A large single-phase loop of ζ is therefore formed, which, dependent on composition will generally decompose into α–Ag + β–Mn on reheating to elevated temperatures. The other point of note here is that the increased solubility of manganese in silver gives rise to an enlarged α solid-solution field, and precipitation of β–Mn is therefore to be expected in the 'Silmanal' region at higher temperatures.

§ 4. MICROSTRUCTURES

The optical micrographic work as mentioned in § 2 was an integral part of the phase diagram determinations of the previous section, and helped to identify the structures present, particularly at low precipitate concentrations. Certain new features however are relevant to the formation of the magnetic alloys.

4.1. *The* 400°C *Section*

The three-phase field (α–Ag + μ + β–Mn), shown in the 400°C section, is easily identified; an acid ferric chloride etch proving suitable here. Figure 5 (Pl. 86) shows the alloy $Ag_3Al_4Mn_3$ which is close to the centre of this field.

The two-phase α–Ag + β–Mn field within which the magnetic alloys lie is, however, more important. Alloys low in silver show a clumped precipitate of β–Mn in the α matrix.

Figure 6 (Pl. 86) shows the alloy Ag_2MnAl, with a structure characteristic of alloys containing 50 at. % or less silver. As the silver content is increased, however, the alloy Ag_3MnAl shows (fig. 7, Pl. 87) that a finely divided Widmanstätten precipitate has developed, while the amount of the clumped precipitate is diminishing. The proportion of the Widmanstätten pattern increases in the alloy Ag_4MnAl, (fig. 8, Pl. 87), while in 'Silmanal' itself Ag_5MnAl (fig. 9, Pl. 88), the only clumped precipitate is a small amount left in the grain boundaries themselves, and all the grains are covered with the Widmanstätten precipitate. Thereafter, the amount of precipitate decreases rapidly as the α boundary is approached, so that in Ag_8MnAl only a very fine precipitate is left, just within the limit of resolution of the microscope.

This Widmanstätten pattern is therefore a feature which, in its development, follows the magnetization contours of Potter's alloys (fig. 1), and therefore suggests it is the remains of a magnetic phase. However, it cannot constitute a ferromagnetic precipitate, since these micrographs (figs. 5–9) are taken from specimens annealed at 400°C, where, as Potter (1931) showed, the magnetization is rapidly destroyed. The structure of the precipitate below the Curie point is therefore of prime importance, since the equilibrium structure (β-Mn) is always paramagnetic.

4.2. *Non-equilibrium Precipitates*

Four specimens of 'Silmanal' (Ag_5MnAl) were then heat-treated at 790°C in an evacuated silica tube and quenched in water. One specimen (magnetic) was examined in this state, two others were annealed for 7 days at 240°C and 310°C respectively yielding other ferromagnetic alloys, and one for 7 days at 400°C. The latter was tested and found non-magnetic. The specimens were then polished and carefully etched in cyanide-persulphate solution, and examined under high power to observe the development of the precipitate. In the case of the first two magnetic alloys, (i.e. unaged and aged at 240°C), the precipitate was barely resolved. Figure 11 (Pl. 89) shows the specimen aged at 310°C—the large specks are undissolved β–Mn, but it is apparent from the etching attack that a fine background precipitate has formed which must be the ferromagnetic phase. In the specimen aged at 400°C, however (fig. 12, Pl. 89), the typical Widmanstätten precipitate has again appeared. The higher ageing temperature should yield a coarser precipitate, but at this stage the transformation to β–Mn has taken place. It is therefore concluded that the ferromagnetic constituent is an intermediate phase, formed during the nucleation of β–Mn, which can grow into platelets crystallographically related to the matrix, and which transforms to the equilibrium structure at temperatures above the Curie point. A final solution to this problem could therefore only be reached by extraction of this constituent itself.

§ 5. ELECTRON MICROSCOPY

Extraction of the ferromagnetic precipitate was first attempted by electrochemical means. A suitable specimen of 'Silmanal' was made the anode of a bath of 10% citric acid in water; the cathode was a silver foil. The sludge formed was collected on a sintered glass filter, dried, and further separation carried out over an alternating current electromagnet. Despite many attempts, the separation thus achieved always yielded a sample whose x-ray patterns were that of silver, and the technique was abandoned.

A successful extraction technique was eventually developed using the carbon replica technique familiar in electron microscopy. A film of carbon, some 50–100 Å thick, is evaporated onto the polished and lightly etched surface of the specimen, which is then immersed in a 10% cyanide–persulphate bath. The etch diffuses through the carbon film and attacks the matrix, and, after sufficient time has elapsed, the carbon can be floated off on water, carrying with it not only a replica of the surface, but also the precipitate particles embedded in it. Since this etchant is normally slow, prolonged immersion was usually necessary; periods up to one hour were common. In obstinate cases, the films were finally removed by a brief immersion in 10% nitric acid in alcohol.

By this means, replicas of the magnetic and non-magnetic samples mentioned in § 4 were obtained, from which high-resolution electron micrographs and also electron diffraction patterns could be obtained.

Figure 13 (Pl. 90) shows the structure of the sample aged at 240°C. The particles are seen to be irregular in shape, and generally less than 1000 Å in diameter. A few examples of needle-like particles were seen, roughly 5000 Å long and 500 Å across, which presumably were to become the Widmanstätten pattern appearing at higher ageing temperatures. The electron diffraction pattern of the precipitate is shown in fig. 14 (Pl. 90). Not all the diffraction rings can be reproduced because of the high contrast, but on the original nine rings can be distinguished, and their Bragg spacings (d) determined. A small correction to the d values is needed, since the accelerating voltage is not exactly the nominal 75 kv. This can be made by evaporating a layer of thallium chloride (whose structure is known) onto the surface of the replica, and plotting a graph of true d values against measured d values. A straight line relation is obtained, whereby the d values of the precipitate can be similarly corrected.

Analysis of Electron Diffraction Pattern from 'Silmanal' Extract

Ring no.	Radius (cm)	Corrected d (Å)	$\{hkil\}$
1	0·53	4·72	$\{0001\}$
2	0·94	2·66	$\{10\bar{1}0\}$
3	1·07	2·34	$\{0002\}$ $\{10\bar{1}1\}$
4	1·41	1·78	$\{10\bar{1}2\}$
5	1·59	1·58	$\{0003\}$ $\{11\bar{2}0\}$
6	1·84	1·36	$\{1013\}$ $\{20\bar{2}0\}$
7	1·92	1·31	$\{11\bar{2}2\}$ $\{20\bar{2}1\}$
8	2·13	1·18	$\{0004\}$ $\{20\bar{2}2\}$
9	2·33	1·07	$\{10\bar{1}4\}$

The table shows the results for the extract. The analysis of the results is achieved by a consideration of the possible structures which may arise. The Heusler structure has certain characteristic absences, and the intense lines have hkl values such that $\sum h^2 = 8, 16, 24, 32 \ldots$ and weaker superlattice lines with $\sum h^2 = 3, 4, 11, 12, 19 \ldots$. Although the intensities of X-ray and electron diffraction patterns are not strictly comparable, the intense lines certainly do not follow this pattern, nor in fact can a good cubic parameter be found for the lines. On the other hand, it is easy to see that the d values of lines 1, 3, 5, and 8 bear a simple ratio to one other, and trial plotting with Bunn charts allowed all the lines to be satisfactorily indexed, giving a primitive hexagonal cell with parameters $a = 2{\cdot}94$ Å, $c/a = 1{\cdot}61$. This phase will be designated ζ', and must therefore be the ferromagnetic constituent.

Replicas from the specimen aged at 400°C revealed the typical Widmanstätten structure which had been observed in figs. 9 and 12, but in greater detail (fig. 15, Pl. 91). Extraction of the coarser precipitate proved difficult here, but satisfactory evidence was obtained that the structure present in this state was predominantly β-manganese ($a = 6{\cdot}39$ Å).

§ 6. Discussion

The results so far described have shown that the presence of ferromagnetism in the silver-based Heusler alloys is due to the presence of a non-equilibrium precipitate which forms on ageing from the super-saturated silver matrix, grows into a Widmanstätten structure, and eventually transforms above the Curie point into the equilibrium product, β–manganese.

It is only possible at this stage to say little more about the crystal structure of this ferromagnetic phase. However, the existence of strong diffracted intensities of the form $\{000l\}$ with l odd show that the lattice in its magnetic state is ordered. It is not, however, possible to distinguish between say, a nickel arsenide structure and any other hexagonal type which gives rise to ferromagnetism. The nickel arsenide structure can probably be rejected, since this cell is somewhat smaller than the equivalent structures MnAs and MnSb, bringing the manganese atoms too close together. If, on the other hand, the ordered structure results from sheets of manganese and aluminium atoms, separated by other sheets of silver atoms, the closest distance of approach of the manganese atoms could be equal to the c axis, 4·70 Å. This compares with a manganese separation of 4·18 Å in Cu_2MnAl, 4·37 in Cu_2MnSn, and 4·39 in Cu_2MnIn.

6.1. *Comparison with Previous Work*

It was mentioned in § 1 that the only previous work on the structure of these alloys was that of Geisler (1951), and it is now possible to make a detailed comparison with the present results.

In the course of a study on the structures of permanent magnet alloys, Geisler examined microsections of Ag_5MnAl, and noted the presence of a precipitate with a Widmanstätten structure. After a consideration of alloys around this composition, he concluded that ‘ Silmanal ’ was a simple precipitation hardening alloy, and that the precipitate itself had the cubic Heusler structure. The present work shows that this is not the case, and the presence of a Widmanstätten structure is not necessarily evidence of a ferromagnetic state.

The other point of note concerns the orientation relation between the Widmanstätten structure and the matrix. From the microstructures, Geisler concluded that the platelets were aligned with the $\{001\}$ planes of the matrix. The lattice parameters found here suggest an alternative orientation. Mehl and Barrett (1931) noticed the appearance of just such a Widmanstätten pattern in a binary alloy of silver and aluminium containing 20·2% silver, where the equilibrium structure is a precipitate of ζ in a face-centred cubic matrix. X-ray examination showed that the orientation of the precipitate was

$$(0001)_p//(111)_m,$$

$$[11\bar{2}0]_p//[\bar{1}10]_m.$$

In the present case, the lattice parameter of the terminal silver solid solution (4·064 Å) is very close to that of the aluminium solid solution studied in the binary alloy; the hexagonal parameters likewise correspond. Calculations then show that if this orientation relationship were maintained here, fitting would be achieved with a linear strain of 2·3% along the a-axis, and only 0·6% along the c-axis.

It is tempting to pursue the analogy between the present case and the binary silver–aluminium alloy. Walker and Guinier (1953) on the basis of low-angle x-ray scattering experiments showed that at early stages of the precipitation of ζ in the binary alloy, the particles were spherical, and it was only at the later stages of ageing that the particles assumed a platelet form. A consideration of figs. 13, 14 and 15 suggest that this may also hold in the ternary system.

It must not be assumed, however, that there is any close relationship between the ζ phase in the quenched alloys or in the equilibrium structure, and the ζ' phase responsible for the ferro-magnetism. For example, the ζ phase never forms a Widmanstätten pattern in quenched alloys, and if it were responsible for the ferromagnetism, the maximum intensities of magnetisation would lie much closer to the composition Ag_3Al than they in fact do. Further evidence against this association will be given below, and since all the magnetic alloys lie in the binary field α–Ag + β–Mn, ζ' would appear to be simply a non-equilibrium nucleation phase in the precipitation of β–manganese from the supersaturated matrix.

6.2. *Magnetic Measurements*

A large amount of unpublished data has been obtained in this Department on the magnetic properties of 'Silmanal' and associated alloys, but in this discussion attention will be concentrated on two of interest, (i) the variation of magnetization with temperature, and (ii) the origin of the very high coercivities in these alloys.

The variation of saturation magnetization with temperature provides further evidence for the distinction between the ζ' (magnetic) and the ζ (non-magnetic) phases. Figure 16 shows the variation of intensity of magnetization (I) against temperature, for the alloy Ag_7Al_2Mn, which is the alloy closest to Ag_5MnAl where the precipitate ζ can be detected in the quenched state. The curves show that in the chill-cast or quenched condition, I is low but after a heating and cooling cycle to a temperature above the Curie point, I is markedly increased. The interpretation here is that the $\alpha + \zeta$ structure in the as-quenched state transforms to supersaturated α or even $\alpha + \zeta'$ in the transition to the equilibrium $\alpha + \beta$-Mn structure, and hence on cooling a large number of the ferromagnetic nuclei of ζ' remain.

In 'Silmanal' itself (fig. 17) the result is very different. Here the chill-cast or quenched specimens show the maximum value of I, and any prolonged heat-treatment above the Curie point reduces this by a large factor, the ζ' phase transforming rapidly to the equilibrium β–Manganese. Since both these alloys lie in the binary equilibrium field of α–Ag + β–Mn, and since I for Ag_7Al_2Mn is less than I for Ag_5MnAl, there must therefore be important differences in structure or ordering between the ζ and ζ' phases.

Fig. 16

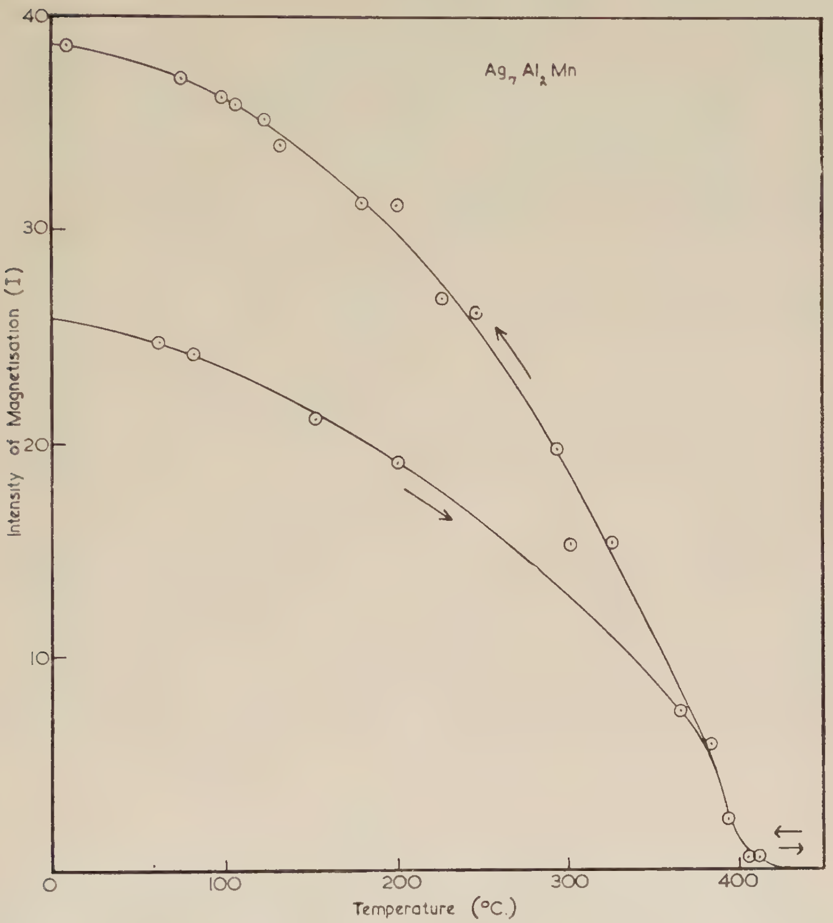

Variation of intensity of magnetization with temperature for Ag_7Al_2Mn.

One can further predict that all alloys in the α–Ag + β–Mn binary region will be similarly ferromagnetic. Even those low in silver will dissolve a small amount of β–Mn on heat-treatment. Some of this will precipitate as ζ' on quenching, and ageing will render the alloy ferromagnetic. As an example, the alloy $AgAlMn_3$ was found to be weakly ferromagnetic after suitable heat-treatment.

6.3. *Origin of the Coercive Force*

Kittel (1949) has reviewed the origins of high coercivities for small, single domain particles, which are generally stated to be due to either (i) shape, (ii) magnetocrystalline anisotropy, or (iii) strain. In the silver-based Heusler alloys a finely dispersed magnetic phase is present, with particles under 1000 Å which are in all probability of single domain size. Further, it has been shown that the coherency strains are so low that this effect may be ignored.

Fig. 17

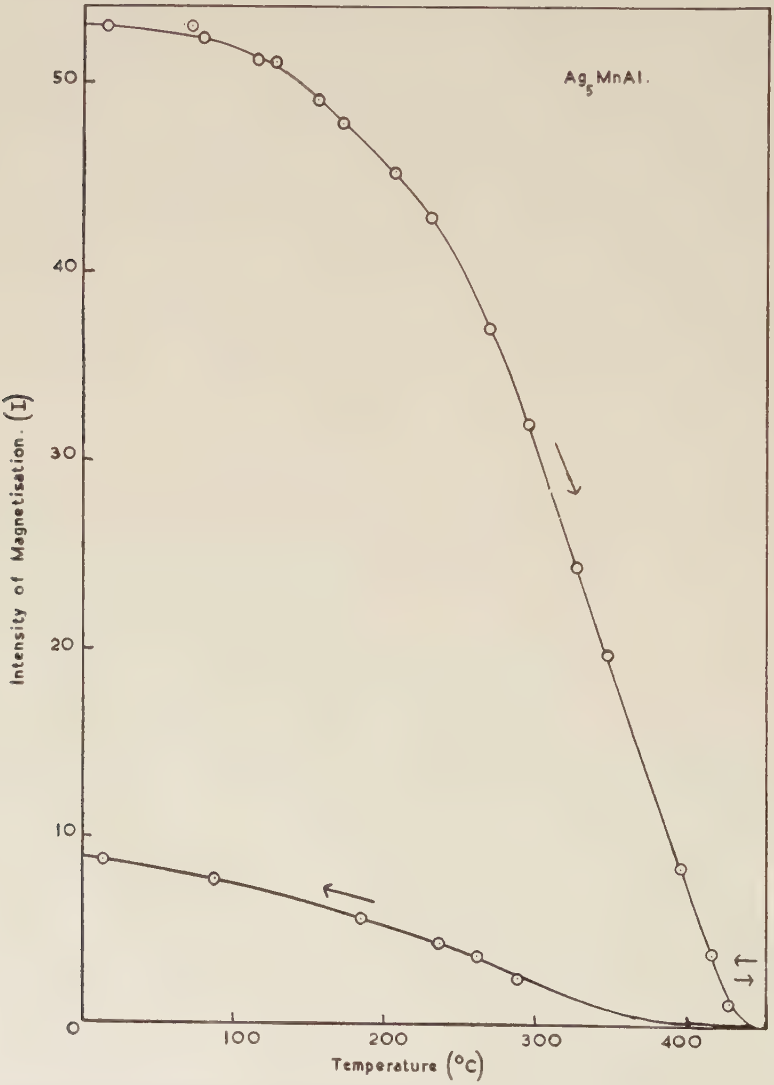

Variation of intensity of magnetization with temperature for Ag$_5$MnAl.

In high coercivities due to shape anisotropy, single domain particles can produce a maximum theoretical coercivity H_c given by

$$H_c = 2\pi I_s$$

where I_s is the saturation magnetization for material in the form of long cylinders. The electron micrographs, however (fig. 13) show that the precipitate particles in the magnetic state are irregular in shape and do not possess these high axial ratios. It is only in specimens heat-treated at higher temperatures (fig. 15) which these axial ratios of 10 or more are found for the precipitate particles, and by this stage the specimen is non-magnetic. Furthermore, approaching this state the particles are almost certainly larger than single domain size, and as Meiklejohn (1953) has shown, the presence of only a small proportion of multidomain particles will appreciably lower the coercivity of a specimen. Alternatively, one may exclude shape anisotropy as a possible mechanism from an estimate of I_s for the precipitate. I_s for the alloy Ag_5MnAl reaches a maximum value of 55–65, and if it is assumed that the particles occupy less than 5% of the total volume (cf. fig. 12), I_s for the particles may have a maximum value of 1300 and $H_c \ngtr 8000$, while values of $H_c \simeq 8300$ oe have been reported in 'Silmanal' (Hollis, private communication).

By the process of elimination, it is therefore more likely that magnetocrystalline anisotropy is the predominant factor, giving a theoretical coercivity

$$H_c = 0{\cdot}64\, K/I_s$$

for particles distributed at random with respect to the field, where K is the anisotropy constant. Lacking knowledge of the value of K, we can only assume that its magnitude, in common with other uniaxial crystals, is high. More significantly, however, a plot of H_c against temperature should fall off more rapidly than a plot of I_s against temperature, since anisotropy is more readily affected by increased temperatures than the saturation magnetization. This is, in fact, found to be the case (Hollis, private communication).

6.4. THE VALENCY OF MANGANESE

The β phase fields of the Cu–Al and Ag–Al alloys are both examples of intermetallic compounds having a 3 : 2 electron–atom ratio. Coles *et al.* (1949) have suggested that the Heusler structure (Cu_2MnAl) itself belongs to this category, and for this to be so, the manganese atoms must be exerting a valency of unity. On the other hand, Hume-Rothery (1948) has shown, from a consideration of the form and direction of the β phase boundary in Cu–Mn–Al alloys, that the manganese atoms would be divalent, and it would not therefore seem to be legitimate to consider the Heusler phase as belonging to this group of structurally analogous phases. A similar conclusion arises from this study of the Ag–Mn–Al alloys. The direction of the β phase boundary at 650°c (fig. 3) is again consistent with manganese acting as a divalent metal: furthermore, the alloy of composition

Ag_2MnAl does not come within this β phase field, even very close to the solidus at 790°c, and so lends support to this view.

The Ag_3Al (μ) structure, however, shows a different effect. Although of only limited extent at 400°c (fig. 2), the tangential direction of the phase boundaries is consistent with the manganese exerting a valency of zero, and we thus have the example of manganese exerting two different valencies in structures which are both considered to be examples of a 3/2 electron compound.

§ 7. ACKNOWLEDGMENTS

The writer is indebted to many colleagues at the University of Sheffield for their assistance in this investigation: Professor Sucksmith for his continued support and advice; Mr. Hollis for allowing the writer to quote his unpublished magnetic measurements on Ag_5MnAl; and Dr. Crangle for carrying out magnetic measurements on other alloys of this system: Mr. Lawlor, for his help in preliminary studies of the 400°c equilibrium diagram; and Professor Honeycombe for his assistance with the electron microscopy studies.

REFERENCES

BRADLEY, A. J., and ROGERS, J. W., 1934, *Proc. roy. Soc.*, A, **144,** 340.
COLES, B. R., HUME-ROTHERY, W., and MYERS, H. P., 1949, *Proc. roy. Soc.* A, **196,** 125.
GAWRANEK, V., KAMINSKY, E., and KURDJUMOV, G., 1936, *Metallwirtschaft*, **15,** 370.
GEISLER, A. H., 1951, *Trans. Amer. Soc. Metals*, **43,** 90.
HEUSLER, F., 1903, *Verh. dtsch. phys. Ges.*, **5,** 219.
HEUSLER, O., 1928, *Z. anorg. Chem.*, **171,** 126.
HUME-ROTHERY, W., 1948, *Phil. Mag.*, **39,** 89.
KITTEL, C., 1949, *Rev. Mod. Phys.*, **21,** 541.
MEHL, R. F., and BARRETT, C. S., 1931, *Trans. Amer. Inst. min. (metall.) Engrs*, **93,** 78.
MEIKLEJOHN, W. H., 1933, *Rev. mod. Phys.*, **25,** 302.
POTTER, H. H., 1931, *Phil. Mag.*, **12,** 255.
WALKER, C. B. B., and GUINIER, A., 1953, *Acta Met.*, **1,** 568.
WEST, D. R. F., and LLOYD THOMAS, D., 1956, *J. Inst. Met.*, **85,** 97.

The Absorption of Sound in Liquid Helium I under Pressure[†]

By J. A. Newell[‡] and J. Wilks
Clarendon Laboratory, Oxford

[Received February 9, 1959]

Abstract

The absorption of 13·6 Mc/s sound waves has been measured in liquid helium I under pressures of up to 25 atm. The absorption varies considerably with the density of the liquid, but at all temperatures above about 3°K is adequately represented by the classical Stokes–Kirchhoff expression.

§ 1. Introduction

The absorption of sound in a fluid is given by the classical expression due to Stokes (1845) and Kirchhoff (1868) namely

$$\alpha = \frac{2\pi^2 f^2}{\rho v^3}\left[(\lambda + 2\eta) + (\gamma - 1)\frac{K}{C_p}\right] \quad . \quad . \quad . \quad . \quad . \quad (1)$$

where f is the frequency of the sound, v the velocity of sound, ρ the density of the liquid, η the coefficient of shear viscosity, λ the coefficient of dilational viscosity (see for example Wilks (1958)), γ the ratio of the specific heats, K the coefficient of thermal conductivity, and C_p the specific heat at constant pressure. The coefficient λ is not readily identified with any property of the liquid which may be easily measured, but it follows from kinetic theory (Maxwell 1867) that for a perfect gas

$$\lambda = -\tfrac{2}{3}\eta \quad . \quad . \quad . \quad . \quad . \quad . \quad . \quad . \quad . \quad (2)$$

so that (1) becomes

$$\alpha = \frac{2\pi^2 f^2}{\rho v^3}\left[\frac{4}{3}\eta + (\gamma - 1)\frac{K}{C_p}\right]. \quad . \quad . \quad . \quad . \quad . \quad (3)$$

The thermal motion of most liquids is generally more complicated than that of a perfect gas and this results in the absorption being considerably greater (see for example Markham *et al.* (1951)). However, measurements on liquid helium I under the vapour pressure have shown that in the case of this simple liquid the absorption is given by expression (3) (Pellam and Squire 1947). The only other liquids known to behave in a similar way are liquid mercury (Ringo *et al.* 1947), liquid argon, liquid nitrogen and liquid oxygen (Galt 1948). The present paper extends the earlier results on helium I by making measurements with the liquid under pressures of up to 25 atm, so that several of the parameters in eqn. (3) take up considerably different values.

[†] Communicated by the Authors.
[‡] Now at Department of Physics, Institute of Cancer Research, London.

§ 2. THE MEASUREMENTS

The apparatus and methods were similar to those used in experiments on liquid helium II above 1 °K, which we have described previously (Dransfeld *et al.* 1958). The measurements were made at a frequency of 13·6 Mc/s, and the values of the absorption obtained are shown in the figure for various pressures over the liquid. After making due allowance for the difference in frequency these results are in satisfactory agreement with Pellam and Squire's measurements at 15 Mc/s. The second column of table 1 gives

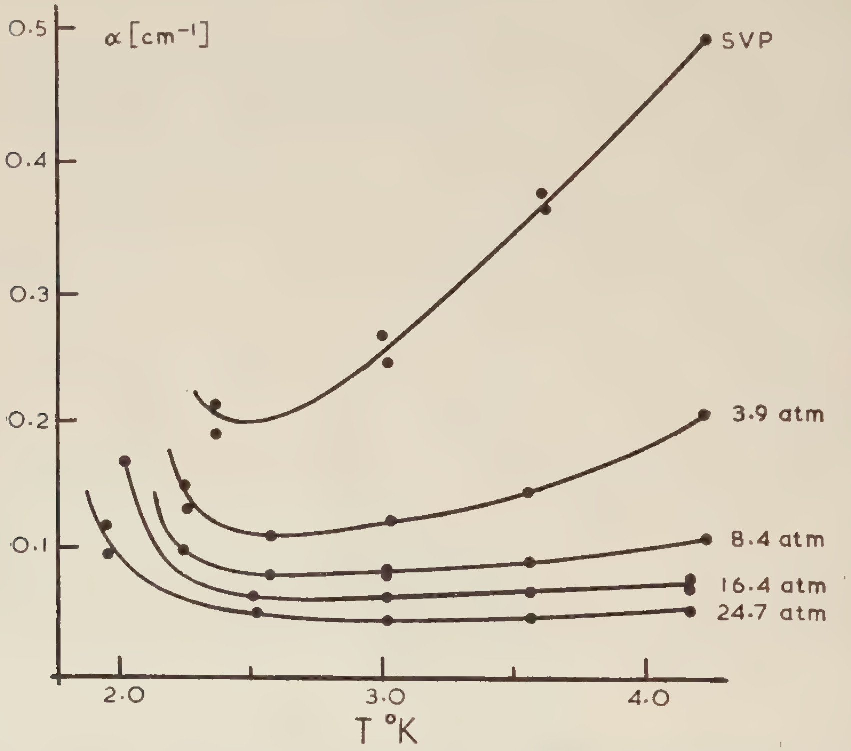

The coefficient of absorption of 13·6 Mc/s sound waves in liquid helium I as a function of the pressure over the helium.

Table 1. The Absorption of Sound in Liquid He I under the Saturated Vapour Pressure

T°K	α (cm^{-1})	α_r $\times 10^6$	$\frac{4}{3}\eta$ $\times 10^6$	$\gamma-1$	$(\gamma-1)K/C_p$ $\times 10^6$	α_r^* $\times 10^6$
4·0	0·43	97	48	0·86	56	104
3·5	0·34	110	49	0·65	50	99
3·0	0·25	102	51	0·38	41	92
2·5	0·20	87	48	0·07	6	54

α is the measured absorption, α_r is the reduced absorption, α_r^* is the reduced absorption calculated from (4) using values given in columns 4, 5 and 6.

smoothed values of the absorption α obtained under the vapour pressure, while the third column gives values of the reduced absorption α_r, obtained by dividing the measured absorption by the factor $2\pi^2 f^2/\rho v^3$. Values of the density have been given by Keesom and Keesom (1933) and of the velocity of sound by Atkins and Stasior (1953). Values of α and α_r at the higher pressures are given in the second and third columns of table 2.

Table 2. The Absorption of Sound in Liquid He I under Pressure

T°K	α (cm^{-1})	α_r $\times 10^6$	$\frac{4}{3}\eta$ $\times 10^6$	$\gamma-1$	$(\gamma-1)K/C_p$ $\times 10^6$	α_r* $\times 10^6$
8·4 atm						
4·0	0·098	84	68	0·36	32	100
3·5	0·087	85	70	0·26	26	96
3·0	0·082	85	72	0·15	19	91
16·4 atm						
4·0	0·071	112	86	0·25	24	110
3·5	0·064	106	89	0·15	17	106
3·0	0·061	102	92	0·10	14	106
24·7 atm						
4·0	0·050	119	102	0·18	18	120
3·5	0·047	114	100	0·10	12	112
3·0	0·046	111	111	0·07	10	121

α is the measured absorption, α_r is the reduced absorption, α_r* is the reduced absorption calculated from (4) using values given in columns 4, 5 and 6.

§ 3. DISCUSSION

It is convenient to re-write eqn. (3) using the reduced absorption α_r, thus

$$\alpha_r = \frac{4}{3}\eta + (\gamma-1)\frac{K}{C_p} . \qquad (4)$$

To compare this expression with the measured absorption under the vapour pressure we use values of η given by Taylor and Dash (1957) and values of K given by Grenier (1951). C_p we take as being approximately equal to the specific heat under the saturated vapour pressure as measured by Hill and Lounasmaa (1957). Values of γ and $(\gamma-1)$ are obtained from the compressibility measurements of Keesom and Keesom (1933) together with the velocity of sound. The fourth, fifth and sixth columns of table 1 give values of the various quantities on the right-hand side of eqn. (4), while the last column gives the calculated values of the reduced absorption (α_r*). At 3°K and above the observed absorption is adequately accounted for by the classical expression, a conclusion previously reached by Pellam and Squire using earlier and less exact data for the various parameters. Any discrepancies are within the errors of the several experimental results used in the comparison. In particular, it is difficult to estimate values of γ accurately for pressures close to the vapour pressure, also the velocity of sound comes into the expression to the third power. Below 3° the absorption is greater than is given by expression (4) and this is certainly due to an additional absorption associated with the lambda transition which does not concern us here. (For further details see Pippard (1951) and Chase (1958).)

The position at higher pressures is shown in table 2. The viscosity at higher densities has been measured by Tjerkstra (1952) and the third column of the table gives his values for $\frac{4}{3}\eta$. On comparing these figures with those for α_r, it is seen that most of the absorption at the higher pressures is due to the viscosity. The experimental data available for evaluating the contribution to the absorption which arises from the thermal conductivity, is rather sparse, and we have to make the best estimate we can. The thermal conductivity under pressure has been measured by Grenier (1951) although only at 4·2°K and up to 3 atm; there was no significant change with pressure. The absorption due to thermal conductivity is also proportional to $(\gamma-1)/C_p$ or to $(\gamma-1)/\gamma C_v$. The only measurements of the specific heat of liquid helium I under pressure are a set of values for C_v corresponding to a pressure of about 19 atm (Keesom and Keesom 1935), and these suggest that to a rough approximation C_v does not vary very much with pressure. Hence if we assume that K and C_v are sensibly constant the reduced absorption at any temperature will be proportional to $(\gamma-1)/\gamma$. Values of $(\gamma-1)$ taken from Atkins and Stasior (1953) are given in column 5 of the table, and estimated values of the thermal contribution to the absorption in column 6. Finally, the last column shows the total estimated reduced absorption (α_r*). Bearing in mind the uncertainties mentioned above which are involved in determining α_r and α_r*, there is reasonable accord between the estimated and observed values of the absorption.

§ 4. CONCLUSION

Above about 3·0°K the absorption of sound in liquid helium I at all pressures up to 25 atm is represented quite well by the Stokes–Kirchhoff expression (3). The large decrease in the absorption at the higher pressures (see figure) arises almost entirely from the large increase in the velocity of sound. Indeed the reduced absorption, α_r, actually increases slightly. Although there is a rapid reduction in the reduced absorption associated with the thermal conductivity, this is more than compensated for by the rise in the viscosity.

It appears that an essential condition for any liquid to have an absorption of the form given by (3) is that its molecules should have only translational modes of motion. Thus the liquids with such an absorption are either monatomic like helium, argon and mercury, or at so low a temperature that their rotational motion is frozen out as in nitrogen and oxygen. Although the Stokes relation, $\lambda = -\frac{2}{3}\eta$, seems to be valid for these liquids it has only been proved for a perfect gas and there is no theoretical basis for applying it to liquids. Helium I under the vapour pressure has an extremely open structure, its viscosity measured at constant volume falls considerably with decreasing temperature (Tjerkstra 1952), and of all liquids approximates most closely to a gas. However, it is not clear that such an approximation is appropriate to other liquids, or even to helium I at the higher densities where the viscosity rises with falling temperature. A theoretical investigation of the value of the coefficient of dilational viscosity of simple liquids and dense gases would therefore be of interest.

Acknowledgments

We wish to express our thanks to the Metropolitan-Vickers Electrical Company for a Research Fellowship (J. W.) and to the Department of Scientific and Industrial Research for a maintenance grant (J. A. N.).

References

Atkins, K. R., and Stasior, R. A., 1953, *Canad. J. Phys.*, **31,** 1156.
Chase, C. E., 1958, *Phys. Fluids*, **1,** 193.
Dransfeld, K., Newell, J. A., and Wilks, J., 1958, *Proc. roy. Soc.* A, **243,** 500.
Galt, J. K., 1948, *J. chem. Phys.*, **16,** 505.
Grenier, C., 1951, *Phys. Rev.*, **83,** 598.
Hill, R. W., and Lounasmaa, O. V., 1957, *Phil. Mag.*, **2,** 143.
Keesom, W. H., and Keesom, A. P., 1933, *Physica*, **1,** 128 ; 1935, *Ibid.*, **2,** 557.
Kirchhoff, G., 1868, *Ann. Phys., Lpz.*, **134,** 177.
Maxwell, J. C., 1867, *Trans. roy. Soc.*, **157,** 49.
Markham, J. J., Beyer, R. T., and Lindsay, R. B., 1951, *Rev. mod. Phys.*, **23,** 353.
Pellam, J. R., and Squire, C. F., 1947, *Phys. Rev.*, **72,** 1245.
Pippard, A. B., 1951, *Phil. Mag.*, **42,** 1209.
Ringo, G. R., Fitzgerald, J. W., and Hundle, B. G., 1947, *Phys. Rev.*, **72,** 87.
Stokes, G. G., 1855, *Trans. Camb. phil. Soc.*, **8,** 287.
Taylor, R. D., and Dash, J. G., 1957, *Phys. Rev.*, **106,** 398.
Tjerkstra, H. H., 1952, *Physica*, **18,** 853.
Wilks, J., 1958, *Z. Phys. Chem.*, **16,** 372.

Remanent Magnetism of Late Secondary and Early Tertiary British Rocks†

By R. L. Wilson
Department of Physics, Imperial College, London

[Received April 6, 1959]

Abstract

The results of palaeomagnetic measurements are given both for the Tertiary basalts of North Eastern Ireland, and for the Cretaceous sediments in the south of England. The direction of magnetization of the basalts is consistently shallower than the present dipole field direction by about 8°. The Cretaceous results are shown to be much less likely to be reliable, but also indicate a shallower dip than that of the present dipole field. A simple and reliable statistical treatment is developed for use with palaeomagnetic data.

§ 1. Introduction

Rock magnetic data for rocks in Britain are completely lacking for the interval between Tertiary and Triassic times, except for a few Jurassic measurements made by Nairn (1937). Since the Triassic results (Clegg *et al.* 1954) show a marked variation from the present dipole field direction while the later Tertiary rocks are magnetized, on the average, in a direction corresponding to that of an axial dipole, it is extremely desirable to gather information concerning intermediate times, in order to ascertain whether any progressive change took place during the interval. The author's work has included two attempts to fill this gap in our knowledge; one was a survey of the Antrim Basalts of Northern Ireland, and the other a series of measurements on Cretaceous sediments from the Isle of Wight. These investigations are described in this paper.

§ 2. The Antrim Basalts

During a survey of the basalts of North Eastern Ireland, the author has measured the palaeomagnetic directions of several igneous bodies. This part of his work constitutes an extension of Hospers and Charlesworth's (1954) work in the same region.

The igneous rocks in this region are of Tertiary age, generally accepted as Eocene, but there exists some evidence, based on a comparison of Scottish and Irish Fossil pollens (Hospers and Charlesworth 1954), that they may have been formed as late as Miocene times. They are basaltic, and may be subdivided into three categories for the purposes of this report; (A) the older 'lower basalts' (olivine), (B) the younger 'middle basalts' (tholeiitic)

---

† Communicated by the Author.

which were previously called 'upper basalts' (Patterson 1955), and (C) the intrusive bodies, dykes and sills, whose relative ages cannot always be determined. Grouping of palaeomagnetic measurements has been made on this basis.

The principle underlying collection of samples was to collect as widely as possible geographically and temporally. The practical limitations of transportation often limited the collection to one sample per igneous body. Ninety samples were collected from fifty-seven distinct igneous bodies, at forty-seven different sites extending around the north-east coast of Ireland from Downhill, in the north-west corner of Co. Antrim, to the dykes exposed east of the Mourne Mountains. Collection was never made more than a few miles inland.

The measuring procedure was to cast each sample of average mass 6 kg, oriented in a rectangular plaster block, and then to measure its direction of magnetization by means of the astatic magnetometer built by Blackett (1952). A core $1\frac{3}{8}$ in. in diameter and $1\frac{3}{8}$ in. long was then cut from the block, and measured under a less sensitive magnetometer as a check on the first measurement.

Table 1 shows the three mean directions derived from the writer's measurements, and the equivalent data from Hospers and Charlesworth's (1954) paper. D is the magnetic declination measured in degrees east of North, I the inclination, $\mathcal{N}$ is the number of separate igneous bodies involved, N is the total number of samples taken from the $\mathcal{N}$ igneous bodies, and n is the total number of independent measurements made (plaster blocks and cores).

It has been customary among rock magnetists to use a form of statistics developed by Fisher (1953). These statistics are based on an assumed Gaussian distribution of density of measured vector directions about the mean direction. In certain cases this distribution is found experimentally to be invalid, so that statistics based on any assumed density distribution must be held in suspicion until the distribution be examined experimentally. In particular, any 'circle of confidence' containing the mean direction with a specified probability may contain falsely implied precision. For this reason a simple system of statistical evaluation of rock magnetic data has been developed (Appendix) and used on the data in this paper. The three significant quantities used are the mean direction, the analogue on a spherical surface of the standard deviation for a single reading, δ, and the standard deviation of the mean, ϵ. These can be found either for a set of igneous bodies, or for a set of measurements on a single igneous body. They are easily understood, and free from any assumptions about distribution.

The measurements for a single igneous body were rejected whenever δ exceeded 10°. The directions were corrected for geological tilt, which in general was small. In cases where only one sample has been taken ($N=1$, $n=2$) from an igneous body, δ has been redefined as the angle between the two directions measured for that sample.

It can be seen from table 1 that the four results are reasonably consistent, all reversed, and that all of them indicate a deviation from the present dipole field of about 8·4° towards shallower inclinations. This is a significant amount in terms of ϵ.

It is necessary to consider the possibility that this deviation might be due to a magnetostrictive effect caused by the pressure of the overlying lavas. The geology of the region indicates that the lowest of the basalts have not been buried more than about 600 metres deep. The pressure at this depth is not great, and similar pressures applied in the laboratory made no discernible directional change. There is no obvious discrepancy between the inclinations of the middle and lower basalts, even though they must have undergone quite different pressures during the geological time involved.

Table 1

	D(ETN)	I	$\mathcal{N}$	N	n	R	δ	ϵ
Lower basalts	173°	−64·6° up	19	35	70	17·599	22°	5·5°
Middle basalts	206°	−62·2° up	6	7	14	5·723	17°	7·1°
Intrusives	184°	−63·3° up	16	25	49	15·268	17°	4·4°
Above three combined	183°	−64·1° up	41	67	133	38·45	20°	3·1°
Hospers' results	194°	−60·2° up	24	72	120	23·253	14°	2·9°
Four results combined	187°	−62·4° up	65	139	253	61·63	18°	2·3°
Present dipole field	0°	+70·8° down	—	—	—	—	—	—
Present field	347°	+70·0° down	—	—	—	—	—	—

(For definitions of symbols, see text.)

On the assumption that the axis of the magnetic dipole field coincides on the average with the earth's rotational axis, the interpretation of this 8·4° deviation as being due to land-mass movement would indicate that Ireland has moved northwards 11·5° of latitude or about 800 miles since the eruption of the basalts.

§ 3. THE ISLE OF WIGHT CRETACEOUS SEDIMENTS

There having been no igneous activity during Cretaceous times in Britain, a systematic attack was made on Cretaceous sediments from eight different localities in Southern England. Forty-six samples were collected from Compton Bay, Whitecliff Bay, Brixton Bay, and Sandown Bay on the Isle of Wight, and from Swanage, Durdle Door, Dungy Head, and Lulworth Cove along the Dorset coast. Each site presented cliff exposures.

Apparent magnetic stability was found in only nineteen of these samples, all of which were collected from the four miles of continuous Wealden sediment exposure along Compton and Brixton Bays. These nineteen samples consisted of buff sandstones and red and grey clays. The other twenty-seven samples were rejected on the basis of the laboratory and geological tests mentioned below. From the nineteen samples, ninety-seven oriented 2 cm cubes were cut and their directions of magnetization determined. The mean intensities were 1×10^{-6} and 5×10^{-6} e.m.u./cm^3 for the sandstones and clays respectively. Table 2 gives the mean direction and standard deviation of the nineteen samples with respect both to the bedding planes and to the present horizontal plane. It also shows the directions of the present earth's field and the dipole field at the Isle of Wight, and the Eocene and Triassic field directions for Britain. Evidence concerning the magnetic stability of these nineteen samples was as follows:

Table 2

	D(ETN)	I(down)	δ	ϵ
Present dipole field	0°	+67·6°	—	—
Present earth's field	351°	+64·0°	—	—
Mean direction with respect to horizontal plane	345°	+63°	4·9°	1·1° ($N=19$)
Mean direction with respect to bedding planes	2°	+59°	8·5°	2·0° ($N=19$)
Reverse of Eocene field direction (for Northern Ireland)	7°	+62°	18·5°	2·3° ($N=65$)
Triassic field direction (for Great Britain)	34°	+26°	—	—

(*a*) The mean direction of magnetization with respect to the present horizontal plane lies only 4° (3·5 standard deviations of the mean) from the direction of the present earth's field.

(*b*) The slight folding of these Wealden beds allowed us to calculate that the 8·5° standard deviation with respect to the bedding planes reduced to 4·9° with respect to the horizontal plane. This conforms with Graham's (1949) test of stability for folded strata.

(*c*) Alternating field demagnetization of the sandstones, in zero steady field, revealed a soft magnetic component, which disappeared for peak alternating fields less than 180 oersteds and had an initial magnitude which was small compared with a harder component. This harder component remained constant in magnitude and direction until 180 peak oersteds was reached, where it began to be unpredictably affected. Removal of the soft component improved the agreement between measurements on cubes from any one sample.

(*d*) Measurement of the magnetic moment of sandstone cubes suitably oriented in the earth's field revealed a soft component, which grew exponentially with time, and was small in magnitude with respect to a harder component. The harder component was stable over at least several months.

(*e*) Two superficially different types of rock, with different natural intensities, comprised the nineteen samples.

The fact that the mean direction of magnetization is roughly intermediate between the Eocene and Triassic directions cannot be taken as proof of stability. Test (*a*) admits the possibility of the harder component possessing instability over a time greater than several months, but small with respect to the times involved in secular variations. It could, on the other hand, be a chance result of the particular tilt of these Wealden beds. Test (*b*) indicates instability of the harder component. Tests (*c*) and (*d*) reveal only that relatively soft and hard components do exist, and tell us nothing of magnetic stability over geological times, except that the alternating field test is consistent with the interpretation of the harder component as being thermoremanence in magnetite, following the work of Thellier and Rimbert (1955). Fact (*e*) is circumstantial evidence in favour of stability.

There is, therefore, doubt as to the validity of any palaeomagnetic interpretation of these results, and further work, preferably on similar sediments differently tilted, must be done to establish a conclusive result.

ACKNOWLEDGMENTS

The author is pleased to thank Professor P. M. S. Blackett, Dr. J. A. Clegg, and members of the Imperial College Rock Magnetism Group for advice and help with this work.

REFERENCES

BLACKETT, P. M. S., 1952, *Phil. Trans.*, **245,** 309.
CLEGG, J. A., ALMOND, M., and STUBBS, P. H. S., 1954, *Phil. Mag.*, **45,** 583.
FISHER, R. A., 1953, *Proc. roy. Soc.* A, **217,** 295.
GRAHAM, J. W., 1949, *J. Geophys. Res.*, **54,** 137, 67.
HOSPERS, J., and CHARLESWORTH, H. A. K., 1954, *Mon. Not. R. astr. Soc. geophys. Suppl.*, **7,** 1, 32.
NAIRN, A. E. M., 1957, *Mon. Not. R. astr. Soc. geophys. Suppl.*, **7,** 6, 308.
PATTERSON, 1955, *Proc. roy. Irish Acad.* B, **57,** 7.
THELLIER, E., and RIMBERT, F., 1955, *C.R. Acad. Sci., Paris*, **240,** 1404.

APPENDIX

A statistical system has been used which employs the analogues, in the case of distribution of points on a spherical surface, of the standard deviations used for a distribution of points on a plane.

(*a*) The mean direction of N directions is found in the customary way. If λ, μ, ν be the direction cosines of the mean direction and λ_i, μ_i, ν_i the direction cosines of the N measured directions, then λ, μ, ν are defined as

$$\lambda=\sum\lambda_i/R, \quad \mu=\sum\mu_i/R, \quad \nu=\sum\nu_i/R$$

where $$R\equiv\sqrt{\{(\sum\lambda_i)^2+(\sum\mu_i)^2+(\sum\nu_i)^2\}}.$$

That is, the mean direction cosines define the mean direction.

(*b*) The mean cosine of the deviations δ_i from the mean direction is found in order to establish the standard deviation for a single reading.

$$\overline{\cos\delta}=\frac{\sum\cos\delta_i}{N}=\frac{\sum\lambda_i\lambda+\sum\mu_i\mu+\sum\nu_i\nu}{N}=\frac{R}{N}$$

whence the deviation $$\delta=\cos^{-1}(R/N).$$

This is the analogue of the 'standard' or r.m.s. deviation, since for small δ

$$\overline{\cos\delta}\doteqdot 1-\tfrac{1}{2}\overline{\delta^2}=R/N.$$

This gives the r.m.s. deviation $\delta_{\text{r.m.s.}}\doteqdot\sqrt{\{2(N-R)/N\}}$.

(*c*) Then by analogy with the case of a planar distribution the standard deviation of the mean direction, ϵ, may be taken as

$$\epsilon=\delta/\sqrt{N}.$$

The expressions δ and ϵ are simple to use and understand, and express the facts adequately without recourse to assumptions about distribution of vector densities. They are also free of mathematical approximations which might limit their region of usefulness.

The Helium Film formed from the Vapour Phase†

By L. G. GRIMES‡ and L. C. JACKSON§
H. H. Wills Physical Laboratory, University of Bristol

[Received February 12, 1959]

ABSTRACT

An account is given of an experiment in which the thickness of the ' saturated ' helium film formed from the vapour on a stainless steel mirror was compared with the thickness of the film formed from the liquid phase. The thickness of the film formed from the vapour was almost the same above and below the λ-point and of the same thickness as the helium I film formed when the mirror was in contact with the liquid. The thickness of the helium II film, with the mirror in contact with the liquid, was much thicker because of the more stringent isothermal conditions prevailing on the mirror surface.

§ 1. INTRODUCTION

FRENKEL (1940) and Schiff (1941) have suggested that the formation of the helium film is essentially due to the van der Waals adsorption forces between the helium atoms and those of the substrate. Minimizing the sum of the van der Waals potential energy and the gravitational energy of an atom at the surface of the film leads to the following equation for the film profile:

$$d = k/H^{1/3}$$

where k is a constant and d the thickness of the film at a height H. This equation has been derived in another way by Rice and Widom (1953) and independently by Atkins (1954) and Meyer (1955). They consider the helium film as an adsorbed layer in equilibrium with a very slightly unsaturated vapour. An interesting feature of this idea is the suggestion that the profile and thickness of the ' saturated ' film should, for the strictly isothermal case, be the same whether the substrate is in contact with the bulk liquid or not, apart from effects due to curvature at the edges of the substrate (Meyer 1955). The purpose of the work described in this paper was to compare qualitatively the thickness of the film formed from the vapour with that formed when the mirror was in contact with the liquid surface.

Due to the mobile helium II film it was essential, if the present experiment was to provide unambiguous results, to measure the thickness of a film formed on a surface which had no mechanical contact with the bath liquid or the film arising from it. To achieve this requirement a mirror was suspended in the vapour phase from a small cylindrical magnet which floated above a superconducting lead dish. One advantage of such a system is that the heat input to the surface is limited to radiation only. The disadvantage is that, at temperatures below the λ-point, the surface is only strictly 'isothermal' with the bath temperature when the mirror is in contact with the liquid bath.

---

† Communicated by the Authors.

‡ Present address: Physics Department, University of Pennsylvania.

§ Present address: Royal Military College, Kingston, Ontario.

For an account of the various theories of the film and the results for the film thickness obtained by many authors, the reader is referred to the review article by Jackson and Grimes (1958).

§ 2. The Apparatus and Method

The apparatus used was essentially the same as that described in an earlier paper (Ham and Jackson 1957: see also Grimes and Jackson, to be published shortly in the *Philosophical Magazine*, referred to as paper II). The only essential difference between the present arrangement and that described in paper II is in the design of the experimental chamber (the mirror tube); this is shown in fig. 1. The lead dish C rested on the glass rim of the mirror tube and had a small hole through its centre. A copper tube T was attached to the lead dish and made central in the mirror tube by suitably spaced phosphor bronze strips. The upper part of the mirror tube terminated in a kovar-glass seal S and this was joined by Hoyt metal to a kovar cap K. This was joined to a length of german silver tubing D which suspended the mirror tube in the cryostat and also served as a connecting line to the reservoirs of helium gas which was condensed during an experiment into the mirror tube. The small permanent magnet M was supported on a brass stirrup which was connected to the top of the Dewar vessel by a length of german silver tubing coaxial with D. The Dewar head was designed to provide a means of rotating and lowering or raising the magnet to any desired position in a vacuum of 10^{-7} mm Hg. The stainless steel mirror G was 1 cm long, 4 mm wide and 2 mm thick and was suspended from the magnet by a thin tungsten rod R.

The pre-run treatment and method of collecting helium gas from the surface of the liquid in the cryostat and condensing it into the mirror tube was similar to that described in Ham and Jackson (1957) and paper II. The principles of the optical method used for the measurements have been described in previous papers (Burge and Jackson 1951, Ham and Jackson 1957) and will not be described here.

Because of the poor thermal contact between the contents of the mirror tube and the liquid helium bath it was necessary to have a slight pressure of helium gas in the mirror tube during the cooling period, prior to transferring liquid helium into the cryostat. The resulting pressure at the liquid helium temperature was always between 30 and 60% of the saturated vapour pressure. The nicol positions for intensity matching across the 1/3 boundary of the barium stearate layers on the mirror were taken under these conditions and used as the zero position of the apparatus; due allowance was made for the birefringence effects in the glass of the mirror tube caused by the pressure difference across the glass surfaces. This procedure was considered justifiable as an experiment of Bowers (1953) showed that about two or three helium layers are adsorbed under the above saturations and this is equivalent to a nicol change of about 3 min of arc.

Fig. 1

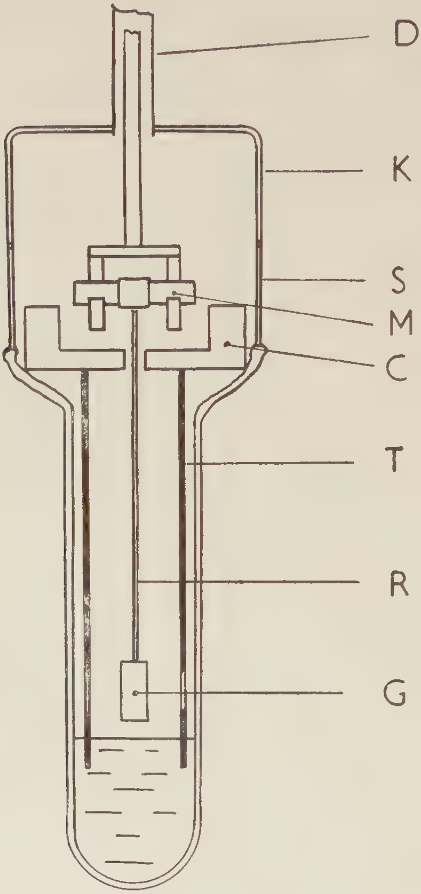

The mirror tube.

The magnet, during the cooling of the apparatus, was suspended by the brass stirrup well above the lead dish. Following the transfer of liquid helium into the apparatus the stirrup was lowered slowly until the magnet released itself and then lowered to the bottom of the lead dish. Floating the magnet in the above manner always gave stable floating positions and the frozen-in currents in the superconducting lead dish probably helped to stabilize the magnet. The floating position of the magnet was not exactly reproducible and the zero position varied from experiment to experiment; this was not a disadvantage, however, for the present purpose.

The temperature was determined by measuring the vapour pressure of the liquid on either an oil or mercury manometer and using the T_{L55} vapour pressure tables (van Dijk and Durieux 1958).

§ 3. THE EXPERIMENTS WITH THE FLOATING MAGNET

At a temperature of 2·05°K, $\frac{1}{2}$ litre of helium gas was condensed slowly into the mirror tube. The magnet remained stable and the initial nicol measurements indicated that a thick film was present on the mirror. It was first thought that the helium gas supply contained an impurity sufficient to affect the film thickness but later measurements showed that the initial matching position of 68° 36′ had changed to 67° 16′ and remained constant at this value. Subsequent condensations indicated that the initial high reading of 68° 36′ was due to a drop of liquid helium remaining on the bottom of the mirror. During later condensations the drop remaining on the mirror surface was evaporated by switching on the room lights: thickness measurements (nicol readings) were made after sufficient time had elapsed for the attainment of temperature equilibrium. After each condensation the position of the liquid level relative to the bottom of the mirror was recorded. The results indicated that the thickness of the film formed from the vapour phase remained practically independent of the position of the liquid surface. Condensations were continued until the liquid reached the mirror surface and immediately large nicol readings were obtained which indicated the presence of a much thicker film on the mirror surface. At a height of 0·06 cm the nicol reading was 69° 0′. The temperature was then allowed to rise through the λ-point to a temperature of 2·48°K. When temperature equilibrium had been attained the nicol readings were recorded and the mean value was similar to those obtained when the mirror was in the vapour phase at a temperature below the λ-point. A second experiment was carried out at 2·03°K and similar results were obtained; in the vapour phase the thickness was practically independent of the position of the liquid helium level until the latter reached the mirror surface when the thick helium II film formed. After the completion of this experiment the temperature was raised to 2·45°K and the mean nicol reading was again similar to that obtained when the mirror was in the vapour phase at 2·03°K.

Two experiments were carried out at a temperature of 2·47°K. The times required for the attainment of temperature equilibrium were much longer but the experimental procedure was as described above. The results were very similar to those obtained at temperatures below the λ-point. The only important difference was that the thickness of the film formed on the mirror, when the liquid was in contact with the mirror was practically the same as that obtained when the mirror was in the vapour phase.

As the magnet floated in slightly different positions during each experiment the results have been normalized to the results at 2·47°K, so that all the nicol positions agree at a height of 3 cm. These normalized results are plotted in fig. 2. The sensitivity of the apparatus was not determined directly but estimated using the thickness measurements of Ham and Jackson (1957) for the height range 0 to 2·5 cm, at temperatures below the λ-point. The estimates of the film thickness are therefore somewhat approximate, but the results show clearly that a film forms the vapour phase at temperatures above and below the λ-point and has a thickness similar to a helium I film formed on a surface which is in direct contact with the liquid helium.

Fig. 2

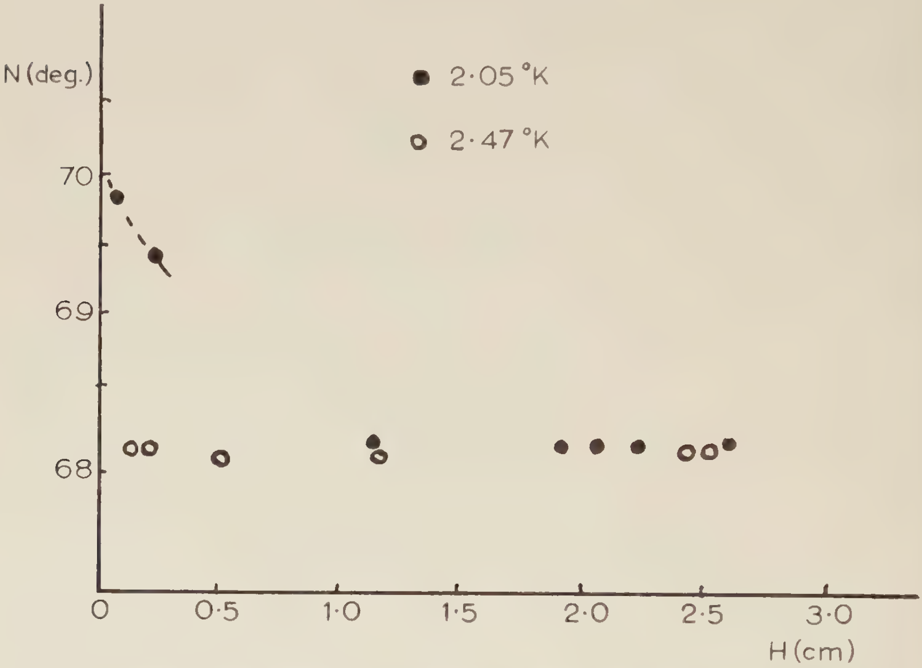

The thickness of the helium film formed (*a*) from the vapour phase (above 0·3 cm) ; (*b*) from the liquid phase (below 0·3 cm).

§ 4. Discussion

The apparent discontinuity in the curve of nicol positions against height when the level of helium liquid reaches the mirror, obtained at temperatures below the λ-point, seems to lend support to the idea that the presence of the helium film has something to do with the λ-point phenomenon of the bulk liquid. This would only be true if the temperature of the mirror surface, when in the vapour phase, was the same as that of the bath liquid. However, observations showed that the mirror was at a slightly higher temperature than the bulk liquid and this alters the interpretation of the results. Part of the energy of the light beam is absorbed at the surface of the mirror.

Further evidence of this heat input was obtained at temperatures above the λ-point when the mirror was in direct contact with the bulk liquid He I. A fine stream of bubbles of helium gas was observed to rise from a small hole in the bottom of the mirror. From an estimate of the size of the bubbles and their rate of formation the heat flowing to the liquid through the bottom of the mirror was estimated to be of the order of 10^{-6} cals/sec. As the surface area of the mirror was of the order of 10 times that of the bottom of the mirror a nearer estimate of the total heat input would probably be 10^{-5} cals/sec.

Fig. 3

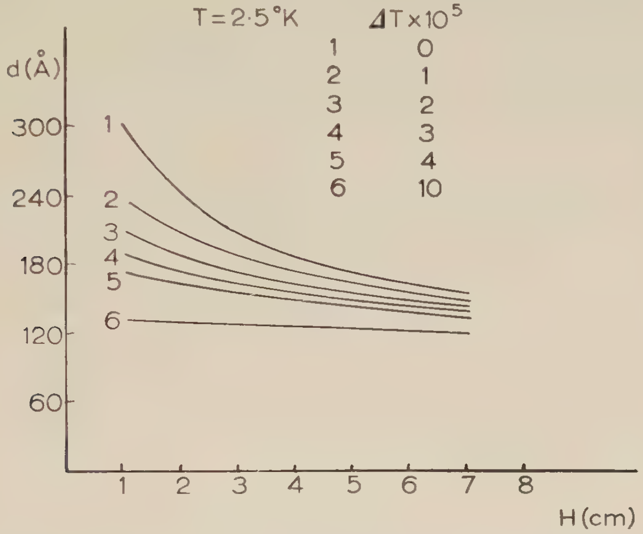

The effect of ΔT on the thickness of the helium film.

When the mirror is surrounded by the vapour phase the heat absorbed at the surface is removed through the vapour phase (see paper II): the average energy of an atom leaving the film is $3/2\ k\Delta T$ greater than a helium atom entering the film. This temperature difference ΔT is present at all temperatures when the mirror is in the vapour phase and is also present when the mirror is in contact with the liquid helium at temperatures above the λ-point. At temperatures below the λ-point, when the mirror makes contact with the bulk liquid, the superfluid destroys any ΔT present and the film is effectively at the same temperature as the liquid helium bath. The presence of a ΔT on the mirror produces drastic effects on the helium film profile and has been described fully by Ham and Jackson (1957) and Jackson and Grimes (1958). Under this condition the thickness measured at a height H becomes equal to the thickness of the ideal isothermal film at a height $(H+\Delta H)$ where ΔH is proportional to ΔT. The effect of ΔT on the film thickness is shown in fig. 3 at a temperature of 2·5°K. The values of ΔH which fit the estimated results for the thickness of the helium I film are in the range 100 to 200 and the corresponding values of ΔT at 2·5°K are between 10^{-3} and 2×10^{-3} deg K. The value of ΔT calculated from the results of paper II was 10^{-4} deg K. As the mass and surface area of the present mirror are very much smaller than that of the mirror used in paper II the temperature excess is expected to be greater for the present mirror.

As the ΔT exists at the helium II temperatures when the mirror is in the vapour phase we should expect the thickness of the helium II film to be approximately equal to the helium I film: this is in agreement with the results. This would not be the case when the superfluid helium came in contact with the mirror. One would expect the temperature difference to be somewhat greater when the mirror is in the vapour phase than when it is dipping into the liquid He I and anticipate, as a result, a small discontinuity in the helium I results when the liquid level reaches the mirror. The scatter of the results prevented the resolution of this discontinuity if present.

Finally it may be concluded that if the thickness of the helium I film could be measured under isothermal conditions, the resulting thickness would be of the order of that of the helium II film. Whether it would be thicker than the helium II film just above the λ-point, as Franchetti (1957) suggests cannot be established from the present observations. The results are in qualitative agreement with the earlier results of Ham and Jackson (1957) and Grimes and Jackson (to be published) and indicate the correctness of the theories of the helium film which are based primarily on the van der Waals attraction.

REFERENCES

ATKINS, K. R., 1954, *Canad. J. Phys.*, **32,** 347.
BOWERS, R., 1953, *Phil. Mag.*, **44,** 485.
BURGE, E. J., and JACKSON, L. C., 1951, *Proc. roy. Soc.* A, **205,** 270.
FRANCHETTI, S., 1957, *Nuovo Cim.*, **5,** 1266.
FRENKEL, J., 1940, *J. Phys., Moscow,* **2,** 365.
HAM, A. C., and JACKSON, L. C., 1957, *Proc. roy. Soc.* A, **240,** 243.
JACKSON, L. C., and GRIMES, L. G., 1958, *Advanc. Phys.*, **7,** 435.
MEYER, L., 1955, *Phys. Rev.*, **97,** 22.
RICE, O. K., and WIDOM, B., 1953, *Phys. Rev.*, **90,** 987.
SCHIFF, L., 1941, *Phys. Rev.*, **59,** 839.
VAN DIJK, H., and DURIEUX, M., 1958, *Leiden Comm. Suppl.* No. 113c.

The Propagation of Fading Waves†

By R. P. Mercier
The Cavendish Laboratory, Cambridge

[Received December 5, 1958]

Abstract

A scalar wave with random variations of amplitude and phase across the wave-front is assumed as a simple model of a radio wave after it has left the ionosphere. The second-order moments of the in-phase and quadrature components of the fluctuating part of the field are found using the Fresnel diffraction formula. It is assumed that these two components have a joint Gaussian distribution, and a parameter ρ_N, called the intrinsic correlation of the fading, is introduced ; this serves as a measure of the eccentricity of the ellipse of constant probability. It is shown that ρ_N is the amplitude of the diffraction pattern produced by a distribution of intensity proportional to the spatial correlation function of the fluctuations over the wave-front. As the wave propagates the correlation tends to zero. It is shown that for a given irregularity size and wavelength, the irregularities may be supposed to be situated at any height, up to a certain maximum height, at which $\rho_N=1$. An analysis of day time fading on 16 kc/s has been made. It appears that the intrinsic correlation of the wave at the ionosphere is very near one, and that the ionosphere imposes phase modulation on the wave.

1. Introduction

The application of the theories of statistics and random noise in radio propagation has progressed steadily since the paper by Ratcliffe (1948) where it was first suggested that a fading radio signal was essentially the same as electrical noise that has been passed through a narrow-band filter. The two well-known papers by Rice (1944) are devoted to the study of electrical noise in circuits. In such theories of electrical noise and fading, the random part of the radio frequency current is assumed to be randomly phased (i.e. that the phase is uniformly distributed from 0 to 2π), and it is necessary to consider only its average power spectrum. Now when one considers thermal noise or thermal radiation, which originates in the independent motion of a collection of electrons, it is clear that the total current or electric field is randomly phased. However, the fading of a radio wave is quite different in this respect ; for the initial source is the coherent radiation of a transmitter, certain modifications in amplitude and phase being introduced by the ionosphere when it is not perfectly specular. It is not obvious that the wave is randomly phased in this case.

It is the purpose of the present paper to examine in detail how the wave becomes randomly phased as it propagates away from the ionosphere.

---

† Communicated by the Author.

It will be shown how one may infer from the statistics of amplitude and phase at the receiver the sort of modulation that was imposed on the reflected wave and the size of the irregularities in the ionosphere. It is usual to measure the irregularity size by correlating the fading at two spaced receivers. In the present method the signals which are correlated are from the same receiver but have a $\pi/2$ difference of phase.

In two recent publications Bowhill (1956, 1957) calculated the statistical properties of a fading signal. His results are similar to those given in § 2 of this paper, but his derivation was based on the theory of the angular spectrum. The present method using Fresnel's diffraction formula is rather simpler.

Further information about the diffracted signal is obtained by assuming that the in-phase and quadrature-components of the signal have a joint Gaussian distribution. Instead of Bowhill's correlation of amplitude and phase we shall define a parameter called the intrinsic correlation of the fading signal. It will be shown that this parameter is related to the diffraction pattern due to a single irregularity, so that it is then possible to give a simple physical interpretation of the changes in the signal as it propagates.

2. Diffraction Theory

We have to consider the propagation of a plane wave after it has been modified by irregularities which alter its phase and amplitude. In the following work the Fresnel approximation is used in calculating the signal at the receiver. The complex amplitude is assumed known over an infinite plane, the direction of propagation being normal to this plane. The xy plane, which is called the screen, contains the known amplitude field. The receiver is at (x_1, y_1, z) and the propagation is in the $+z$ direction. We shall later substitute a wave diverging from a point source for the plane wave.

Fresnel's diffraction formula (Baker and Copson 1950), valid for $r \gg \lambda$, is

$$E(x_1, y_1, z) = \frac{i}{2} \int\int_{x,\,y=-\infty}^{x,\,y=\infty} F(x, y) \exp\left(i\omega t - \frac{2\pi i r}{\lambda}\right) \frac{1+\cos\psi}{\lambda r}\, dx\, dy \qquad (1)$$

where $r = \sqrt{[z^2 + (x-x_1)^2 + (y-y_1)^2]}$, ψ = angle between the direction of propagation and the line joining (x, y) and (x_1, y_1, z). λ = wavelength, ω = angular frequency $= 2\pi c/\lambda$, F = the complex amplitude of the wave at the screen, $\equiv F_1(x, y) + iF_1(x, y)$.

We shall assume that the variation in the angle of arrival of the diffracted radiation is small enough that one may use the expansion of r in terms of $(x-x_1)^2$, $(y-y_1)^2$, which is an approximation used by Fresnel. Since the width of the angular spectrum is determined by the gradient of phase of F over the screen, there is a certain restriction on this. For example, if the period of phase fluctuation over the screen is one wavelength, the amplitude of the periodic variation should not exceed one radian. It may in fact be shown that any field in the screen of shorter spatial period gives field rise only to evanescent waves which disappear within a few wavelengths of the screen (Booker and Clemmow 1950). We have therefore

$$E(x_1, y_1, z) = \frac{i}{\lambda z} \int\int_{-\infty\,-\infty}^{\infty\,\infty} F(x, y) \exp\left(\frac{-\pi i}{\lambda z} [(x-x_1)^2 + (y-y_1)^2]\right) dx\, dy$$

$$\times \exp\left(i\omega t - \frac{2\pi i z}{\lambda}\right)$$

$$\equiv [E_1(x_1, y_1, z) + iE_2(x_1, y_1, z)] \exp\left(i\omega t - \frac{2\pi i z}{\lambda}\right). \quad . \quad . \quad (2)$$

The quantities F_1, E_1 and F_2, E_2 are respectively the amplitudes of the in-phase and quadrature components of the signal. These are equivalent to the amplitude and phase, but are much easier to discuss in the analysis. We wish to make applications to experimental work in which both phase and amplitude are recorded, and not amplitude alone.

This is the same diffraction formula that has been used by Booker *et al.* (1950), Ratcliffe (1948), and Bowhill (1956). They derived it from an exact diffraction theory based on the concept of the angular spectrum of the diffracted radiation (Booker and Clemmow 1950). Hewish (1951) has made the exact calculation in a case of a periodic screen where the period of the phase variation was 50 λ with an amplitude of up to 4 radians; the angular spectrum was narrow enough that the Fresnel approximation might have been used.

In order to study the statistical properties of E and F when the ionosphere is irregular, we consider a hypothetical assembly of screens—the parent population in the usual terminology of statistics. Averages will be with respect to this population. In practice one samples by taking a record of fading at the receiver for as long as the fading remains statistically stationary in time, so that the sample is homogeneous. We denote by a bar over a quantity its assembly average. We shall use (2) to find the following quantities

$$\overline{E_1}, \overline{E_2}, \overline{E_1^2}, \overline{E_1 E_2}, \overline{E_2^2}. \quad . \quad . \quad . \quad . \quad . \quad . \quad . \quad . \quad (3)$$

We assume that $F(x, y)$ is a stationary function over the entire xy plane. The probability distributions of E and F are discussed later.

The following results are taken without proof

$$\int\int_{-\infty\,-\infty}^{\infty\,\infty} \exp\left(i[a(x^2+y^2)+bx+cy+d]\right) dx\, dy = \frac{\pi i}{a} \exp\left(i\left[d - \frac{b^2+c^2}{4a}\right]\right), \quad . \quad . \quad . \quad (4)$$

$$\lambda^2 z^2 \int\int_{-\infty\,-\infty}^{\infty\,\infty} \exp\left(\frac{2\pi i}{\lambda z}(x\xi + y\eta)\right) dx\, dy = \delta(\xi, \eta). \quad . \quad . \quad (5)$$

where a, b, c, d are real, and $\delta(\xi, \eta)$ is the Dirac delta function. (4) may be derived from the Fresnel integral

$$\int_0^\infty \exp(ix^2)\, dx = \tfrac{1}{2}(1+i)\sqrt{\pi/2}.$$

The average of E, $\bar{E}$, is obtained from (2), dropping the

$$\exp\left(-\frac{2\pi iz}{\lambda}+i\omega t\right)$$

$$\bar{E}=\frac{i\bar{F}}{\lambda z}\int\int_{-\infty-\infty}^{\infty\infty}\exp\left(-\frac{\pi i}{\lambda z}[(x-x_1)^2+(y-y_1)^2]\right)dx\,dy=\bar{F}. \qquad (6)$$

Thus the average signal remains unchanged in course of propagation.

We shall now find $\overline{E^2}$ and $\overline{EE^*}$ from which one finds $\overline{E_1{}^2}$, etc. The square of the right-hand side of (2) is expressed as a double integral,

$$\overline{E^2}=-\frac{1}{\lambda^2z^2}\int\int\int\int_{-\infty-\infty-\infty-\infty}^{\infty\infty\infty\infty}\overline{F(x,y)F(x',y')}\exp\left(\frac{-\pi i}{\lambda z}\right.$$
$$\left.\times\{(x-x_1)^2+(y-y_1)^2+(x'-x_1)^2+(y'-y_1)^2\}\right)dx\,dy\,dx'\,dy'.$$

Write $x'=x+\xi$, $y'=y+\eta$. Since F is a stationary random function $\overline{F(x,y)F(x+\xi,y+\eta)}$ is a function of ξ, η only. The x and y integration may be performed using (4):

$$\overline{E(x_1,y_1)^2}=\frac{i}{2\lambda z}\int\int_{-\infty-\infty}^{\infty\infty}\overline{F(x,y)F(x+\xi,y+\eta)}\exp\left[\frac{-\pi i(\xi^2+\eta^2)}{2\lambda z}\right]d\xi\,d\eta. \qquad (7)$$

$\overline{E^2}$ is therefore independent of (x_1, y_1) and E is a stationary random function.

$\overline{EE^*}$ is also expressed as a double integral:

$$\overline{EE^*}=\frac{1}{\lambda^2z^2}\int\int\int\int_{-\infty-\infty-\infty-\infty}^{\infty\infty\infty\infty}\overline{F(x,y)F^*(x',y')}\exp\left(\frac{\pi i}{\lambda z}\right.$$
$$\left.\times\{-(x-x_1)^2+(x'-x_1)^2-(y-y_1)^2+(y'-y_1)^2\}\right)dx\,dy\,dx'\,dy',$$

$$\overline{EE^*}=\frac{1}{\lambda^2z^2}\int\int\int\int_{-\infty-\infty-\infty-\infty}^{\infty\infty\infty\infty}\overline{F(x,y)F^*(x+\xi,y+\eta)}\exp\left(\frac{\pi i}{\lambda z}\right.$$
$$\left.\times\{-2x\xi-2y\eta\}\right)dx\,dy\,d\xi\,d\eta$$
$$=\int\int_{-\infty-\infty}^{\infty\infty}\overline{F(x,y)F^*(x+\xi,y+\eta)}\delta(\xi,\eta)\,d\xi\,d\eta$$

$$\overline{EE^*}=\overline{FF^*},\quad \text{i.e.}\quad \overline{E_1{}^2}+\overline{E_2{}^2}=\overline{F_1{}^2}+\overline{F_2{}^2}. \qquad (8)$$

The average power is conserved during the propagation. From (7), (8) we may find the averages $\overline{E_1{}^2}$, $\overline{E_2{}^2}$, $\overline{E_1E_2}$:

$$\overline{E_1{}^2}=\tfrac{1}{4}\overline{(E+E^*)^2}=\tfrac{1}{4}(\overline{E^2}+\overline{E^{2*}}+2\overline{EE^*}),$$
$$\overline{E_2{}^2}=-\tfrac{1}{4}\overline{(E-E^*)^2}=-\tfrac{1}{4}(\overline{E^2}+\overline{E^{2*}}-2\overline{EE^*}),$$
$$\overline{E_1E_2}=\frac{1}{4i}\overline{(E+E^*)(E-E^*)}=\frac{1}{4i}(\overline{E^2}-\overline{E^{2*}}).$$

The spatial correlation functions of F_1 and F_2 are defined as follows:

$$\rho_1(\xi,\eta)=\frac{\overline{F_1(x,y)F_1(x+\xi,y+\eta)}-\bar{F}_1{}^2}{\overline{F_1{}^2}-\bar{F}_1{}^2},\qquad \rho_2(\xi,\eta)=\frac{\overline{F_2(x,y)F_2(x+\xi,y+\eta)}-\bar{F}_2{}^2}{\overline{F_2{}^2}-\bar{F}_2{}^2},$$

$$\rho_{12}(\xi,\eta)=\frac{\overline{F_1(x,y)F_2(x+\xi,y+\eta)}-\bar{F}_1\bar{F}_2}{\overline{F_1F_2}-\bar{F}_1\bar{F}_2}. \qquad (9)$$

It is assumed that $\rho_1, \rho_2, \rho_{12} \to 0$ as $\xi, n \to \infty$. Clearly $\rho_1 = \rho_2 = \rho_{12} = 1$ at $\xi = \eta = 0$.

For brevity the integrals occurring in (7) when the spatial correlation functions are substituted, are denoted as follows:

$$\left.\begin{aligned} B_1 + iA_1 &= \frac{1}{2\lambda z} \int\int_{-\infty-\infty}^{\infty\,\infty} \rho_1(\xi, \eta) \exp\left(\frac{-\pi i}{2\lambda z}(\xi^2+\eta^2)\right) d\xi\, d\eta, \\ B_2 + iA_2 &= \frac{1}{2\lambda z} \int\int_{-\infty-\infty}^{\infty\,\infty} \rho_2(\xi, \eta) \exp\left(\frac{-\pi i}{2\lambda z}(\xi^2+\eta^2)\right) d\xi\, d\eta, \\ B_{12} + iA_{12} &= \frac{1}{2\lambda z} \int\int_{-\infty-\infty}^{\infty\,\infty} \rho_{12}(\xi, \eta) \exp\left(\frac{-\pi i}{2\lambda z}(\xi^2+\eta^2)\right) d\xi\, d\eta. \end{aligned}\right\} \quad (10)$$

The final result giving the averages and variances of E_1, E_2 are obtained from (7)–(10):

$$\begin{aligned} &\overline{E_1} = \overline{F_1}, \quad \overline{E_2} = \overline{F_2}, \\ &\overline{E_1^2} - \overline{E_1}^2 = \tfrac{1}{2}(\overline{F_1^2} - \overline{F_1}^2)(1 - A_1) + \tfrac{1}{2}(\overline{F_2^2} - \overline{F_2}^2)(1 + A_2) - (\overline{F_1F_2} - \overline{F_1}\,\overline{F_2})B_{12}, \\ &\overline{E_2^2} - \overline{E_2}^2 = \tfrac{1}{2}(\overline{F_1^2} - \overline{F_1}^2)(1 + A_1) + \tfrac{1}{2}(\overline{F_2^2} - \overline{F_2}^2)(1 - A_2) + (\overline{F_1F_2} - \overline{F_1}\,\overline{F_2})B_{12}, \\ &\overline{E_1E_2} - \overline{E_1}\,\overline{E_2} = \tfrac{1}{2}(\overline{F_1^2} - \overline{F_1}^2)B_1 - \tfrac{1}{2}(\overline{F_2^2} - \overline{F_2}^2)B_2 - (\overline{F_1F_2} - \overline{F_1}\,\overline{F_2})A_{12}. \end{aligned} \quad . \; . \; . \; (11)$$

As an example let the correlation functions be identical and of the form

$$\rho_1 = \rho_2 = \rho_{12} = \exp\left[-\frac{1}{r_0^2}(\xi^2+\eta^2)\right]. \quad . \; . \; . \; . \; . \; (12)$$

Then we have

$$A_1 = A_2 = A_{12} = -\frac{x^2}{1+x^2}, \quad B_1 = B_2 = B_{12} = \frac{x}{1+x^2}$$

where

$$x = \pi r_0^2 / 2\lambda z.$$

This example will be discussed in § 3.

2.1. *Point Source*

As nothing has been said about what happens to the wave in the ionosphere, we cannot state generally what happens when the source is brought to a finite distance. Despite conflicting theories of the details of the scattering it has been customary to assume that the function $F(x, y)$ is modified as follows for a point source:

$$F(x, y) = \{F_1(x, y) + iF_2(x, y)\}\frac{a}{r_1}\exp\left(i\omega t - \frac{2\pi i r_1}{\lambda}\right) \quad . \; . \; (13)$$

where r_1 is the distance from some source on the $-z$ axis at $(z_1, 0)$ to the point (x, y). $a =$ some constant.

This is true only when the scattering occurs mainly in a region where the refractive index μ is $\gtrsim 1$. If there is appreciable scattering near the level of reflection—analogous to deviative absorption—then the modulation F just below the ionosphere will depend on the detailed boundary conditions within the ionosphere (height gradient of electron density, etc.). It is a mistake to assume always, for example, that the diffraction pattern on the ground is doubled in size when a point source is substituted for an incident plane wave. What follows therefore is correct only for a model of the ionosphere in which the scattering occurs in a region where $\mu \approx 1$.

We shall neglect the variation in intensity of illumination over the screen, and consider only the phase variation. When we write r_1 in the approximate form $r_1 = z_1 + (x^2+y^2)/2z_1$, eqn. (2) becomes

$$E(x_1, y_1, z) = \frac{ia}{\lambda z z_1} \int\int_{-\infty-\infty}^{\infty\infty} F(x, y) \exp\left\{\frac{-\pi i}{\lambda}\{(x-x_1)^2+(y-y_1)^2\} \times \left(\frac{1}{z}+\frac{1}{z_1}\right)\right\} dx\, dy \exp\left(\frac{-2\pi i(z+z_1)}{\lambda}+i\omega t\right). \quad . \quad . \quad . \quad . \quad (14)$$

Equations (7), (8) become, respectively,

$$\overline{E^2} = \frac{ia^2}{2\lambda z z_1 (z+z_1)} \int\int_{-\infty-\infty}^{\infty\infty} \overline{F(x, y)F(x+\xi, y+\eta)} \exp\left(\frac{-\pi i}{2\lambda z'}(\xi^2+\eta^2)\right) d\xi\, d\eta, \quad . \quad . \quad . \quad (15)$$

$$\overline{EE^*} = \frac{a^2}{(z+z_1)^2}\overline{FF^*} \quad . \quad . \quad . \quad . \quad . \quad . \quad . \quad . \quad (16)$$

where

$$z' = \frac{z z_1}{z+z_1}.$$

In the integrals A and B, z is replaced by z'. The eqns. (11) become

$$\left.\begin{aligned}
\overline{E_1} &= \frac{a}{z+z_1}\overline{F_1} \quad \overline{E_2} = \frac{a}{z+z_1}\overline{F_2}, \\
\overline{E_1^2} - \overline{E_1}^2 &= \frac{a^2}{(z+z_1)^2}\{\tfrac{1}{2}(\overline{F_1^2}-\overline{F_1}^2)(1-A_1)+\tfrac{1}{2}(\overline{F_2^2}-\overline{F_2}^2)(1+A_2) \\
&\quad -(\overline{F_1F_2}-\overline{F_1}\,\overline{F_2})B_{12}\}, \\
\overline{E_2^2} - \overline{E_2}^2 &= \frac{a^2}{(z+z_1)^2}\{\tfrac{1}{2}(\overline{F_1^2}-\overline{F_1}^2)(1+A_1)+\tfrac{1}{2}(\overline{F_2^2}-\overline{F_2}^2)(1-A_2) \\
&\quad +(\overline{F_1F_2}-\overline{F_1}\,\overline{F_2})B_{12}\}, \\
\overline{E_1E_2} - \overline{E_1}\,\overline{E_2} &= \frac{a^2}{(z+z_1)^2}\{\tfrac{1}{2}(\overline{F_1^2}-\overline{F_1}^2)B_1-\tfrac{1}{2}(\overline{F_2^2}-\overline{F_2}^2)B_2 \\
&\quad -(\overline{F_1F_2}-\overline{F_1}\,\overline{F_2})A_{12}\}.
\end{aligned}\right\} \quad (17)$$

3. The Joint Gaussian Probability Distribution

One may show by calculating the nth moment of E_1 and E_2 that although the variances of E_1 and E_2 change considerably during the course of propagation, the form of the probability distribution functions changes only a little. This result will be presented in detail elsewhere.

If F_1 and F_2 have a joint Gaussian distribution we are therefore approximately justified in assuming that E_1 and E_2 also have a joint Gaussian distribution.

Let the frequency function of E_1 and E_2 be

$$f(E_1, E_2)=\frac{1}{\sqrt{(1-\tau^2)}2\pi\sigma_1\sigma_2}\exp\left(-\frac{1}{2(1-\tau^2)}\left\{\frac{(E_1-\overline{E}_1)^2}{\sigma_1{}^2}-\frac{2\tau(E_1-\overline{E}_1)(E_2-\overline{E}_2)}{\sigma_1\sigma_2}+\frac{(E_2-\overline{E}_2)^2}{\sigma_2{}^2}\right\}\right) \quad . \quad . \quad . \quad . \quad (18)$$

where

$$\tau=\frac{\overline{E_1E_2}-\overline{E}_1\overline{E}_2}{\sqrt{\{(\overline{E_1{}^2}-\overline{E}_1{}^2)(\overline{E_2{}^2}-\overline{E}_2{}^2)\}}}$$

$$\sigma_1{}^2=\overline{E_1{}^2}-\overline{E}_1{}^2, \quad \sigma_2{}^2=\overline{E_2{}^2}-\overline{E}_2{}^2;$$

Fig. 1

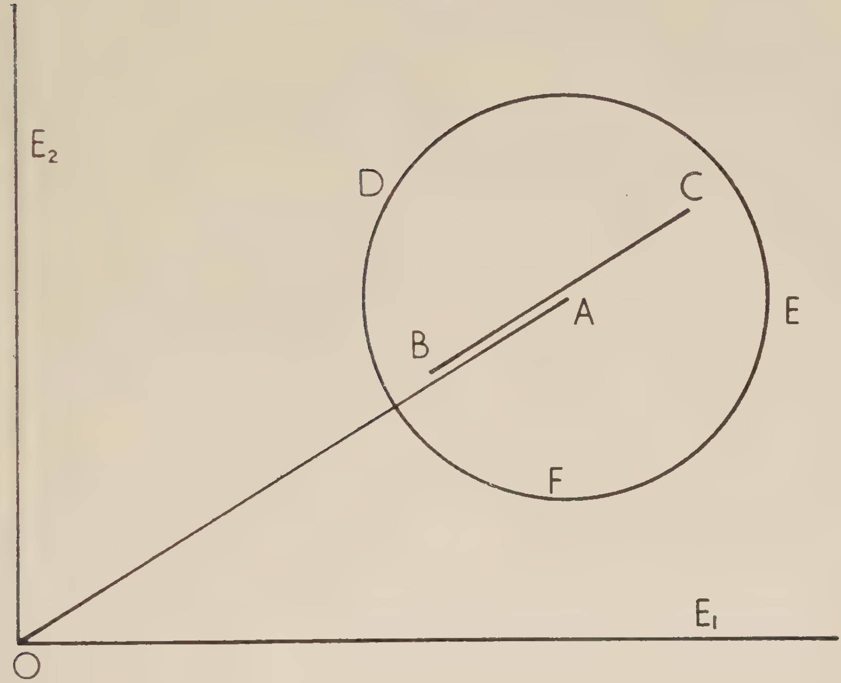

OA is the average signal $\overline{E}$. The line BC is the ' ellipse ' $f=$const. in the case of amplitude modulation ; the circle DEF is the ellipse for a randomly phased signal.

$f=$const. is an ellipse in the E_1, E_2 plane, with centre at $(\overline{E}_1, \overline{E}_2)$. Amplitude modulation is indicated by a straight line parallel to the average signal. The fading signal is said to be randomly phased when $f=$const. is a circle. See fig. 1.

If we are to discuss effectively the way in which E becomes randomly phased as the wave propagates, we require a measure of the ellipticity which is independent of the particular choice of axes E_1, E_2. We cannot use τ because when the curve $f=$ const. is not circular τ can always be made to vanish by a suitable rotation of the axes. $\tau=0$ is a necessary but not sufficient condition that $f=$ const. be a circle. We therefore define an *intrinsic correlation* ρ_N of the fading signal as follows: ρ_N is the maximum value of τ under rotation of the axes E_1, E_2.

The problem is to find ρ_N in terms of σ_1, σ_2, τ. We will first transform the coordinates E_1, E_2 to a system λ_1, λ_2 whose origin is at the centre of the ellipse and whose axes lie along the major and minor axes of the ellipse. Let the transformation be as follows. See fig. 2.

$$\left.\begin{aligned} E_1-\overline{E_1}&=\lambda_1\cos\theta-\lambda_2\sin\theta,\\ E_2-\overline{E_2}&=\lambda_1\sin\theta+\lambda_2\cos\theta.\end{aligned}\right\}\quad . \quad . \quad . \quad . \quad . \quad (19)$$

Fig. 2

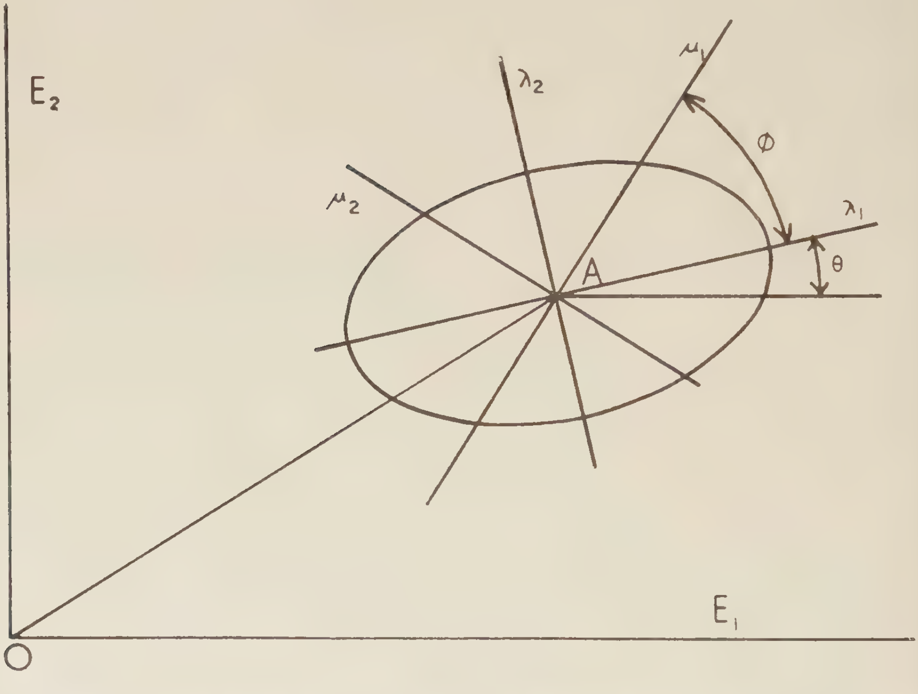

OA is the average signal $\overline{E}$. The axes λ_1, λ_2 are along the axes of the ellipse. The correlation coefficient is maximum in the μ_1, μ_2 coordinate system.

When substitution is made in the quadratic form in (18) we obtain

$$\lambda_1{}^2\left(\frac{\cos^2\theta}{\sigma_1{}^2}+\frac{\sin^2\theta}{\sigma_2{}^2}-\frac{2\tau\sin\theta\cos\theta}{\sigma_1\sigma_2}\right)+\lambda_2{}^2\left(\frac{\sin^2\theta}{\sigma_1{}^2}+\frac{\cos^2\theta}{\sigma_2{}^2}+\frac{2\tau\sin\theta\cos\theta}{\sigma_1\sigma_2}\right)$$
$$-2\lambda_1\lambda_2\left(\frac{\cos\theta\sin\theta}{\sigma_1{}^2}-\frac{\cos\theta\sin\theta}{\sigma_2{}^2}+\frac{\tau}{\sigma_1\sigma_2}(\cos^2\theta-\sin^2\theta)\right). \qquad (20)$$

The axes $\lambda_1\lambda_2$ lie along the axes of the ellipse when the coefficient of $\lambda_1\lambda_2$ in (20) vanishes. Therefore

$$\tan 2\theta = -\frac{2\tau\sigma_1\sigma_2}{\sigma_2^2-\sigma_1^2}. \qquad (21)$$

The frequency function of λ_1, λ_2 is

$$f(\lambda_1, \lambda_2) = \frac{1}{2\pi\sqrt{\overline{\lambda_1^2}\,\overline{\lambda_2^2}}}\exp\left\{-\tfrac{1}{2}\left[\frac{\lambda_1^2}{\overline{\lambda_1^2}}+\frac{\lambda_2^2}{\overline{\lambda_2^2}}\right]\right\}. \qquad (22)$$

A further rotation will be made to determine the system of coordinates in which the correlation coefficient τ is a maximum. See fig. 2.

$$\left.\begin{aligned}\lambda_1 &= \mu_1\cos\phi-\mu_2\sin\phi,\\ \lambda_2 &= \mu_1\sin\phi+\mu_2\cos\phi.\end{aligned}\right\} \qquad (23)$$

The correlation coefficient of μ_1, μ_2, τ_μ say, is obtained from the coefficient of $\mu_1\mu_2$ in the quadratic form

$$\frac{\lambda_1^2}{\overline{\lambda_1^2}}+\frac{\lambda_2^2}{\overline{\lambda_2^2}} = \mu_1^2\left(\frac{\cos^2\phi}{\overline{\lambda_1^2}}+\frac{\sin^2\phi}{\overline{\lambda_2^2}}\right)+\mu_2\left(\frac{\sin^2\phi}{\overline{\lambda_1^2}}+\frac{\cos^2\phi}{\overline{\lambda_2^2}}\right)$$

$$-2\mu_1\mu_2\left(\frac{1}{\overline{\lambda_1^2}}-\frac{1}{\overline{\lambda_2^2}}\right)\sin\phi\cos\phi$$

whence

$$\tau_\mu = \frac{\cos\phi\sin\phi(1/\overline{\lambda_1^2}-1/\overline{\lambda_2^2})}{\{1/(\overline{\lambda_1^2}\,\overline{\lambda_2^2})+\sin^2\phi\cos^2\phi(1/\overline{\lambda_1^2}-1/\overline{\lambda_2^2})^2\}^{1/2}}.$$

τ_μ is maximum when $\phi=\pi/4$, clearly. Therefore

$$\rho_N = \max\tau_\mu = \frac{1-\overline{\lambda_1^2}/\overline{\lambda_2^2}}{1+\overline{\lambda_1^2}/\overline{\lambda_2^2}} = \frac{\overline{\lambda_2^2}-\overline{\lambda_1^2}}{\overline{\lambda_1^2}+\overline{\lambda_2^2}}. \qquad (24)$$

This shows that if ϵ is the eccentricity of the ellipse, then $|\rho_N|=\epsilon^2/(2-\epsilon^2)$. The ratio $\overline{\lambda_1^2}/\overline{\lambda_2^2}$ is the ratio of the coefficients of λ_2^2 and λ_1^2 in (20). After some simplification we obtain

$$\rho_N = \frac{\sigma_2^2-\sigma_1^2}{\sigma_2^2+\sigma_1^2}\sec 2\theta = \frac{1}{\sigma_1^2+\sigma_2^2}\{(\sigma_1^2-\sigma_2^2)^2+(2\rho\sigma_1\sigma_2)^2\}^{1/2}. \qquad (25)$$

As a last point we give the expression for $f(\lambda_1, \lambda_2)$ in terms of σ_1, σ_2, ρ_N,

$$f(\lambda_1, \lambda_2) = \frac{1}{\pi(\sigma_1^2+\sigma_2^2)(1-\rho_N^2)}\exp\left\{-\frac{1}{\sigma_1^2+\sigma_2^2}\left(\frac{\lambda_1^2}{1+\rho_N}+\frac{\lambda_2^2}{1-\rho_N}\right)\right\}. \qquad (26)$$

The propagation of the fading amplitude will be described in terms of ρ_N and θ.

4. THE INTRINSIC CORRELATION OF THE FADING AMPLITUDE

ρ_N and θ as defined by eqns. (21), (25) are functions of z, since E_1 and E_2 depend on z. We shall find $\rho_N(z)$ and $\theta(z)$ in terms of the variances of F_1F_2 and the A's and B's. Let $\rho_N(0)$, $\theta(0)$ denote the corresponding properties of the ellipse of F_1F_2. We are free to choose the orientation of the ellipse of F_1F_2 and shall suppose that the axes F_1F_2 are parallel to those of the ellipse. Then from eqns. (11), (18), (21), (25),

$$\tan 2\theta(z) = -\frac{2\tau\sigma_1\sigma_2}{\sigma_2{}^2-\sigma_1{}^2} = -\frac{2(\overline{E_1E_2}-\bar{E}_1\bar{E}_2)}{(\overline{E_2{}^2}-\bar{E}_2{}^2)-\overline{E_1{}^2}-\bar{E}_1{}^2)}$$

$$= \frac{-(\overline{F_1{}^2}-\bar{F}_1{}^2)B_1+(\overline{F_2{}^2}-\bar{F}_2{}^2)B_2}{-(\overline{F_1{}^2}-\bar{F}_1{}^2)A_1+(\overline{F_2{}^2}-\bar{F}_2{}^2)A_2}. \quad . \quad . \quad . \quad . \quad (27)$$

$$\rho_N(z) = \frac{\sigma_2{}^2-\sigma_1{}^2}{\sigma_2{}^2+\sigma_1{}^2}\sec 2\theta = \frac{(\overline{E_2{}^2}-\bar{E}_2{}^2)-(\overline{E_1{}^2}-\bar{E}_1{}^2)}{(\overline{E_2{}^2}-\bar{E}_2{}^2)+(\overline{E_1{}^2}-\bar{E}_1{}^2)}\sec 2\theta$$

$$= \frac{-(\overline{F_2{}^2}-\bar{F}_2{}^2)A_2+(\overline{F_1{}^2}-\bar{F}_1{}^2)A_1}{(\overline{F_1{}^2}-\bar{F}_1{}^2)+(\overline{F_2{}^2}-\bar{F}_2{}^2)}\sec 2\theta(z). \quad . \quad . \quad . \quad (28)$$

For a point source it is only necessary to replace z in the A's and B's by z'.

These results are much simpler when the three spatial correlation functions of F_1 and F_2 are identical. This is the case when the same diffraction mechanism, such as a thin screen of varying refractive index, is responsible for the fluctuations in both F_1 and F_2. If two diffracting layers modified the amplitude and phase separately the spatial correlations would be different. Suppose then that $A_1=A_2=A$, $B_1=B_2=B$. We then have

$$\tan 2\theta = -B/A, \quad . \quad . \quad . \quad . \quad . \quad . \quad . \quad . \quad (29)$$

$$\rho_N(z) = \frac{(\overline{F_1{}^2}-\bar{F}_1{}^2)-(\overline{F_2{}^2}-\bar{F}_2{}^2)}{(\overline{F_1{}^2}-\bar{F}_1{}^2)+(\overline{F_2{}^2}-\bar{F}_2{}^2)} A \sec 2\theta$$

$$= \rho_N(0)\sqrt{(A^2+B^2)}. \quad . \quad . \quad . \quad . \quad . \quad . \quad . \quad . \quad (30)$$

$\rho_N(0)$ is defined to be the intrinsic correlation of the fluctuating amplitude F, which is seen from (24) to be

$$\frac{(\overline{F_2{}^2}-\bar{F}_2{}^2)-(\overline{F_1{}^2}-\bar{F}_1{}^2)}{(\overline{F_2{}^2}-\bar{F}_2{}^2)+(\overline{F_1{}^2}-\bar{F}_1{}^2)}.$$

The + root is chosen in (30) so that $\rho_N(z)\to\rho_N(0)$ as $z\to 0$. Equations (29), (30) are independent of the system of axes used for E and F provided θ is the angle between the major axes of the ellipses.

These equations have a simple physical interpretation. According to (10),

$$-A+iB = \frac{i}{2\lambda z}\int\int_{-\infty-\infty}^{\infty\,\infty} \rho(\xi,\eta)\exp\left(\frac{-\pi i}{2\lambda z}(\xi^2+\eta^2)\right)d\xi\,d\eta$$

$$= \frac{i}{\lambda z}\int\int_{-\infty-\infty}^{\infty\,\infty} \rho\{\sqrt{2}\xi,\sqrt{2}\eta\}\exp\left(\frac{-\pi i}{\lambda z}(\xi^2+\eta^2)\right)d\xi\,d\eta. \quad . \quad . \quad . \quad (31)$$

Therefore $-A+iB$ is the complex amplitude at the centre of the Fresnel diffraction pattern by an irregularity over which the amplitude is $\rho(\sqrt{2}\xi,\sqrt{2}\eta)$. $\rho_N(z)/\rho_N(0)$ and $\theta(z)$ are therefore the amplitude and phase of the diffraction pattern. The variation with distance z of the correlation at the receiver is a sort of focusing in the diffraction. The fading is randomly phased when $\rho_N(z)=0$, i.e. when the signal at the receiver due to a single irregularity has vanished.

Let us consider the previous example (eqn. (12))

$$\rho_1=\rho_2=\rho_{12}=\exp\left[-\frac{1}{r_0^2}(\xi^2+\eta^2)\right].$$

Equations (29), (30) become

$$\left.\begin{aligned}\rho_N(z)&=\frac{x}{\sqrt{(1+x^2)}}\rho_N(0)=\left(1+\frac{4\lambda^2z^2}{\pi^2r_0^4}\right)^{-1/2}\rho_N(0),\\ \tan 2\theta(z)&=\frac{1}{x}=\frac{2\lambda z}{\pi r_0^2}.\end{aligned}\right\} \qquad (32)$$

As $z\to\infty$ the ellipse of E becomes circular and rotates through an angle of $\pi/4$.

Fig. 3

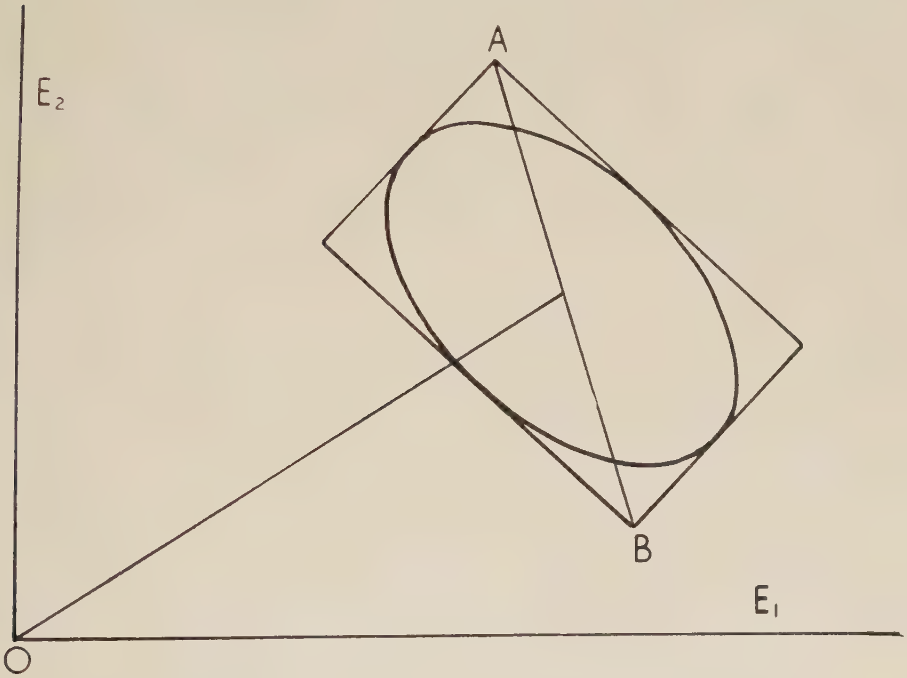

This shows the construction of the modulation imposed on the signal at the maximum height. The modulation is the line AB, the diagonal of the ellipse. The ellipse rotates counter-clockwise as z increases.

From the definition of $\rho_N(z)$ we know that $|\rho_N|\leqslant 1$. This implies a certain maximum value for z, viz.

$$z_{\max}=\frac{\pi r_0^2}{2\lambda}\sqrt{\left(\frac{1}{\rho_N^2(z)}-1\right)}.$$

We therefore see that if the irregularities are known in size and there is a known correlation in the fading at the receiver, then there is a maximum height at which the irregularities can be supposed to be situated. At that maximum height $\rho_N(0)=1$.

There is a simple geometrical relation between the straight modulation at the maximum and the ellipse at any other distance. From (32) we deduce that $\rho_N(z)=\rho_N(0)\cos 2\theta$. Therefore the straight line is the diagonal of the ellipse as shown in fig. 3.

4.1. *Effect of Point Source*

When a wave from a point source is incident on the screen then (27) and (28), etc. are still valid provided one changes z to z' (see (16)).

Fig. 4

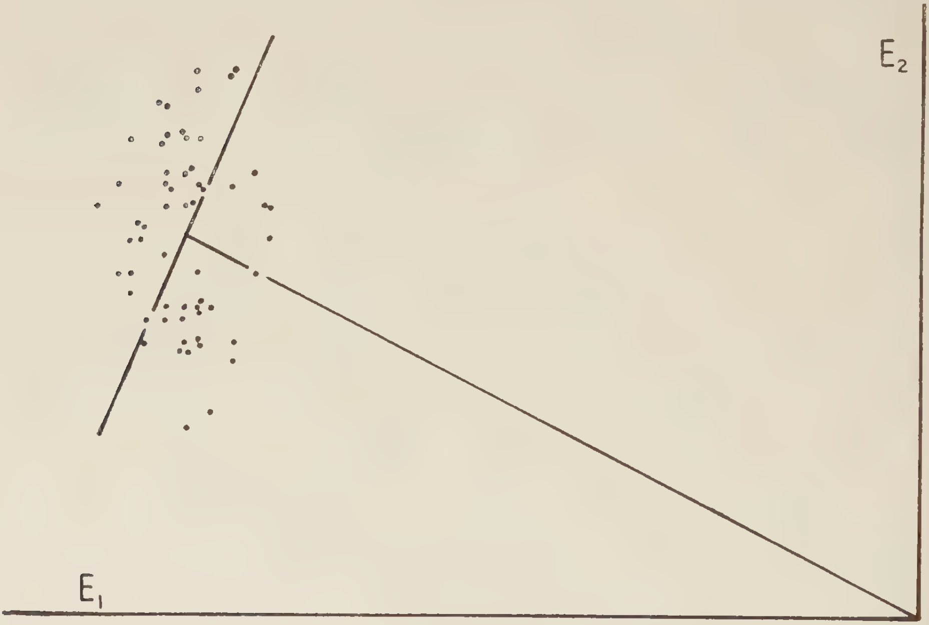

Typical daytime fading record on 16 kc/s : 10.00–11.00 G.M.T. July 6, 1949. The points represent the signal at minute intervals over the period of an hour. The diagonal of the probability ellipse is drawn to show the phase modulation at the maximum height.

4.2. *Experimental Results*

A certain amount of experimental work has been done on 16 kc/s. The signal from GBR, at Rugby, is recorded after nearly vertical reflection. The receiver records the components of the sky-wave which are in-phase and in-quadrature with the ground wave. By plotting these components as Cartesian coordinates one is able to study the fading signal in the light of the foregoing analysis. In fig. 4 an example is shown. The points represent the signal at minute intervals over the period of an hour. The curves of constant probability density are nearly elliptical. When the diagonal of the ellipse is drawn it appears that the modulation at the hypothetical maximum height is, in this example, very nearly phase modulation.

It is difficult to make a survey of the numerous records hitherto obtained because most of them show a large systematic phase variation which obscures the more rapid short period fading. The fading has a period of about three minutes, while the slow phase change may amount to $\pi/4$ in an hour.

The whole theory is at the limit of validity in the case of 16 kc/s, since $r=5\lambda$, and eqn. (1) is true under the assumption that $r \gg \lambda$. However the only extensive data are for this frequency and it is expected that the result will be not far from the truth.

Five hourly periods have been analysed. Four of these, including the one in fig. 4, show very nearly phase modulation. The other appears to be a mixture of phase and amplitude modulation.

In the example shown the parameter x may be calculated from the angle θ. From the relation $\rho_N(z)=\rho_N(0)\cos 2\theta$ we have $2\theta=46°$. Therefore, from (32) $x=\cot 2\theta=0{\cdot}96$. Assuming $z'=z/2=45$ km and $\lambda=18{\cdot}8$ km., we obtain $r_0=23$ km. This is in tolerable agreement with the estimates made by the spaced receiver method of measuring irregularity size (Hargreaves, private communication).

5. Conclusion

The fluctuating in-phase and quadrature components of a fading signal have been assumed to have a joint Gaussian probability distribution. This distribution has not been described in terms of the usual variances and correlation coefficient, but in terms of two parameters ρ_N and θ : ρ_N measures the extent to which the signal is randomly phased and θ measures the change in phase of the modulation on the signal after it has left the screen. These two parameters are the amplitude and phase of the Fresnel diffraction pattern due to a single irregularity. The experimental records of 16 kc/s fading analysed according to this theory show that at this frequency the modulation is highly correlated at the ionosphere and that it is generally phase modulation.

Acknowledgments

The author wishes to thank Dr. K. G. Budden and also Mr. J. A. Ratcliffe and his colleagues of the Cavendish Laboratory for much criticism and helpful discussion of the work presented here. He also wishes to thank the National Research Council of Canada for the award of a Special Scholarship during the past two years.

REFERENCES

BAKER, B. B., and COPSON, E. T., 1950, *The Mathematical Theory of Huygens' Principle* (Oxford).

BOOKER, H. G., and CLEMMOW, P. C., 1950, *Proc. Inst. elect. Engrs*, **97,** 11.

BOOKER, H. G., RATCLIFFE, J. A., and SHINN, D. H., 1950, *Phil. Trans. roy. Soc.* A, **242,** 856.

BOWHILL, S. A., 1956, *Penn. State Rep.* 89 ; 1957, *J. atmos. terr. Phys.*, **11,** 91.

HEWISH, A., 1951, *Proc. roy. Soc.* A, **207,** 81.

RATCLIFFE, J. A., 1948, *Nature, Lond.*, **162,** 9 ; 1956, *Rep. Progr. Phys.*, **19,** 188.

RICE, S. O., 1944, *Bell Syst. tech. J.*, **23,** 282 ; 1945, *Ibid.*, **24,** 46.

CORRESPONDENCE

The Hardening of Copper by Neutron Irradiation

By M. A. Adams and P. R. B. Higgins
Metallurgy Division, Atomic Energy Research Establishment, Harwell

[Received February 9, 1959]

Various studies have been made of the effects of neutron irradiation on the mechanical properties of metallic materials (see the review articles of Cottrell (1956, 1957) Glen (1955) and Kinchin and Pease (1955)), and it is now generally recognized that irradiation may cause hardening in two broadly different ways: (*a*) by making the nucleation of slip difficult (source hardening) and/or (*b*) by making slip propagation difficult (lattice friction hardening). Copper has been most extensively investigated but in none of the experiments on this material has the relative contribution of the two forms of hardening been clearly separated. One means of making the separation is, however, suggested by work that has been done on mild steel, for which it has been shown, both theoretically (Petch 1953) (Cottrell 1958) and experimentally (Hall 1951) (Petch 1953) (Hull and Mogford 1958), that the lower yield stress is related to the grain size by the equation:

$$\sigma_y = \sigma_i + k_y \, . \, d^{-1/2} \qquad \ldots \ldots \ldots \quad (1)$$

where, following Cottrell's (1958) notation, d is the half-grain diameter, σ_y the shear stress at the lower yield point, k_y a measure of the shear stress to operate dislocation sources and σ_i the shear stress resisting the movement of dislocations across the slip plane. Equation (1) describes generally the conditions for yield propagation when there is a sharp yield point. Copper shows such a yield point after irradiation (fig. 1.) so that measurements of the yield strength as a function of $d^{-1/2}$ on specimens irradiated various amounts should reveal whether source hardening (changes in k_y) or lattice friction hardening (changes in σ_i) occurs.

Wires of 0·085 in. diameter were prepared from Matthey spectrographic (99·999%) copper rods by successively swaging (50% reduction in area) and vacuum annealing (600°c for 2 hours). After a final swage to 0·060 in. diameter, batches of 3·5 cm long specimens were vacuum annealed for 2 hours at temperatures from 400°c to 1000°c to give grain sizes (determined from a metallographic examination of the specimens after testing) in the range from 0·0025 cm diameter to 0·08 cm diameter. Specimens covering the complete grain-size range were sealed in evacuated silica capsules and irradiated at a temperature of about 50°c for 1 and 3 weeks

Fig. 1

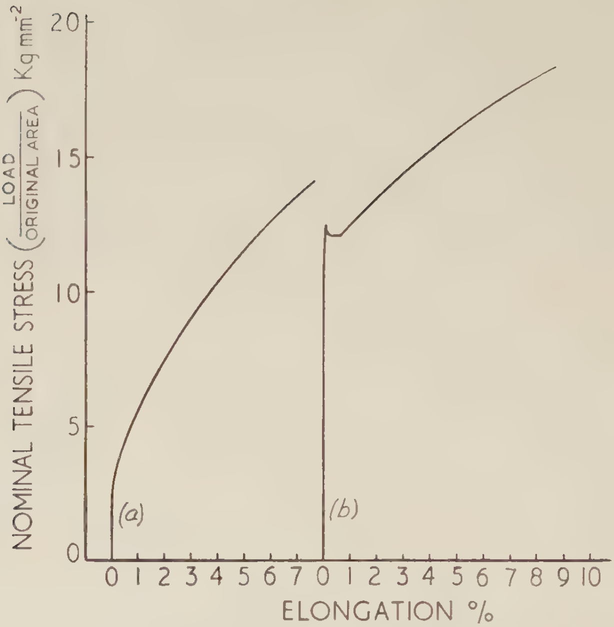

Stress–strain curves for (*a*) un-irradiated and (*b*) irradiated (3 weeks in a fast neutron flux of 3×10^{11} n cm^{-2} sec^{-1}) polycrystalline copper specimens of 0·0025 cm grain diameter ($d^{-1/2} = 28$ cm$^{-1/2}$), tested at 20°c.

Fig. 2

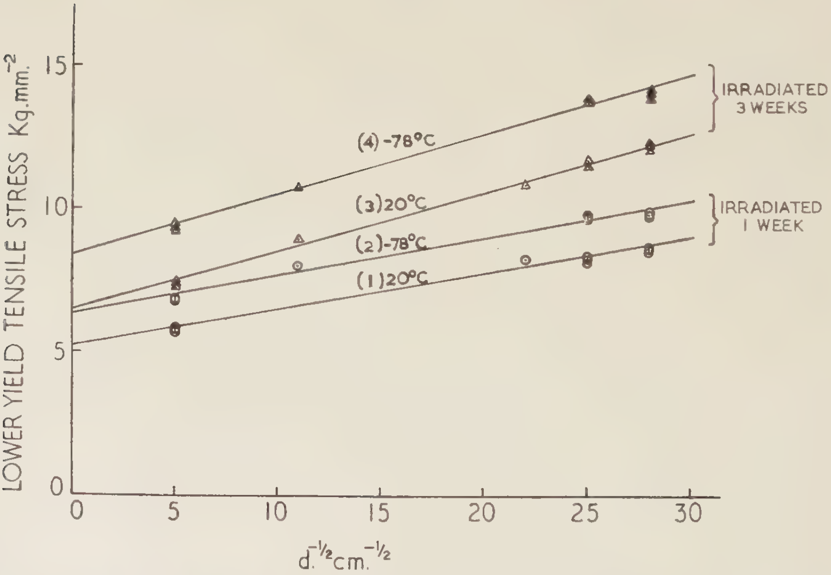

Lower yield stress values at 20°c and −78°c of copper samples covering a range of grain sizes, after irradiations of 1 and 3 weeks in a fast neutron flux of 3×10^{11} n cm^{-2} sec^{-1}.

inside a fuel element in the BEPO reactor. The measured thermal neutron flux was $4 \cdot 5 \times 10^{11}$ n cm^{-2} sec^{-1}, the measured flux above about 1 MeV, 3×10^{11} n cm^{-2} sec^{-1}, and the estimated flux between 0·4 ev and 1 MeV, $1 \cdot 5 \times 10^{12}$ n cm^{-2} sec^{-1} (Wright 1959, private communication).

Tensile tests were made at 20°C and −78°C in the autographically recording tensile machine described by Adams (1958). The wires were held by their ends in carefully aligned clamp type grips leaving a gauge length of 2 cm, and were extended at a strain-rate of $5 \cdot 7 \times 10^{-4}$ sec^{-1}.

Results for the two irradiations and two testing temperatures are shown in fig. 2 as a plot of lower yield stress against $d^{-1/2}$ and can be summarized as follows:

1. At a fixed neutron dose and testing temperature the yield stress of irradiated polycrystalline copper increases, within the limits of accuracy of the experimental measurements, linearly with increasing $d^{-1/2}$ in agreement with eqn. (1).
2. The effect of increasing irradiation is to raise both σ_i and k_y (compare curves 1 and 3 and curves 2 and 4). Thus lattice friction hardening and source hardening proceed simultaneously.
3. The increased yield strength of irradiated copper at −78°C compared with 20°C, arises from a temperature dependence of the lattice friction component of hardening (compare curves 1 and 2 and curves 3 and 4).

The feasibility of the various theories of radiation hardening can now be assessed in the light of these results. Thus, it seems unlikely that a source hardening mechanism with the required lack of sensitivity to temperature can be provided by a point defect atmosphere locking effect, or by a simple jog process. If, however, dislocations become heavily jogged, as recent observations on quenched metals suggest (Hirsch *et al.* 1958), temperature independent locking is conceivable, since a large length of jog on some plane other than a close-packed one may constitute an almost immovable lock. Vacancies condensed as voids on dislocations (Coulomb and Friedel 1957) could also cause source-hardening of a type which is relatively temperature insensitive. Regarding the lattice friction component of hardening, the 'peg' theory (Cottrell 1957) seems most likely to provide a mechanism with the required sensitivity to temperature. Aggregates of defects (Kunz and Holden 1954 a, b), dislocation rings formed by the collapse of vacancy clusters (Smallman and Westmacott 1959), and disturbed zones in the lattice (Seeger 1958) are possible 'pegs' through which gliding dislocations could be forced by the applied stress with appreciable assistance from thermal fluctuations at relatively low temperatures.

Further work is proceeding to determine the dose dependence and annealing characteristics of the two types of hardening. Full details of the experiments will be published later.

ACKNOWLEDGMENTS

Grateful acknowledgment is made to Dr. R. E. Smallman for his contribution to discussions which led to the initiation of these experiments.

REFERENCES

ADAMS, M. A., 1958, U.K. Atomic Energy Res. Estab. Rep. No. M/R.2604.
COTTRELL, A. H., 1956, *Metallurgical Reviews*, Vol. 1, Part 4; 1957, *Inst. Met. Monograph* No. 23; 1958, *Trans. Met. Soc. A.I.M.E.*, **212,** 192.
COULOMB, P., and FRIEDEL, J., 1957, *Dislocations and Mechanical Properties of Crystals* (New York: Wiley), p. 555.
GLEN, J. W., 1955, *Advanc. Phys.*, **4,** 381.
HALL, E. O., 1951, *Proc. phys. Soc. Lond.* B, **64,** 747.
HIRSCH, P. B., SILCOX, J., SMALLMAN, R. E., and WESTMACOTT, K. H., 1958, *Phil. Mag.*, **3,** 897.
HULL, D., and MOGFORD, I. L., 1958, *Phil. Mag.*, **3,** 1213.
KINCHIN, G. H., and PEASE, R. S., 1955, *Rep. Progr. Phys.*, **18,** 1.
KUNZ, F. W., and HOLDEN, A. N., 1954 a, *Phys. Rev.*, **94,** 1417; 1954 b, *Acta Met.*, **2,** 816.
PETCH, N. J., 1953, *J. Iron St. Inst.*, **174,** 25.
SEEGER, A., 1958, 2nd United Nations International Conference on the Peaceful uses of Atomic Energy, A/Conf.15/P/998.
SMALLMAN, R. E., and WESTMACOTT, K. H., 1959, *J. app. Phys.* (in the press).

Variation of Young's Modulus of Fused Quartz Fibre with Diameter

By D. J. TRITTON
Cavendish Laboratory, Cambridge

[Received April 10, 1959]

THERE has been some dispute (Jurkov 1935, Reinkober 1939, Tighe 1956) as to whether Young's modulus of fused quartz-fibre varies with diameter. Some recent experiments by the author demonstrate clearly that it does, though they do not fill in the detailed form of the variation.

The observations were made during the development of a quartz-fibre anemometer for measuring the low air speeds of free convective flows. This instrument consists of a fused quartz-fibre (of diameter in the range 20 to 100 microns and length in the range 1 to 3 cm) cemented into a piece of hypodermic tubing. When this is placed in an air flow the deflection of the free end, observed on the eyepiece scale of a tele-microscope, is a measure of the velocity.

During calibration runs, it became clear that the results could not be consistently interpreted using the value of $5{\cdot}18 \times 10^{11}$ dynes cm^{-2} for Young's modulus of quartz-fibre in Kaye and Laby's (1956) tables. Hence, some measurements were carried out. The method was a determination of the resonant frequencies of some of the fibres, as mounted for velocity measurements. A fibre may be regarded as a bending beam with one end free and the other clamped. Hence, its equation of motion is

$$m\frac{\partial^2 y}{\partial t^2} = F - EI\frac{\partial^4 y}{\partial x^4}$$

which becomes

$$EI\frac{d^4 y_0}{dx^4} - 4\pi^2 m\nu^2 y_0 = F_0$$

for a periodic motion of frequency ν. Here y is the displacement of the fibre at distance x from its fixed end and y_0 the amplitude of this displacement; F is the bending force per unit length and F_0 its amplitude; m, E and I are the mass per unit length, Young's modulus, and moment of the cross section of the fibre. The boundary conditions on this are

$$y_0 = \frac{dy_0}{dx} = 0 \quad \text{at} \quad x = 0,$$

$$\frac{d^2 y_0}{dx^2} = \frac{d^3 y_0}{dx^3} = 0 \quad \text{at} \quad x = l,$$

so that the resonant frequencies are given by

$$\begin{vmatrix} 1 & 1 & 1 & 1 \\ 1 & -1 & i & -i \\ e^{\phi} & e^{-\phi} & -e^{i\phi} & -e^{-i\phi} \\ e^{\phi} & -e^{-\phi} & -ie^{i\phi} & ie^{-i\phi} \end{vmatrix} = 0 \qquad \phi = \sqrt[4]{\frac{4\pi^2 m\nu^2}{EI}}\,.\,l$$

which reduces to

$$\cos\phi\cosh\phi = -1.$$

The first four eigenvalues of ϕ are

$$\phi_1 = 1{\cdot}875,\ \phi_2 = 4{\cdot}712,\ \phi_3 = 7{\cdot}853,\ \phi_4 = 11{\cdot}00.$$

Young's modulus is thus given in terms of the resonant frequencies as

$$E = \frac{4\pi^2 l^4 m\nu_n{}^2}{I\phi_n{}^4} = \frac{64\pi^2 l^4 \rho_Q}{d^2}\cdot\left(\frac{\nu_n}{\phi_n{}^2}\right)^2$$

where ρ_Q is the density of quartz and d the diameter of the fibre; ν_n is the observed nth resonant frequency. This treatment ignores damping, but the fact that good agreement was obtained in the experimental observations of different eigenvalues is a justification for neglecting its effect on the resonant frequencies.

The resonances were found by mounting the fibre 10 cm or so in front of a loudspeaker connected to an electronic oscillator. The fibre sometimes responded to one of the higher harmonics in the loudspeaker's note; it was then necessary to discover at what frequency the fibre was vibrating, which was done by observing it in the light of a stroboscope. The frequencies were all in the low audio range, and there was overlap between the ranges covered by the first few eigenvalues for the various fibres; the results are thus not due to some frequency-dependence.

Of the other quantities needed for calculating E, the diameters of the larger fibres were measured with a travelling microscope and those of the small ones by a wedge-fringe optical interference method.

The fibres investigated came from two different sources. Ones of approximately 20 and 45 microns in diameter were supplied by Messrs. Taylor, Taylor and Hobson Ltd. of Leeds who kindly measured the density of their original material for me ($2{\cdot}20\,\mathrm{g\,cm^{-3}}$). Since the experiments of Douglas and Isard (1951) showed that density variations produced by heat treatment are only of the order of 0·2%, this figure may be used for the fibres. A fibre of approximately 75 microns in diameter was made from some scrap fused quartz, of which the origin is not known. The same figure was used for the density of this; Tighe (1956) remarks that there are no significant variations in the density of different samples of fused quartz.

The results were

Fibre diameter (cm)	Young's modulus (dynes $\mathrm{cm^{-2}}$)
$1{\cdot}97 \times 10^{-3}$	$8{\cdot}1 \times 10^{11}$
$4{\cdot}42 \times 10^{-3}$	$6{\cdot}85 \times 10^{11}$
$7{\cdot}53 \times 10^{-3}$	$5{\cdot}95 \times 10^{11}$

I estimate that these values for Young's modulus are accurate to around 4%. Each is based on the results for a single fibre, but, further experiments were made with fibres of other lengths from the same reels. Accurate diameter measurements were not made on these (since this is a tedious and time-consuming job), but, supposing them to have the same diameters gives agreement with the above results to within 3%. It is thus safe to conclude that the above are not freak results produced by, for example, a flaw in one of the fibres.

It is doubtful whether samples of quartz from different sources always have the same constitution; Drane (1929), for instance, concluded that the results of various experimenters on the elasticity of fused quartz rod could be explained only by actual variability. Hence, a comparison between the 75·3 micron fibre and the others is of doubtful value. On the other hand, the manufacturers assure me that the 19·7 and 44·2 micron fibres were made of the same material, so that the difference, considerably more than the experimental error, in Young's moduli of the two is the most interesting result of this work. The difference is very likely due to the rate of cooling of the fibre during manufacture. Comparisons with other workers are also open to the criticism that the material may not be just the same. It is, however, perhaps worth noting that my values of E for the 44·2 and 75·3 micron fibres are within the range of the various curves given by Reinkober (1932, 1937, 1939) but that the increase as the diameter is decreased is even larger than that observed by him. Jurkov (1935) observed a modulus of about $9{\cdot}4 \times 10^{11}\,\mathrm{dynes\,cm^{-2}}$ for all diameters; this seems unlikely in view of my results.

The resonance method can be recommended as a means of finding the full form of the variation. However, it should be noted that if there is a variation in the local elasticity of an individual fibre with distance from the axis the modulus would be different for bending than for stretching.

The results of this work have been successfully used in determining from calibrations of a number of quartz-fibre anemometers the drag produced by low Reynolds number flow past cylinders. A report on this will be published elsewhere shortly (Tritton 1959).

ACKNOWLEDGMENTS

I am most grateful to Dr. A. A. Townsend for his encouragement and, in particular, for suggesting the resonance technique. My thanks go also to Messrs. Taylor, Taylor and Hobson, Ltd. (in particular, their chief physicist, Mr. D. F. Burnett) for making the density measurement and for general interest and assistance and to Dr. J. E. Stanworth (of the British Thomson-Houston Co., Ltd.) for his helpful comments on the results.

REFERENCES

DOUGLAS, R. W., and ISARD, J. O., 1951, *J. Soc. Glass Tech.*, **35,** 206.
DRANE, H. D. H., 1929, *Proc. roy. Soc.* A, **122,** 274.
JURKOV, S., 1935, *Tech. Phys. U.S.S.R.*, **1,** 386.
KAYE, G. W. C., and LABY, T. H., 1956, *Tables of Physical & Chemical Constants*, 11th edition (Longmans).
REINKOBER, O., 1932, *Phys. Z.*, **33,** 32 ; 1937, *Ibid.*, **38,** 112 ; 1939, *Ibid.*, **40,** 385.
TIGHE, N. J., 1956, NBS circular 569.
TRITTON, D. J., 1959, *J. Fluid Mech.*, **6** (to be published).

Waves in Electron Clouds

By J. R. PIERCE and L. R. WALKER
Bell Telephone Laboratories Inc., Murray Hill,
New Jersey, U.S.A.

[Received February 2, 1959]

IN a recent paper in this journal (Piddington 1958) the author in referring to an earlier paper of ours (Pierce and Walker 1956) quotes us as saying: " No definitive conclusion can be drawn from it (the steady state analysis) alone." What we said was: " This relation, the dispersion relation, is obviously significant for the problem on hand since it describes an intrinsic property of the ion stream and may, of itself, give some valuable information. But no definitive conclusion can be drawn from it alone about any specific problem, since only the boundary conditions can say what part of the ω–Γ spectrum is excited and to what extent."

REFERENCES

PIDDINGTON, J. H., 1958, *Phil. Mag.*, **3,** 1241.
PIERCE, J. R., and WALKER, L. R., 1956, *Phys. Rev.*, **104,** 306.

REVIEWS OF BOOKS

Modern Geometrical Optics. By MAX HERZBERGER. (New York and London: Interscience Publishers, 1958.) [Pp. 504.] $15.

THIS book, by one of America's leading optical specialists, deserves an honoured place in every optical library. It contains thirty-nine chapters (four in an Appendix), a bibliography and an index. In his preface, the author reminds us that lens design is still more of an art than a science and that the acquaintance of the average lens designer with higher mathematics is limited. For this reason, he has tried to restrict the demands on the reader's mathematical technique to the minimum. But this minimum is not a very small one and the average lens designer who reads the whole of Dr. Herzberger's book will find that he has learned a good deal of higher mathematics as well as of geometrical optics. Without this mathematics, a systematic account of the subject would be impracticable. Vectors are freely used, for the sake of the simplicity which they bring, and an admirably lucid introductory course on vector analysis is provided in the Appendix by Dr. Erich Marchand. Another chapter in this Appendix, entitled Miscellaneous Mathematical Tools, supplies necessary background knowledge of matrices, of the method of least squares, of Gaussian brackets, and of polynomial approximation methods. By thus allowing the reader to educate himself as he goes along, Dr. Herzberger is able to proceed from the thoroughly practical and mathematically elementary ray-tracing methods which occupy his first seven chapters, through Gaussian optics in the next seven, to a concise and elegant presentation of Hamilton's ideas, according to which the laws of geometrical image formation by an optical system are expressed through a single characteristic function, or Eikonal function, as it later came to be called.

Of many other interesting topics treated in the last part of the book we here mention the method of fitting a fifth-order mathematical model (simplified approximation) to an optical system on the basis of the results of tracing a relatively small number of meridonal and skew rays, and the use of spot diagrams as a tool in lens design. The author's use of diapoints often lends an agreeably modern flavour even to the more elementary discussions.

Dr. Herzberger's wide knowledge and enthusiasm for his subject illuminates the whole book and in the fourteen years spent, as he tells us, on its writing and rewriting he has produced a major contribution to the optical literature.

E. H. LINFOOT.

Theories of Figures of Celestial Bodies. By WENCESLAS S. JARDETZKY. (New York: Interscience Publishers, 1959.) [Pp. 186.] 45*s*.

A MATHEMATICIAN who wants to find out what has been done, and who has been doing it, in the subject of the mechanics of rotating fluid masses, could hardly do better than start by consulting this book.

Professor Jardetzky's breadth of knowledge of the European and American literature on the subject is evident in this concise and clearly written historical review. In the first part of the book, the author gives an outline of the work done by early investigators, Jacobi, Poincare, and many others, on bodies of fluid rotating as if solid. The basic mathematical equations are stated, methods and results of solutions are indicated, physical principles and various simplifying assumptions are discussed. In the second part, more complicated problems are considered, particularly such conditions as are known to exist in actual celestial bodies—zonal differences of rotation and other internal motions, bodies of mixed composition, small oscillations, and the effects of external fields of force.

There is a very extensive bibliography.

J. E. J.

[The Editors do not hold themselves responsible for the views expressed by their correspondents.]

Fig. 3

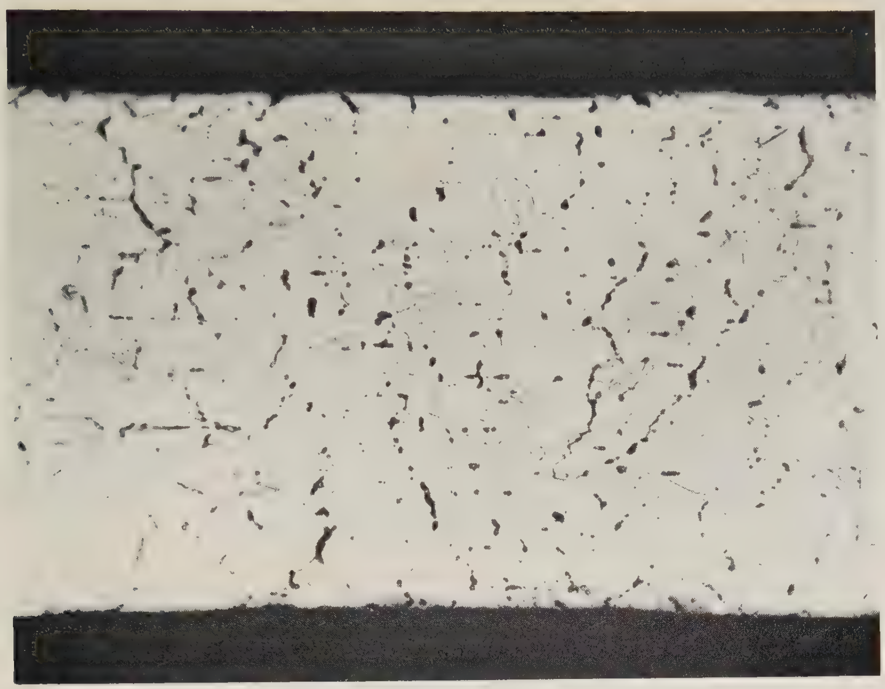

Voids along grain boundaries in a specimen fractured at 480°c with a uniaxial stress of 4730 p.s.i. Hand polished and etched. ×270.

Fig. 4

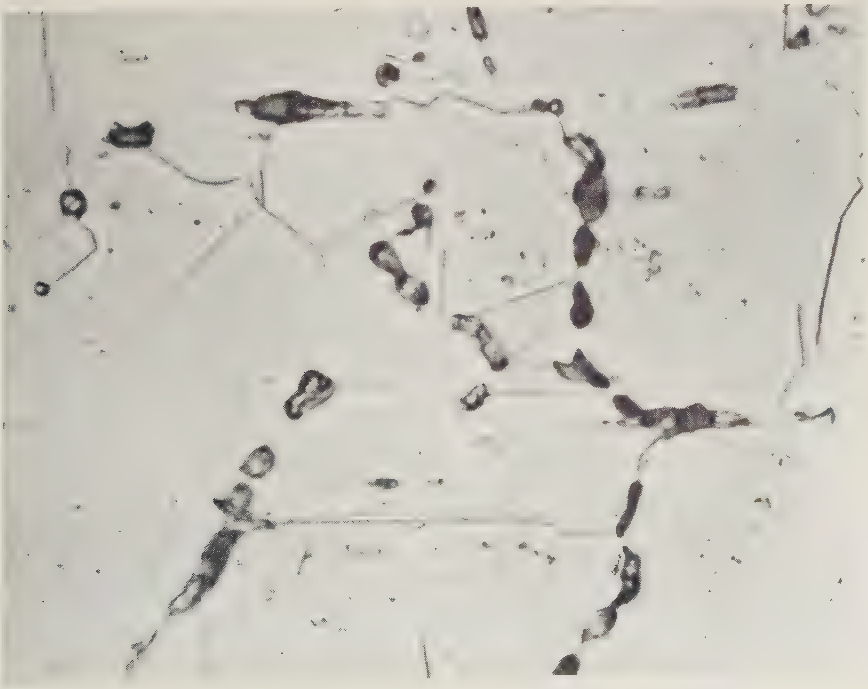

Same as fig. 3. ×2000.

Fig. 5

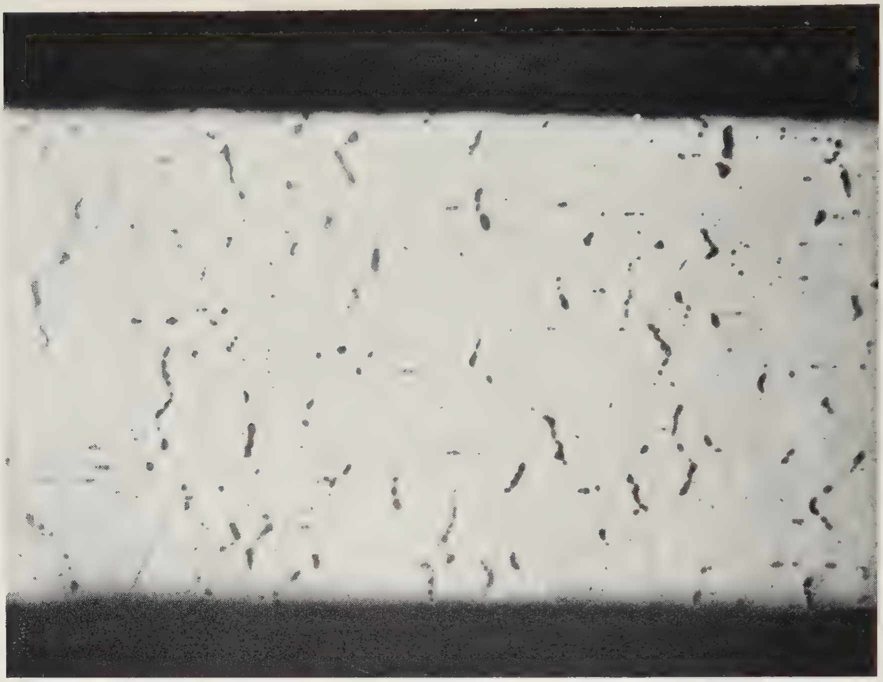

Voids formed at 410°c with stress of 4730 p.s.i. ×270.

Fig. 6

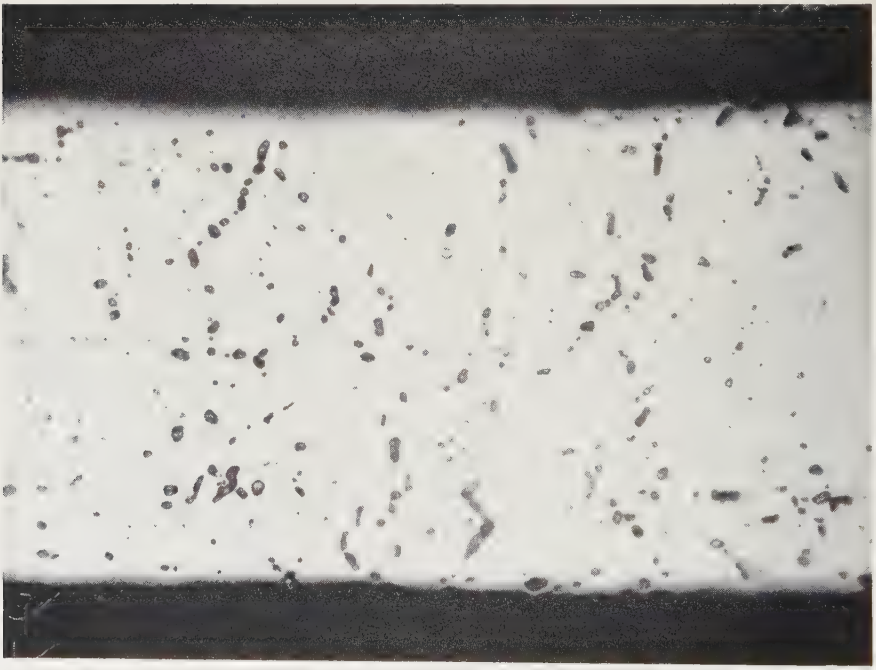

Voids formed at 410°c with stress of 3000 p.s.i. ×270.

Fig. 8

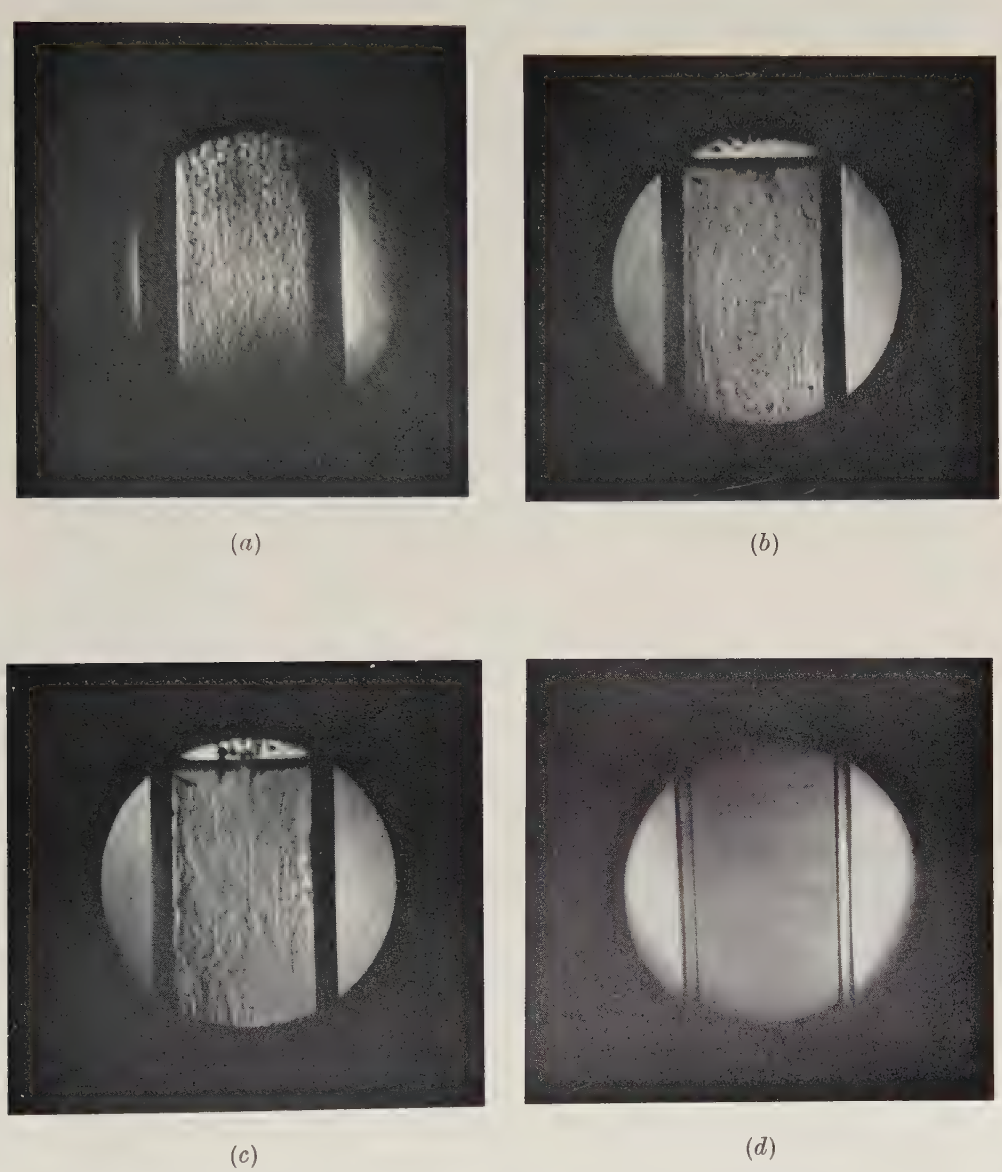

(a) (b) (c) (d)

Schlieren pictures of mixture at various temperatures :
(a) 31° ; (b) 32° ; (c) 33° ; (d) 36°C.

Fig. 1

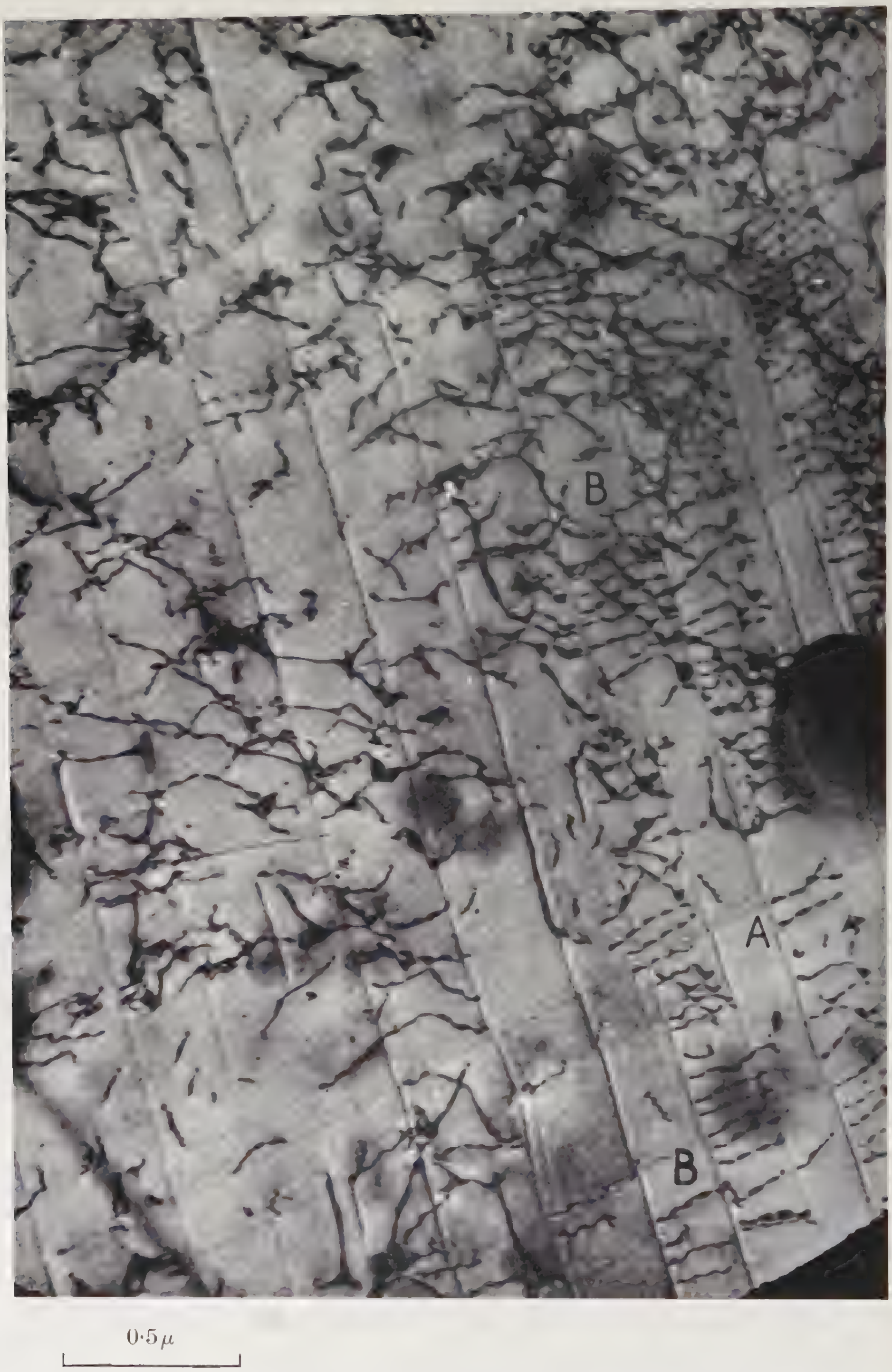

Contrast produced by surface slip steps. At A and B dislocations are associated with slip steps. Mag. × 50 000.

Fig. 2

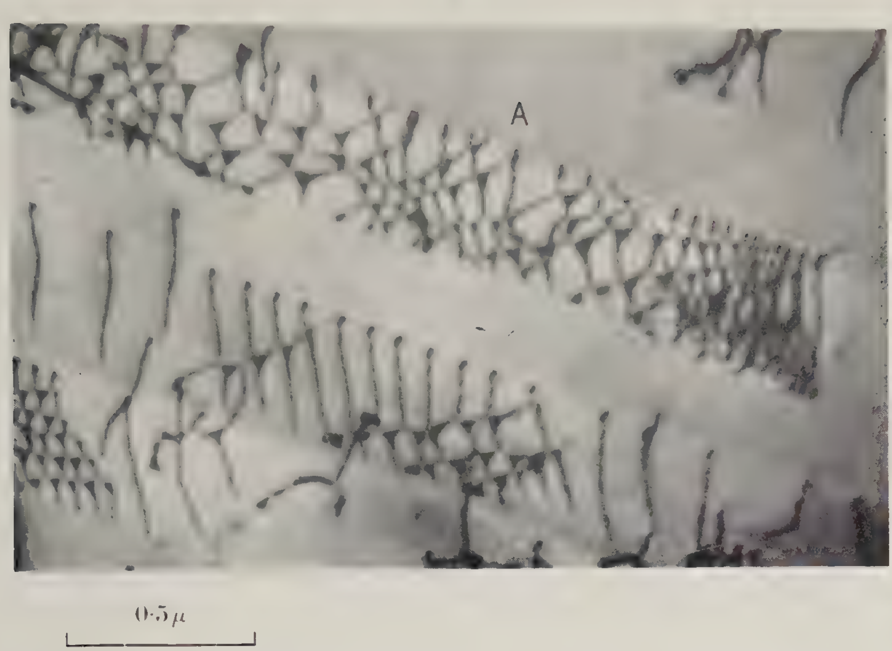

Dislocation networks at the surface. At A dislocations meet the protected surface in visible lines corresponding to slip steps. Mag. × 50 000.

Fig. 6

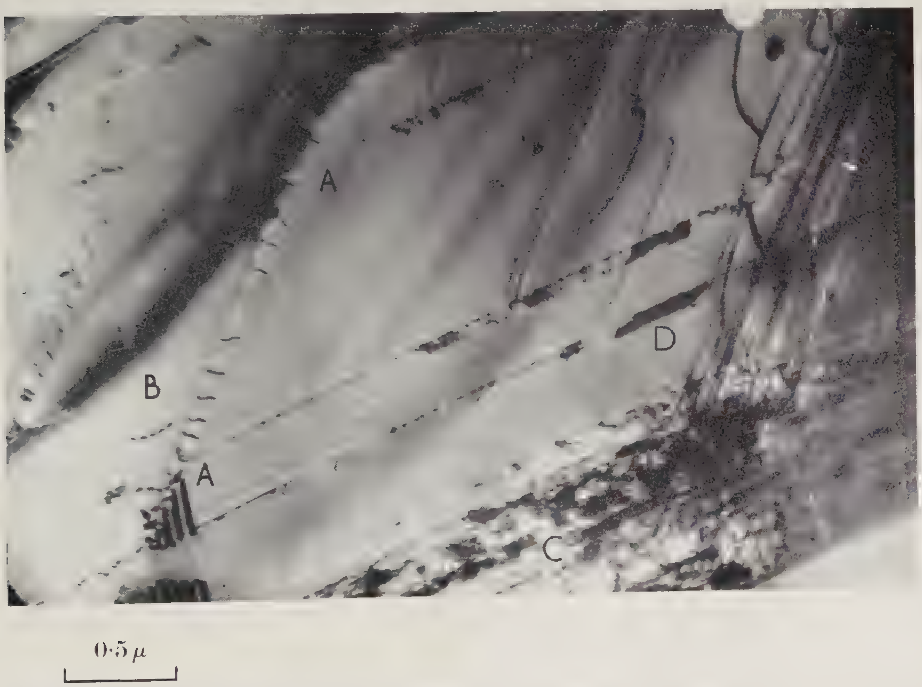

Surface of a fatigue specimen. Note at A offsets produced by slip on two systems, at B slip similar to that in simple tension, at C fatigue striation and at D patches of stacking fault. Mag. × 33 000.

Fig. 3

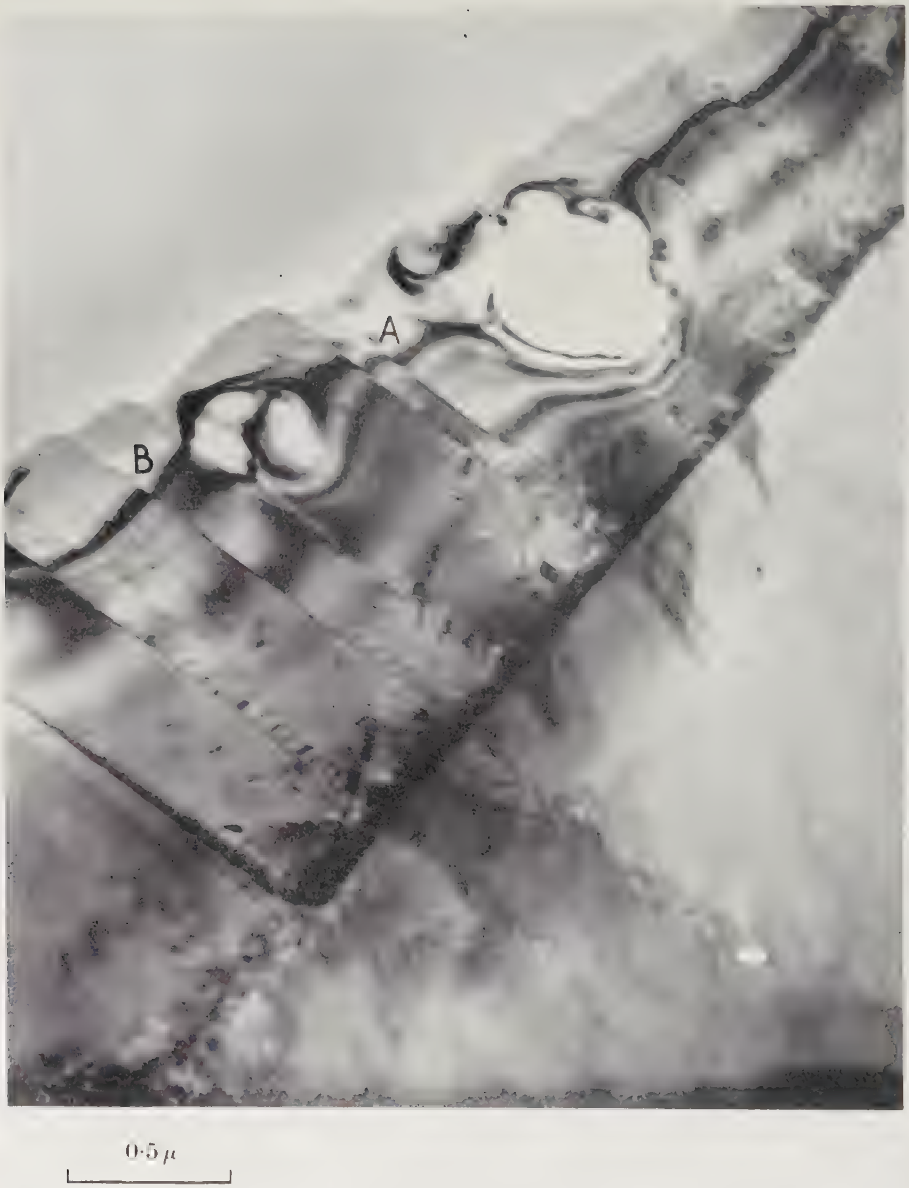

Slip steps at the edge produced by dislocations lying in the slip planes. Note shifts in extinction contour at A and B. Mag. ×45 000.

Fig. 4

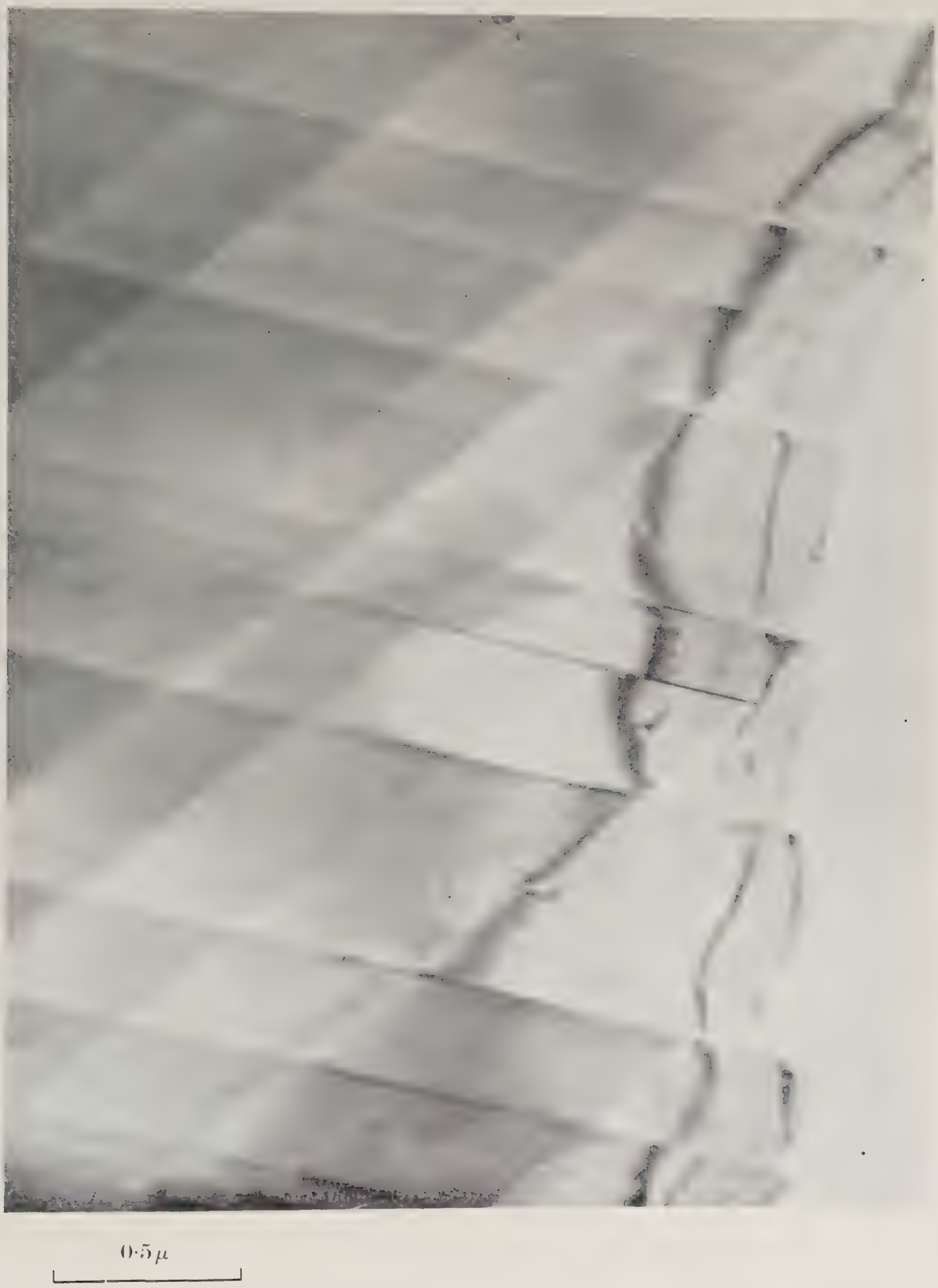

Intensity change on crossing slip steps. Note also the offsets produced where the slip lines intersect. These can be compared with the steps at the edge. Mag. × 55 000.

Fig. 7

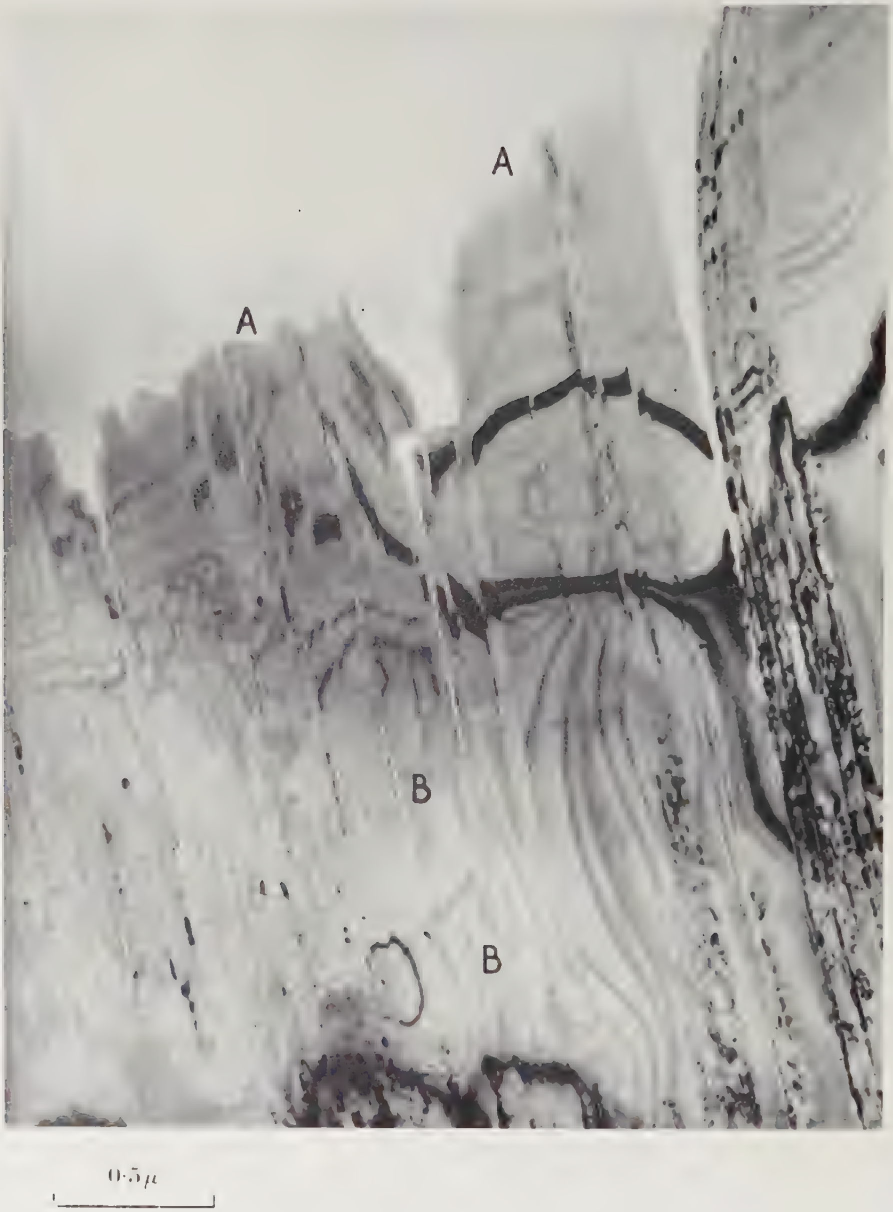

Fatigue specimen showing at A slip line without associated edge steps and at B light regions corresponding possibly to fatigue cracks. Mag. ×45 000.

Fig. 8

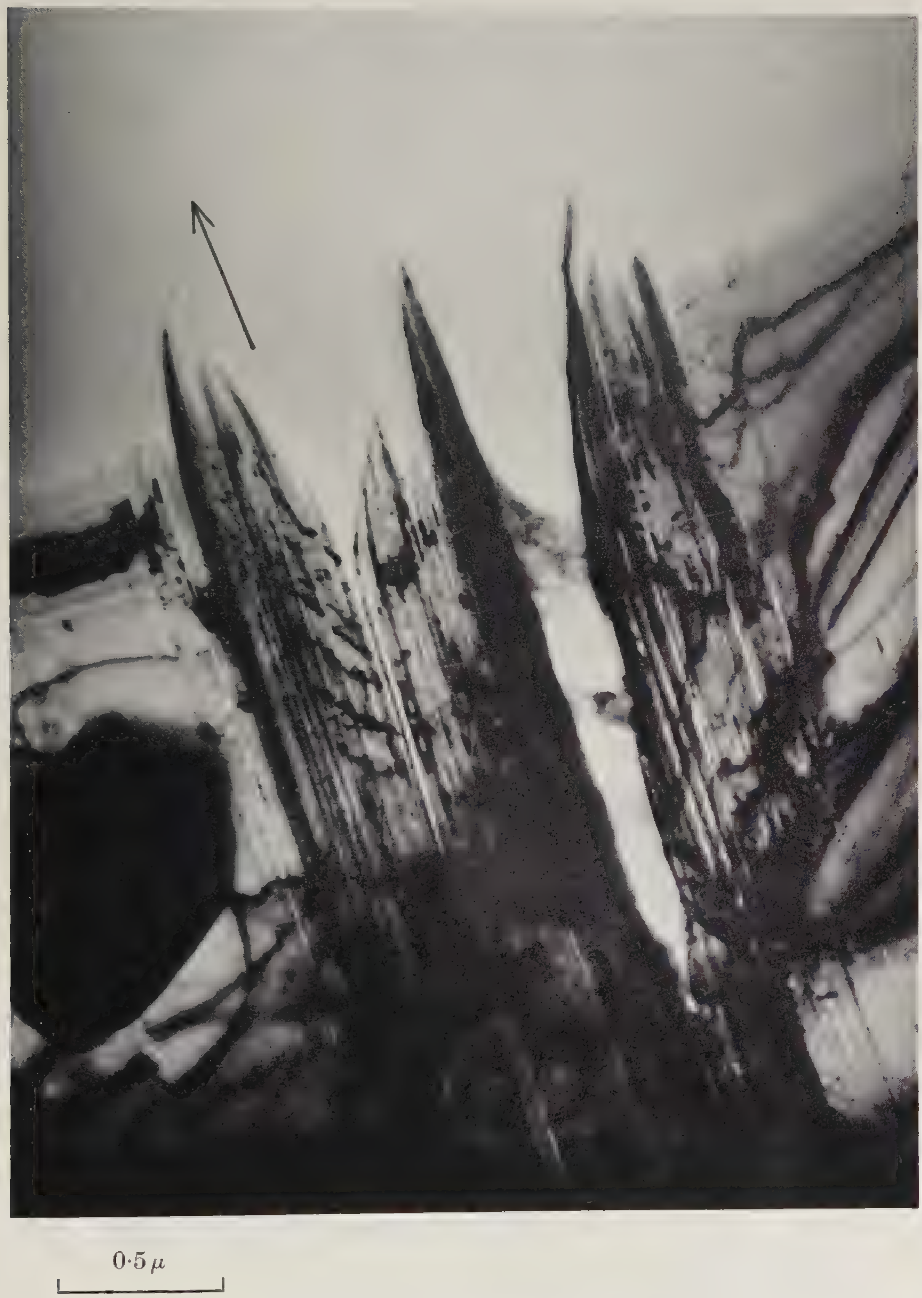

Fatigue striation showing closely spaced slip. Arrow shows direction of maximum taper magnification. Mag. ×45 000.

Fig. 5

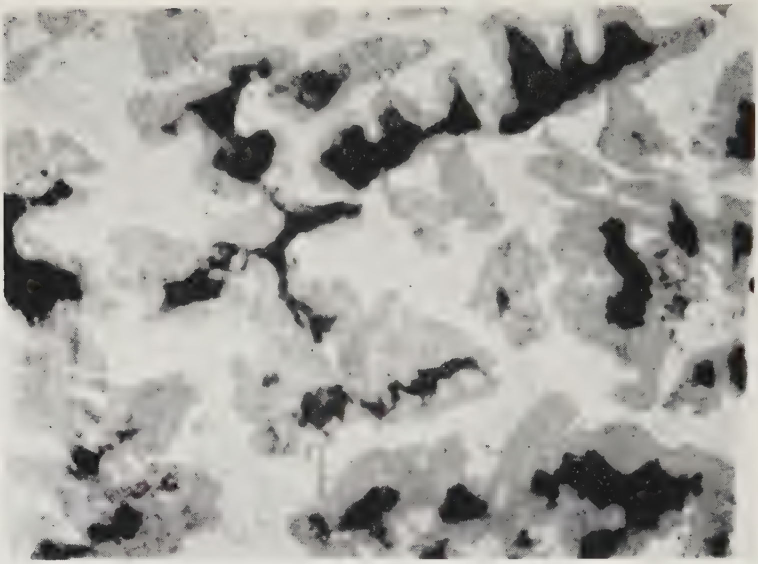

$Ag_3Al_4Mn_3$, annealed at 400°c for 7 days (×1000).

Fig. 6

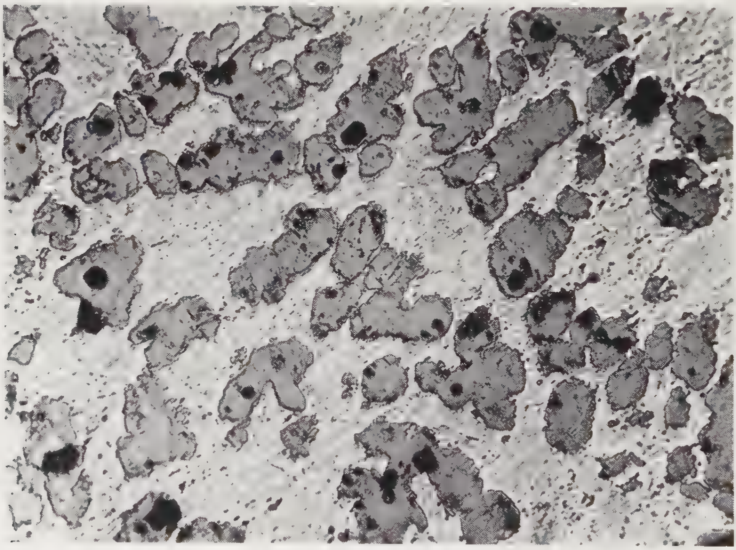

Ag_2MnAl, annealed at 400°c for 7 days (×550).

Fig. 7

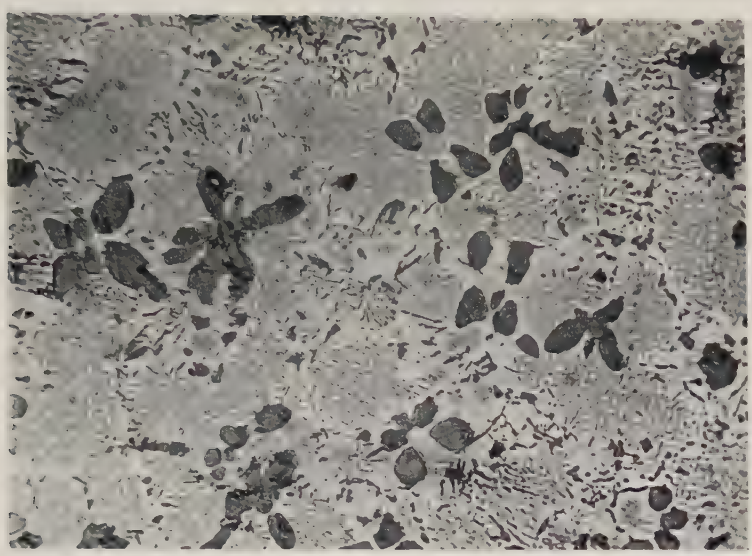

Ag_3MnAl, annealed at 400°c for 7 days (×550).

Fig. 8

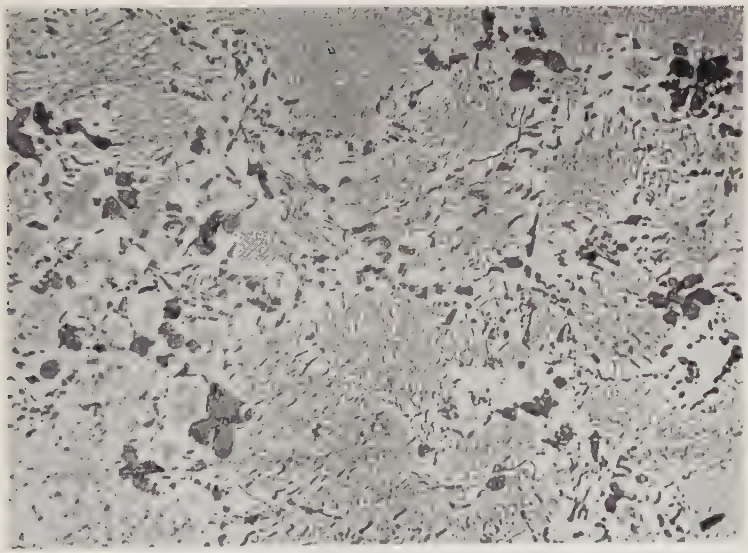

Ag_4MnAl, annealed at 400°c for 7 days (×550).

Fig. 9

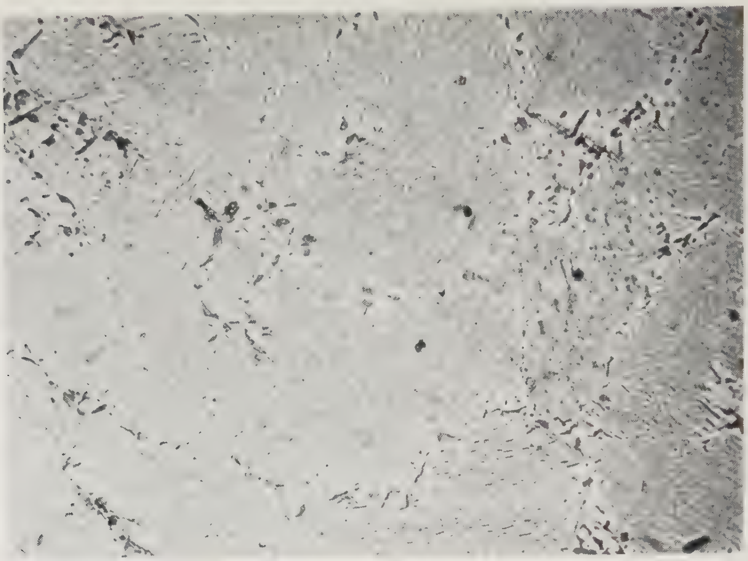

Ag_5MnAl, annealed at 400°c for 7 days (×550).

Fig. 10

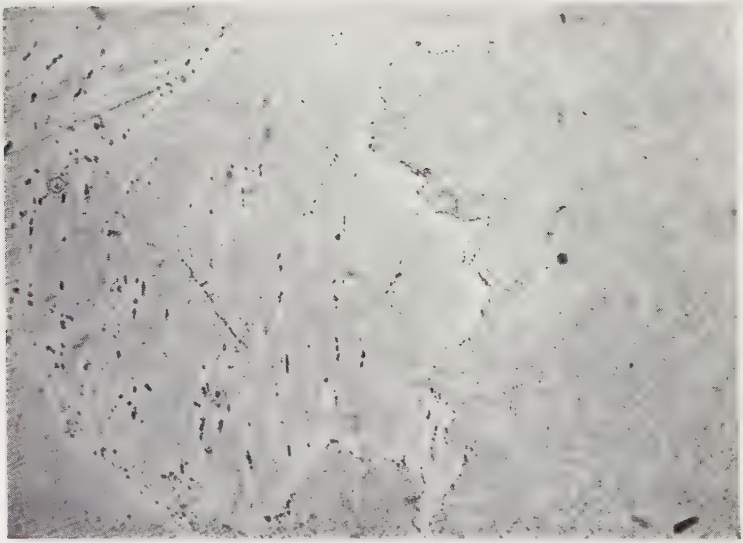

Ag_8MnAl, annealed at 400°c for 7 days (×550).

Fig. 11

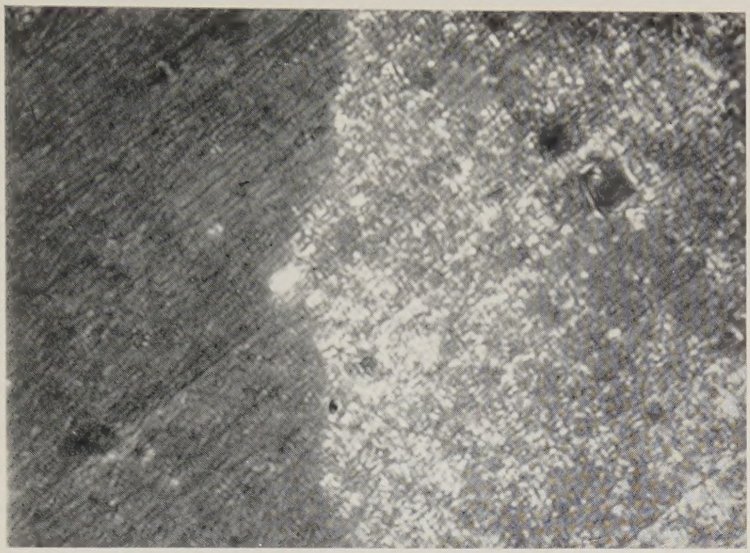

Ag_5MnAl, quenched and aged at 310°c for 7 days (×2000).
(Slightly defocused.)

Fig. 12

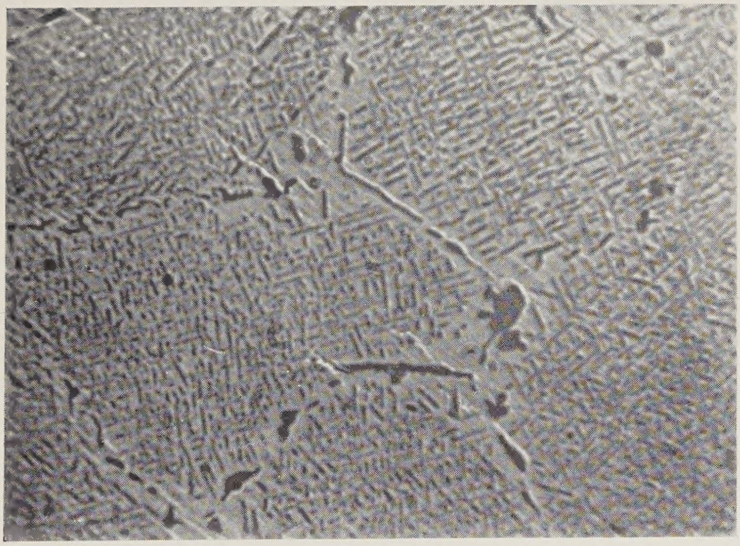

Ag_5MnAl, quenched and aged at 400°c for 7 days (×2000).

Fig. 13

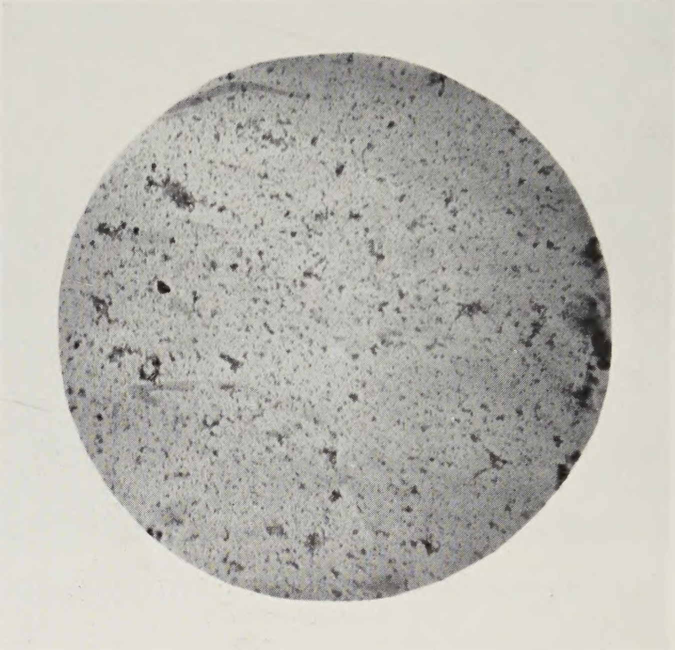

Ag_5MnAl, quenched and aged at 240°c for 7 days. Carbon replica (×10 000).

Fig. 14

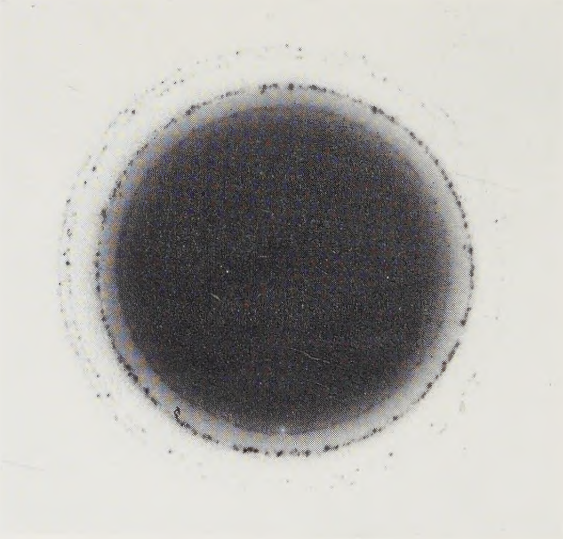

Electron diffraction pattern from same specimen.

Fig. 15

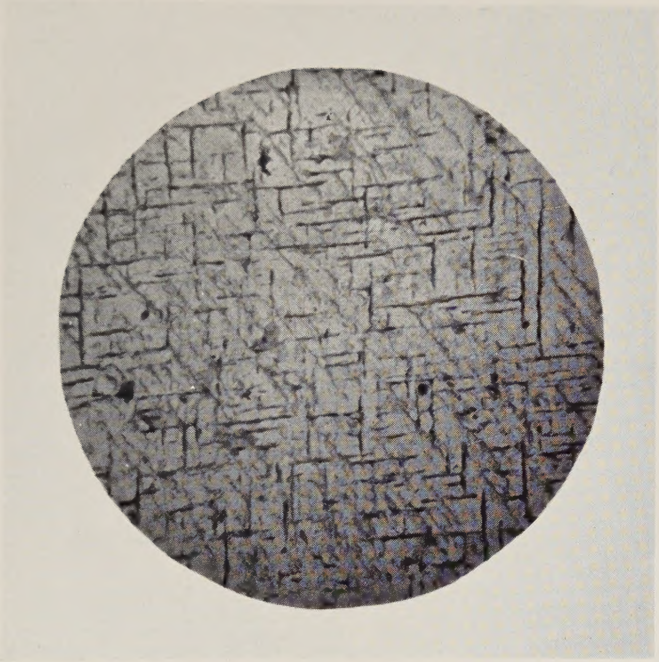

Ag_5MnAl, quenched and aged at 400°c for 7 days. Carbon replica (× 10 000).

ev
0

U. of Haw.